Master's Thesis Academic Year 2019

A Study for Improvements in Signal Readout and Background Rejection of Belle II Silicon Vertex Detector

(Belle II シリコン崩壊点位置検出器の 信号読み出しと 背景信号除去の改善の研究)

The University of Tokyo
Department of Physics, Graduate School of Science

35-186012 Yuma Uematsu

mail: uematsu@hep.phys.s.u-tokyo.ac.jp

31st January 2020

Abstract

The Belle II experiment at KEK, Tsukuba, Japan, is conducted to search for new physics beyond the Standard Model (SM) through the precise measurement of the SM parameter in the flavor physics. For this purpose, we measure e^+e^- collision events using the high luminosity accelerator SuperKEKB. To precisely measure the decay vertices, we locate the Vertex Detector (VXD) at the innermost part of the Belle II detector. VXD is a silicon tracker composed of two types of detectors; (1) a pixel detector and (2) a double-sided microstrip detector (Silicon Vertex Detector, SVD). This thesis presents studies on SVD to improve data readout and track reconstruction.

The stable operation of SVD with a large amount of beam background is challenging: studies in the first operation of VXD reveal the higher background hit-rate than our expectation, which affects both online data-taking and offline analysis at the design luminosity. Firstly, the online data rate exceeds the data bandwidth. Secondly, the offline track finding becomes difficult at such a high occupancy of background. To expand these limitations, we study modifications for each. For the former, we reduce the number of sampling points of the silicon-strip hit signals, thereby reducing the data rate. For the latter, we newly develop a hit selection method using the hit-time information, which is currently not used. This hit-time cut selectively removes the background hits because the hit-time of backgrounds is uncorrelated to that of physics signals. We review the possible effects of these two modifications and confirm their validity, analyzing the first physics data taken in the spring of 2019, with VXD fully installed. Then, we evaluate the performance of the modifications in the safety factor of the above limitations for the simulated background, using the Monte Carlo simulation with various amounts of background hits. As a result, we increase the safety factor from 1.5 to almost 5 with these modifications, which ensures the stable operation of SVD at the design luminosity.

Contents

Chapter 1
Introduction: the Belle II experiment

In this chapter, we briefly overview the Belle II experiment, then focus on one of its sub-detectors, the Silicon Vertex Detector (SVD).

The Belle II experiment is conducted at the SuperKEKB accelerator (KEK, Tsukuba, Japan) with the asymmetric collision of 4 GeV e^+ and 7 GeV e^-. The invariant mass of the collision system is 10.58 GeV, which corresponds to the mass of $\Upsilon(4S)$ [1]. Since more than 96% of $\Upsilon(4S)$ decay into $B\bar{B}$ pairs, the machine can create a large number of B mesons for precise physics measurement.

1.1 Physics motivation

The target of the Belle II experiment is to probe the existence of new physics beyond the Standard Model (SM) by measuring the parameters in SM as precisely as possible. One of the strong points of the experiment is the hermeticity of the detector. This allows us to reconstruct the decay modes with missing energy, i.e., with neutrinos in the final state. Another strong point is the asymmetric collision, which allows us to measure the lifetime difference of $B\bar{B}$ mesons in each pair, utilizing the distance between vertices. This enables the time-dependent analysis, especially the measurement of the time-dependent CP violation. Using the time-dependent decay width of $B^0/\bar{B}^0$ meson into final CP eigenstates f_{CP}

$$\Gamma\left(B^0_{\text{phys}}(t)/\bar{B}^0_{\text{phys}}(t) \to f_{CP}\right) = \left|\left\langle f_{CP} \middle| H \middle| B^0_{\text{phys}}(t)/\bar{B}^0_{\text{phys}}(t)\right\rangle\right|^2, \tag{1}$$

where $B^0_{\text{phys}}(0)/\bar{B}^0_{\text{phys}}(0) = B^0/\bar{B}^0$, we define the time-dependent CP asymmetry $a_{f_{CP}}$ [2] as

$$a_{f_{CP}} \equiv \frac{\Gamma\left(B^0_{\text{phys}}(t) \to f_{CP}\right) - \Gamma\left(\bar{B}^0_{\text{phys}}(t) \to f_{CP}\right)}{\Gamma\left(B^0_{\text{phys}}(t) \to f_{CP}\right) + \Gamma\left(\bar{B}^0_{\text{phys}}(t) \to f_{CP}\right)}. \tag{2}$$

Here we take the ratio of the decay widths, thus we can measure $a_{f_{CP}}$ without measuring the absolute size of the decay width.
Eq. (2) leads to

$$a_{f_{CP}} = \frac{(1-|\lambda|^2)\cos(\Delta M t) - 2\text{Im}\lambda \sin(\Delta M t)}{1+|\lambda|^2}, \tag{3}$$

where $\Delta M = M_2 - M_1$ for the mass difference of the mass-eigenstates B_1, B_2 of neutral B mesons and

$$\lambda = \frac{q}{p}\frac{\bar{A}_{f_{CP}}}{A_{f_{CP}}}, \tag{4}$$

where p and q for the rotation between B_1, B_2 and $B^0, \bar{B}^0$

$$|B_1\rangle = p\left|B^0\right\rangle + q\left|\bar{B}^0\right\rangle, \tag{5}$$

$$|B_2\rangle = p\left|B^0\right\rangle - q\left|\bar{B}^0\right\rangle, \tag{6}$$

and $A_{f_{CP}}/\bar{A}_{f_{CP}}$ for the decay width of $B^0/\bar{B}^0$ meson into final CP eigenstates f_{CP} without mixing,

$$A_{f_{CP}}/\bar{A}_{f_{CP}} = \left\langle f_{CP} \middle| H \middle| B^0/\bar{B}^0 \right\rangle . \tag{7}$$

Thus, by measuring the time-dependence, we can separate the contributions from $\cos(\Delta Mt)$-term and $\sin(\Delta Mt)$-term, and hence we can evaluate both $(1-|\lambda|^2)/(1+|\lambda|^2)$ and $2\mathrm{Im}\lambda/(1+|\lambda|^2)$.

One of the interesting decay modes is the radiative decay $B \to f_{CP}\gamma$ such as $B \to K^*(\to K^0_S\pi^0)\gamma$, where we can measure the photon polarization through the time-dependent CP violation [3]. The more detailed explanations for these, and the other chances to observe new physics are summarized in the Belle II Physics Book [4].

1.2 SuperKEKB

The SuperKEKB accelerator consists of three parts: linear accelerator, positron damping ring, and main storage ring. The image of SuperKEKB is shown in Fig. 1.1.

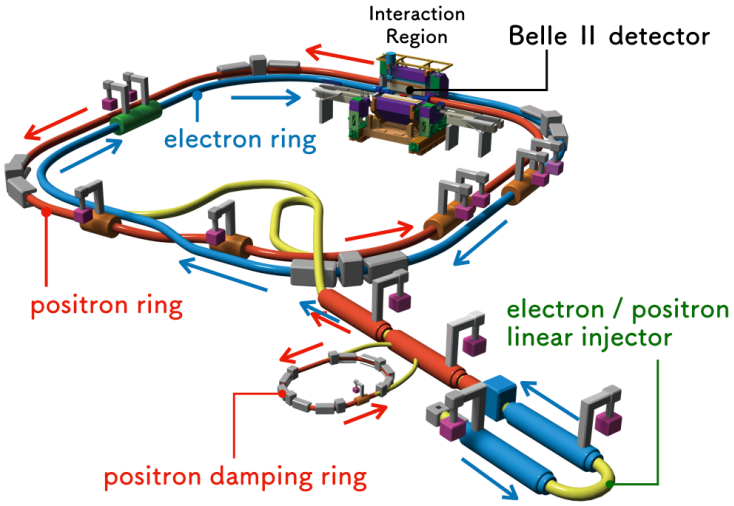

Fig. 1.1: A schematic view of SuperKEKB [5].

1.2.1 Luminosity

When the beam–beam interaction strongly limits the luminosity of a ring collider, the luminosity can be written as

$$L \propto \gamma_{\pm}\left(\frac{I_{\pm}\xi_{y\pm}}{\beta^*_{y\pm}}\right), \tag{8}$$

where β^*_y for vertical (or along the y-axis) beta function at the IP, I for beam current, ξ_y for vertical beam–beam parameter, and γ for Lorentz factor. Indices + and − stand for positron and electron beams, respectively.

The target luminosity is $8.0 \times 10^{35}\mathrm{cm}^{-2}\mathrm{s}^{-1}$, which is 40 times higher than its predecessor KEKB record, $2.1 \times 10^{34}\mathrm{cm}^{-2}\mathrm{s}^{-1}$. With this high luminosity of SuperKEKB, we aim to

integrate 50 ab^{-1}. This can be achieved with about 20 times smaller β_y^* and about 2 times larger beam current comparing to KEKB. Main machine parameters for SuperKEKB (and KEKB) are summarized in Table 1 [6]. As information for the timing distribution of physics events, the beam bunch is planned to cross every two clock-cycles of 509 MHz RF clock signal.

As a current status in Dec. 2019, $L = 1.88 \times 10^{34} cm^{-2} s^{-1}$ with $\beta_y^* = 1$ mm has been recorded and we have accumulated 10.57 fb^{-1}.

Table 1: Main machine parameters of SuperKEKB comparing with those achieved in KEKB.

Machine parameters	KEKB achieved	SuperKEKB
Energy (e^+/e^-) [GeV]	3.5/8.0	4.0/7.007
ξ_{y+}/ξ_{y-}	0.129/0.090	0.088/0.081
$\beta_{y+}^*/\beta_{y-}^*$ [mm]	5.9/5.9	0.27/0.30
I_+/I_- [A]	1.64/1.19	3.60/2.60
L [$10^{34} cm^{-2} s^{-1}$]	2.108	80
$\int L$ [ab^{-1}]	1.041	50

1.2.2 Beam background

Other than the particles from the e^+e^- collisions which we are interested to measure, particles created by secondary scatterings of off-orbit beam particles and radiated photons in detector and accelerator materials also can intrude into the detection volume to induce the background signals in the detectors. Such hits are called 'beam backgrounds' [7]. They can be classified into two types according to their origins: single-beam backgrounds and luminosity backgrounds. Single-beam backgrounds originate from beam particles scattered by another beam particle or a residual gas particle, or photons emitted by the bending of a beam particle. Those scattered particles are kicked out from the beam orbit and eventually hit the beam pipe and cause a shower, which can become a background hits. The radiative photons can also hit the beam pipe and cause a shower. The other type of backgrounds, the luminosity backgrounds, are caused by the beam collision: radiative Bhabha scattering, two-photon process, etc. Though such components are not observed yet because of the low luminosity, these will be the dominant component at the design luminosity. The measured background rate in the 2018 spring run, the decomposition method, and the estimation of future background rates are summarized by H.Tanigawa [8].

The high luminosity of SuperKEKB will lead to many beam background hits. This can result in big concerns of Belle II data-taking and analysis, especially for the inner sub-detectors such as SVD. First, they can radiatively damage the detector itself. Second, they can increase the data rate. Third, they can contaminate the physics events, affecting the detector performance in the offline analysis such as track-reconstruction.

1.3 The Belle II detector and data acquisition system

The Belle II detector consists of sub-detectors such as trackers (a vertex detector (which consists of PXD and SVD) and a central drift chamber (CDC)), particle identifiers (the TOP counters and ARICH), an electromagnetic calorimeter (ECL), a superconducting solenoid coil, and K_L/μ

identification detectors (KLM) in a magnetic return yoke. A drawing for the detector is shown in Fig. 1.2.

The coordinate system in Belle II is: z-axis is along the Belle II solenoid axis, written in the black-dashed line, and its direction is along the electron beam; x-axis is horizontal and perpendicular to the z-axis, and directed towards the right in the figure; y-axis is vertical and directed out of the paper, to the top of the Belle II detector. The cylindrical coordinate (d, φ, z)[1] and the spherical coordinate (r, θ, φ)[2] are also used.

The innermost detector is the vertex detector (VXD) located at the radial position of 1.5 cm. This enables us to measure the track vertex position with a resolution of 12 μm [9]. Another characteristic is the hermeticity. The detector covers a large physics acceptance of $17° < \theta < 170°$ from the IP.

The detailed description for each detector is summarized in the Belle II Technical Design Report [10].

[1] $x = d\cos\varphi,\ y = d\sin\varphi$

[2] $x = r\sin\theta\cos\varphi,\ y = r\sin\theta\sin\varphi,\ z = r\cos\theta$

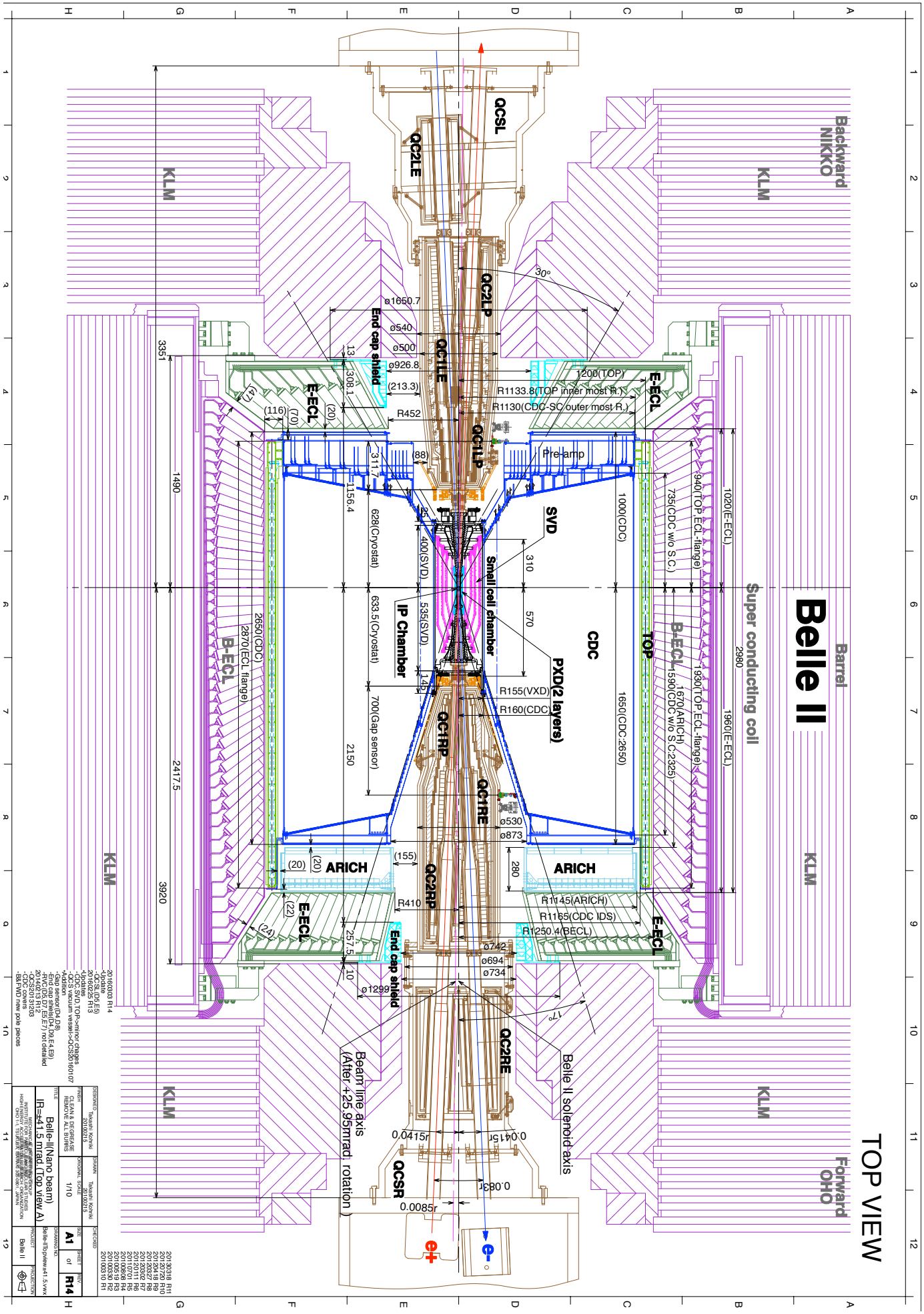

Fig. 1.2: A drawing of the Belle II detector in the longitudinal section (top view).

1.3.1 Vertex Detector (VXD)

The Vertex Detector (VXD) is located closest to the IP to measure the decay vertices precisely. The requirements for VXD are fine position resolution, small material budget, and radiation hardness. The beam pipe is also made of beryllium to suppress the material budget. VXD is the innermost detector, which consists of two types of silicon detectors: inner two layers of the Pixel Detectors (PXD) and outer four layers of the Strip Detectors (SVD) (drawn in light-blue and pink in Fig. 1.2). The 3D models of VXD and the layout of the sensors are shown in Fig. 1.3.

PXD is located as close as 1.5 cm to the IP. It has fine pixels: 50×50 μm^2 for inner layer and 50×75 μm^2 for outer layer. The sensors are fabricated based on the DEPleted Field Effective Transistor (DEPFET) technology, which allows us to make them as thin as 50 μm thick. The data size of PXD is reduced by sending hits only in the region of interest (ROI) decided by tracks reconstructed in SVD.

SVD is described in detail in Section 1.4.

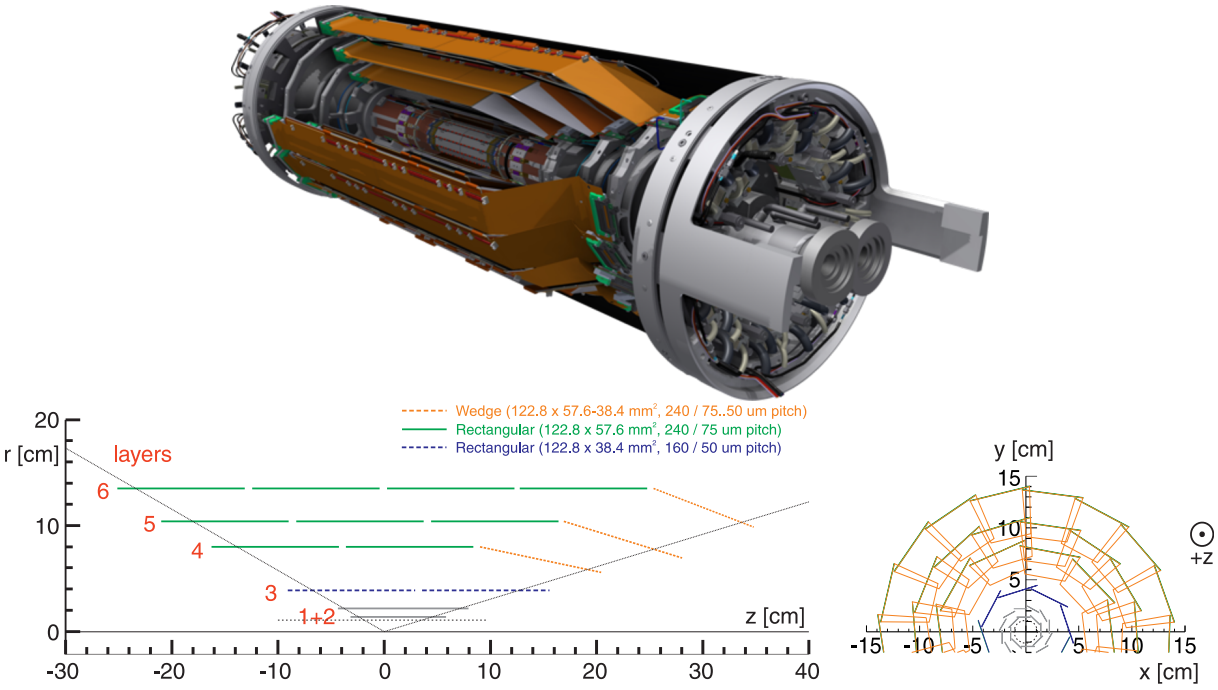

Fig. 1.3: upper: 3D model of the VXD. lower: Schematic views of the VXD in rz cross-section (left) and $r\phi$ cross-section (right). Inner two layers (grey) for PXD and out four for SVD: blue-dashed for Layer 3, green for Layer 4–6 rectangular sensors, orange-dashed for Layer 4–6 wedge sensors.

1.3.2 Central Drift Chamber (CDC)

CDC is a cylindrical drift chamber as large as 1.13 m in radius, located just outside VXD (drawn in blue in Fig. 1.2). The main purposes of CDC are tracking and trigger decisions for all charged particles. CDC has layers of stereo wires, which enables us to get the 3D hit-position information and the hit-time information with a precision of better than 1ns (see also Fig. 3.6). In the 2019 spring data which we analyze for this study, the offline EventT0, which is the time difference

between the collision timing and the level-1 trigger timing, is mainly measured by CDC offline track-reconstruction.

1.3.3 Time-Of-Propagation (TOP) counter

The TOP counter is a Cherenkov detector which consists of quartz as a medium and the micro-channel plate (MCP) PMTs as a sensor, located outside the barrel region of CDC (drawn in pear-green in Fig. 1.2). The main purpose of the TOP counter is the particle identification between $K^{\pm}$ and $\pi^{\pm}$. Another characteristic is the fine-timing resolution due to the transit time spread of MCP-PMT as small as ~30 ps. This also gives us event timing with high resolution and will be used for level-1trigger timing with high resolution in the future. However, since the offline TOP timing information was not available at the 2019 spring data, in this analysis we use the offline CDC timing information for the EventT0 estimation as explained above.

1.3.4 Calorimeter (ECL)

ECL is an electromagnetic calorimeter using a 30 cm long CsI(Tl) crystal, which corresponds to 16.1 radiation length. They are located outside the TOP counter (drawn in purple for barrel region, dark-green for end-cap regions in Fig. 1.2). The purpose is the identification and energy measurement of $e^{\pm}$ and γ. One characteristic is the hermeticity: it covers $12.4^{\circ} < \theta < 155.1^{\circ}$ except for two gaps between the barrel and end-caps ($\sim 1^{\circ}$ wide). ECL has a fast shaper ($\tau = 200$ ns) for the trigger, which is currently the main source of level-1 trigger timing. ECL is also used for measuring the event timing, though the proportion is small compared to CDC.

1.3.5 Level-1 trigger

In Belle II, the level-1 trigger decision is based on the information of the CDC track segments, ECL clusters, TOP hits, etc.

The trigger timing, which is important for this study, is decided by the CDC, TOP, or/and ECL. TOP timing is expected to be the most precise with the resolution of 2 ns (precise enough to separate the bunch-crossing every 4 ns), though its complete implementation still needs more work. ECL timing has the resolution of 5 ns for Bhabha, 7 ns for hadron (or *physics*), 15 ns for $\mu^+\mu^-$ events, which is currently the most precise trigger timing as of Dec. 2019. Though CDC timing has a resolution of around 25 ns, the trigger upgrade scheduled in the spring of 2020 is expected to make this resolution as small as a few ns. As in the future, we expect to have jitters less than 10 ns also in ECL timing for $\mu^+\mu^-$ events. The data used in this study are taken with ECL timing.

For each level-1 trigger, the information describing which sub-trigger determines the trigger timing is distributed together with the trigger signal, and we have four-times more precise information indicating 2 ns bunch pockets for TOP timing.

1.3.6 Data Acquisition System (DAQ)

Two roles of the DAQ important for this study are trigger distribution and data readout. These systems are illustrated in Fig. 1.4.

The Front-end Timing SWitches (FTSWs) are used to distribute triggers, not only to the front-end readout electronics but also to the COmmon Pipeline Platform for Electronics Readout (COPPER) boards for each sub-detector. Along with the trigger, FTSWs also distribute a clock signal (127 MHz), which is the one-fourth frequency of the RF clock signal (509 MHz) used in SuperKEKB. FTSW also handles the BUSY signal from the front-end electronics and the COPPER to prevent the buffer overflow.

The data from the front-end electronics are sent to COPPER, which has a common interface of DAQ for the subsystems. COPPER sends data to the readout PC (ROPC) for each sub-detectors, then the data go to the first Event Builder (EB1), the High-Level Trigger (HLT) and the second Event Builder (EB2). Those data are saved in the STORAGE disks. EBs, HLTs, and ROPCs stop receiving data when their buffer becomes almost full. In other words, they cause back-pressure to the COPPER in final, thus their memories are saved by the COPPER BUSY system, also described later in Section 2.1.

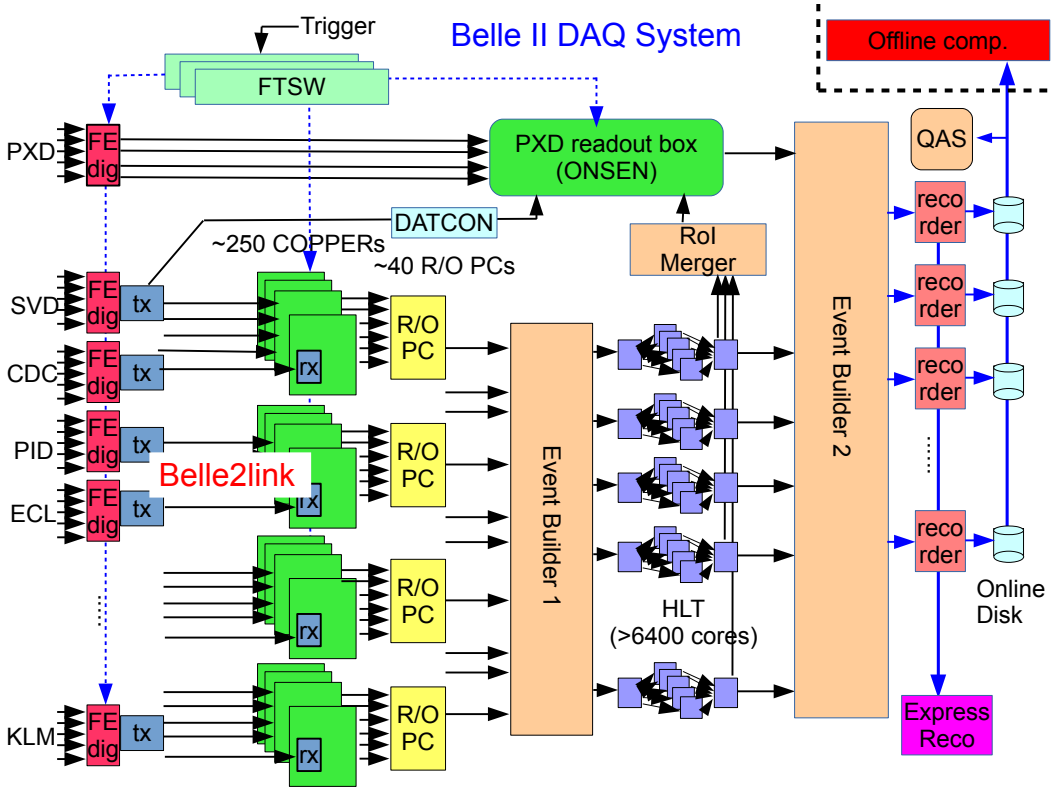

Fig. 1.4: A schematic view of the Belle II DAQ system.

1.4 Silicon Vertex Detector (SVD)

SVD covers cylindrical space of r = 4–15 cm from the IP. The important roles of SVD are the ROI decision for the PXD using the track-reconstruction with high position resolution, the reconstruction of particles with low momenta, and vertexing of K_S. The geometry is shown in Fig. 1.3.

In this section, we describe the details of the signal processing during the SVD readout and

the framework of the SVD offline analysis, which are essential for the detailed analysis of SVD signals in this study.

1.4.1 Double-Sided Silicon-Strip Detector (DSSD)

SVD is a four-layered tracking detector utilizing double-sided silicon strip detectors (DSSDs). From inner to outer, the layers are named as L3, L4, L5, and L6. Rectangular DSSD sensors are used in all layers, fabricated at Hamamatsu Photonics (HPK), Japan. A photo of one of such DSSD sensors is shown in Fig. 1.5. On the other hand, wedge DSSD sensors used in

Fig. 1.5: A photo of a DSSD sensor. This type of sensors are used in L4–6 parallel regions (drawn in green color in Fig. 1.3).

the slanted part (orange in Fig. 1.3) are fabricated at Micron Semiconductor Limited, England. Main parameters of the sensors are summarized in Table 2.

Table 2: Main parameters of DSSD sensors [10].

	Rectangular L4–6	Rectangular L3	Wedge L4–6
Number of readout strips (P/N-side)	768/512	768/768	768/512
Readout strip pitch (P/N-side) [μm]	75/240	50/160	75–50/240
Sensor size [mm $\times$ mm]	59.60×124.88	40.43×124.88	60.63–41.02×125.58
Thickness [μm]	320	320	300

A schematic view of these DSSD sensors is shown in Fig. 1.6. The mechanism of the silicon detector can be explained as follows:
We apply the inverse bias voltage to the P–N junction of the silicon semiconductor (+ for N, − for P). This creates a depletion region from P-side strips, and the higher voltage (called depletion voltage) fully depletes the silicon bulk. This means that the built-in potential expands the full width of the silicon bulk. If the particle interacts with the silicon bulk, electron–hole pairs are created. These are collected by this built-in potential and can be read out from the aluminum strip.

With an old design of DSSD, we had a problem on the N-side that the charge collected by the built-in potential diverges through the connection plane between n-bulk and SiO_2 coat (this caused by the connection like the weak P–N junction). To prevent this, we place p^+-stop to surround n-strip. Every other strip is not read out by the aluminum strip (called floating strip) on both sides of the bulk. The charge of these strips is collected by the capacitive coupling between those and their neighboring readout strips.

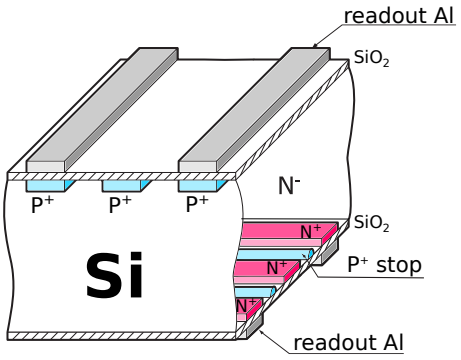

Fig. 1.6: A schematic view of a DSSD sensor.

1.4.2 Data-taking by the front-end readout ASIC

The signal detected on the strip is read out by the ASIC named APV25 [11], which was developed for the CMS silicon tracking detector. SVD system clock 31.8 MHz is generated by dividing the 127 MHz DAQ clock by four, and the APV25 is driven with this 31.8 MHz clock. On APV25, analog value is written in its ring buffer every SVD system clock-cycle (31.4 ns). We have a floating timing difference between the trigger timing in the DAQ clock regime and the trigger timing in the SVD clock regime. We record this difference ('trigger bin') for each trigger. Fig. 1.7 shows the timing chart to explain the 0–3 value of trigger bin i_{TB}.

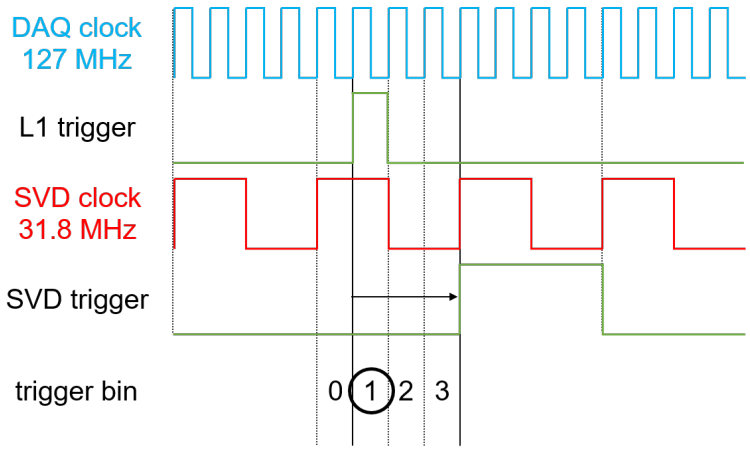

Fig. 1.7: A timing chart for the 0–3 value of trigger bin. In this case, we have $i_{\mathrm{TB}} = 1$.

The trigger (TRG) signal for APV25 needs three clock-cycles to be sent. To take the sample every clock-cycle, APV25 has to be operated in *Multi* mode where consecutive three samples per TRG signal are transmitted to the backend. We currently use 6-sample-mode in data-taking where consecutive two TRG signals per level-1 trigger signal are sent to APV25 to read out consecutive six samples for every DAQ trigger.

Analog samples to be read out are ones sampled at a fixed latency before the TRG signal arrives on APV25. The latency is set in a register on APV25 which cannot be changed during the data taking. When the TRG signal arrives, APV25 stores the ring-buffer address of the samples to be read out into FIFO. These samples cannot be overwritten on the ring-buffer anymore until the readout of the data is completed. After a certain time, the stored analog samples are readout,

taking 140 clock-cycles (about 4.4 μs) for each sample (12 for header including the address of APV25 and 128 for analog signal heights of 128 inputs).

Fig. 1.8 shows the timing chart for the SVD data-taking by the level-1 trigger, where the analog values stored in the ring-buffer are read out according to the latency.

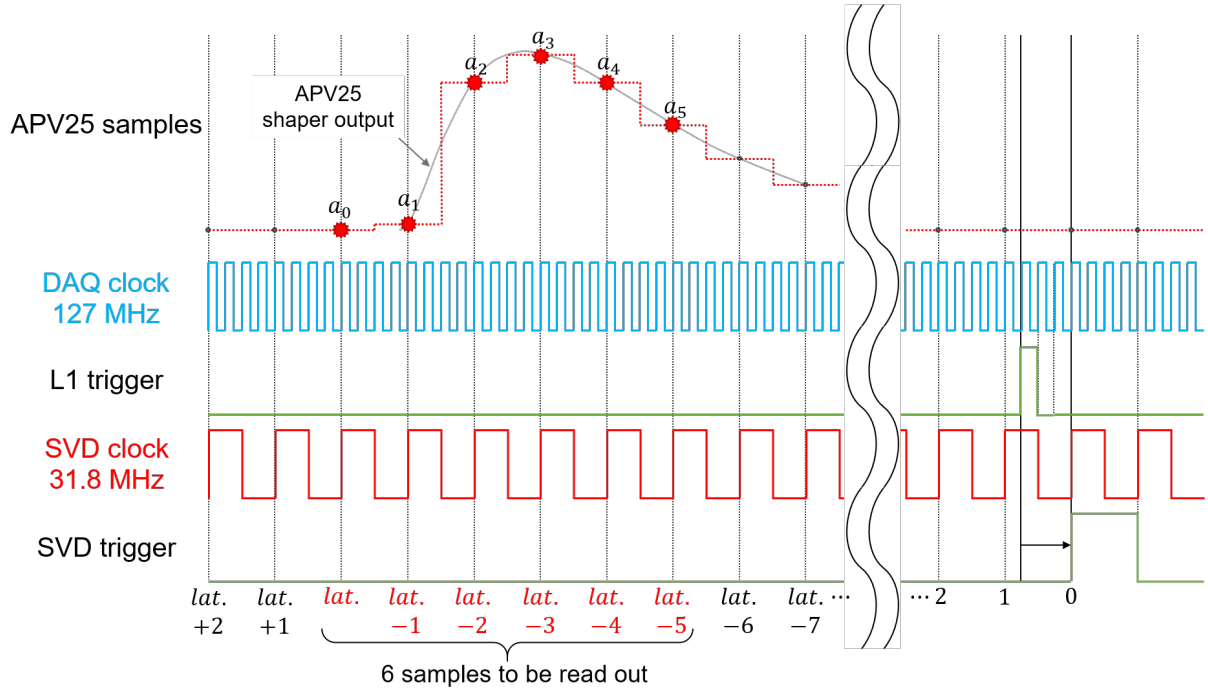

Fig. 1.8: A timing chart of the SVD data-taking by the DAQ trigger, where the analog values stored in the ring-buffer are read out according to the latency.

1.4.3 Readout chain

Each APV25 chip has 128-channel inputs, which are connected to the DSSD strips via flexible circuits (pitch adapters) using wire-bonding. Some of APV25s is placed on the sensor, using the flexible printed circuit *origami* for the readout, while the others are placed directly on the hybrid boards at the edge of the ladders. The cables from hybrid boards are connected to junction boxes where those cables are separated into the power supply lines and the cables to the flash-ADCs (FADCs).

FADCs perform data processing in the pipeline and convert the analog data to digital data. In the data processing at FADC, we apply the mask on noisy (or 'hot') strips, subtract common-mode noise, and apply a cut requiring the signal-to-noise ratio (S/N) over 3, i.e., only the strip signals with ADC samples three times larger than the noise values are recorded.

For the most downstream part of the SVD-specific readout, each FADC is linked to one COPPER boards for DAQ and Data Concentrator (DATCON) for PXD through a Finesse Transmitter Board (FTB). Flows from the hybrid boards are illustrated with pictures in Fig. 1.9.

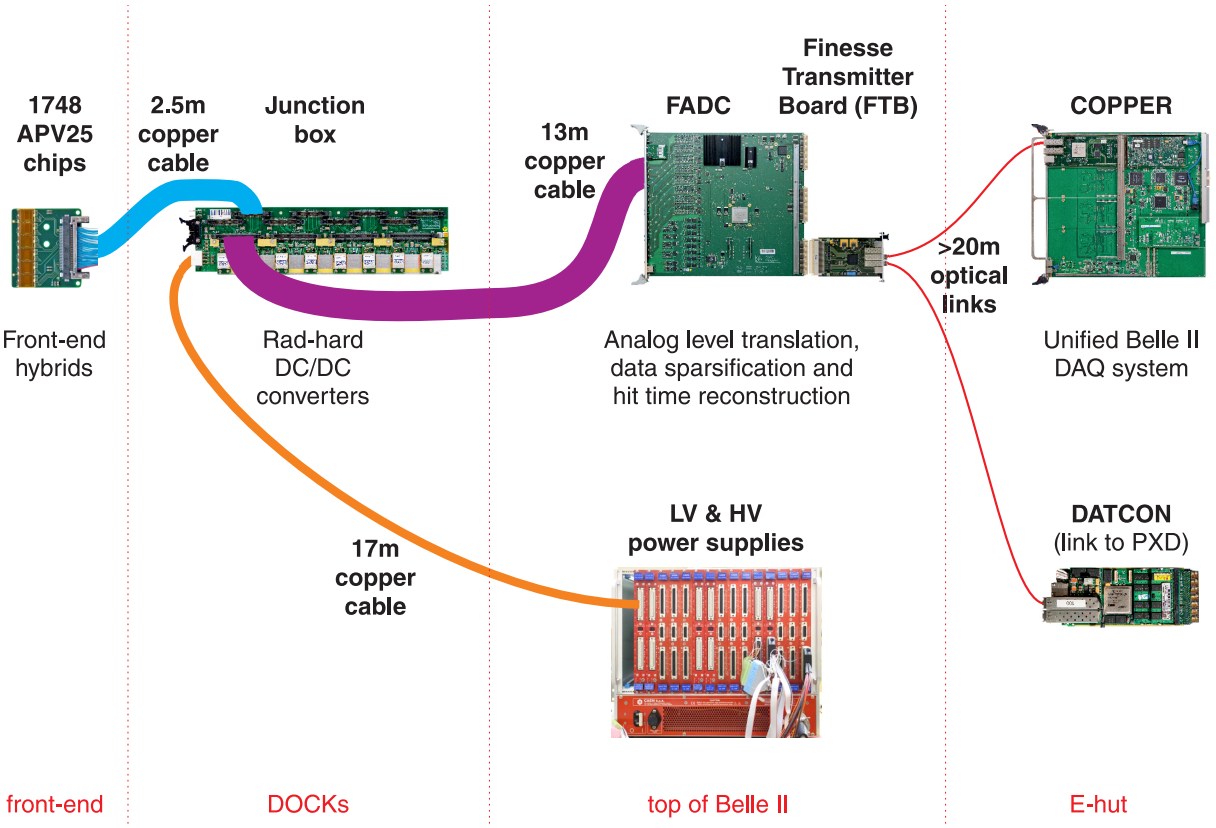

Fig. 1.9: Images of the SVD readout chain nodes.

1.4.4 Offline analysis chain: hit reconstruction in SVD

The offline analysis is done in the Belle II analysis software framework (basf2). The flow of the current six-sample hit reconstruction is summarized below:

1. hit reconstruction at each strip
   In the 6-sample-mode readout, we have six ADC samples for each strip. Here we extract the hit-time information using the 6-sample CoG method (described in Section 3.4.1) and amplitude information by taking the largest ADC sample of the six.

2. clustering
   Here we combine the strips to form the particle hit called 'clusters'. We first combine the neighboring strip hits whose S/N > 3[3]. Then we require the largest strip amplitude in the cluster to be S/N > 5. Here we extract the following information of signal: the charge of the cluster as the sum of strip amplitudes in the cluster, the cluster noise by adding the strip noise in quadrature, the cluster hit-time by taking the amplitude-weighted mean of strip hit-time, and the cluster hit position by taking the amplitude-weighted mean of strip positions (for 2-strip clusters, analog head-tail [12] for larger clusters).

3. *SpacePoint* creation
   Here we combine the U-side and V-side clusters and calculate the 3D position in the coordinate of Belle II detector from the sensor position coordinate, using the sensor geometry.

This flow of reconstruction is summarized in Fig. 1.10. After these reconstructions, we utilize the *SpacePoints* (including position, hit-time) information for the tracking.

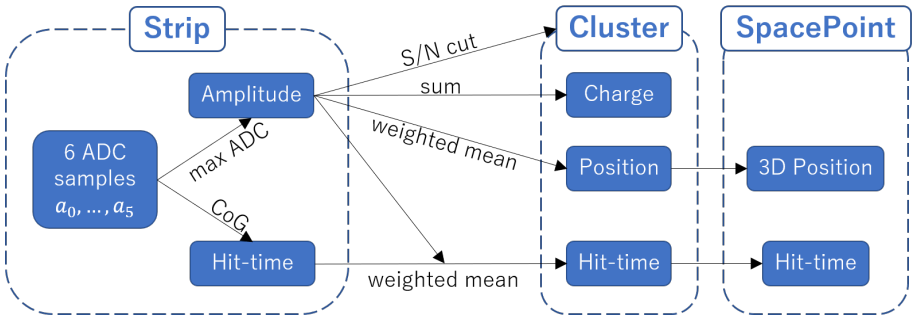

Fig. 1.10: Simplified diagram of SVD hit reconstruction. The extractions of information are drawn as black arrows.

[3]Here we can use the different (or updated) noise value from the one we use at FADCs during the online readout.

Chapter 2
Research tasks: concerns for the SVD operation

One major concern for the SVD operation is the future increase in the beam background faster than our estimation. In this chapter, we discuss the effect of the beam background on the SVD. We have two scales to represent the beam background condition: one is the scale factor to the simulated beam background at the design luminosity, called 'nominal' background, the other is the SVD hit occupancy, which is the fraction of the hit strips over SNR=5. The relation between these two scales is shown in Fig. 2.1, which is almost linear in this region.

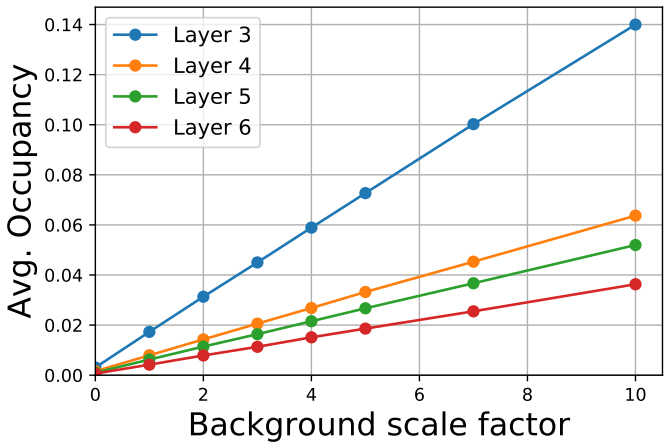

Fig. 2.1: The relation between the background scale factor and the average occupancy in simulation. The hits by electrical noise are not simulated. For the average occupancy calculation, we first calculate the occupancies on each sensor/side with SNR $\geq$ 5 cut, then take the average of them.

2.1 Data bandwidth of the SVD readout

As described in Section 1.2.2, there are various background sources in the SuperKEKB. These background events create fake triggers in addition to the expected physics event rate of roughly 10 kHz. To achieve the efficient physics-data-taking of the Belle II experiment, a trigger rate of 30kHz at the design luminosity needs to be acceptable for all the DAQ systems including SVD. The bandwidth of the SVD readout chain is first reviewed.

1. APV25 output
   In the six-sample-mode data-taking, APV25 takes 840 (= 6×140) clock-cycles to send one event of data, which is corresponding to about 26.4 μs with 32 MHz clocks. Thus, we can send at most $38{\times}10^3$ triggers per second. Because the APV25 output is before the application of the zero-suppression, this maximum trigger rate does not depend on the

SVD occupancy, and the trigger rate of 30 kHz is acceptable even under the large beam background.

2. FADC output
   The FADC output rate is 32 bit $\times$ 32 MHz. This corresponds to about 120 MB/s of the maximum data rate. We have 52 FADCs in total. This bandwidth is wider than that at the COPPER output as explained below, though the data rate is almost the same. Thus, this also cannot be a bottleneck.

3. COPPER throughput
   One COPPER for each FADC, we have 52 COPPERs in total. The limitation of the data rate through each COPPER is about 85 MB/s which is measured with the real COPPER system.

4. ROPC output
   We have 9 ROPCs in total. Each ROPC is connected to HLT with two 1-Gbps network lines, which corresponds to the data bandwidth of 250 MB/s per ROPC.[4]

5. HLT input/output
   If we do not apply the High-Level-Trigger selection on data, the limitation in the data rate will come from the HLT output (EB2 processing) speed. The limitation on the total Belle II data rate is around 300 MB/s per HLT unit (currently we have 9 HLT units and this will increase by 2 for each year, up to 20).
   With the High-Level-Trigger (HLT) selection, the data rate after the selection will decrease by a factor of six. In this case, the data rate will be limited by the HLT input (EB1 processing) speed before the High-Level-Trigger selection, around 500 MB/s per HLT unit for the total Belle II except for the PXD.

The data bandwidths, current data rates, and the design data rates are summarized in Table 3. Since the more HLT units will be introduced, the bandwidth at the HLT will not be a bottleneck. Then, the tightest limit on the data rate comes from the ROPC output. The relation between the largest data rate at the ROPC output and the background scale factor is shown in Fig. 2.2. We have the safety factor of 1.5 to the nominal background.

[4]For the long-term, an upgrade of DAQ is planned where COPPERs and ROPCs are combined into one board. If we can reduce the data rate, we can decrease the number of needed boards, hence its expense.

Table 3: The data bandwidths compared with the current and design largest data rate.

	bandwidth	current data rate[a]	design data rate[b]
APV25 output [10^3events/s]	38	3.5	30
FADC output [MB/s/FADC]	120	2.3	36
COPPER throughput [MB/s/COPPER]	85	2.3	36
ROPC output [MB/s/ROPC]	250	16	230
HLT input (total[c]/SVD only) [GB/s]	4.5 → 10	0.35/0.10	(4.9)[d]/1.4
HLT output [GB/s in the total Belle II]	2.7 → 6.0	0.70	(1.6)[e]

[a] trigger rate 3.5 kHz, the occupancy taken from the 2019 spring run data, total event size 100 MB without PXD, 200 MB with PXD, no HLT selection
[b] assuming nominal background
[c] for the total Belle II except for the PXD
[d] roughly estimated by (current rate in total) × (design rate in SVD) / (current rate in SVD)
[e] with HLT selection, roughly estimated by (input design rate) × (output current rate) / (input current rate) /6

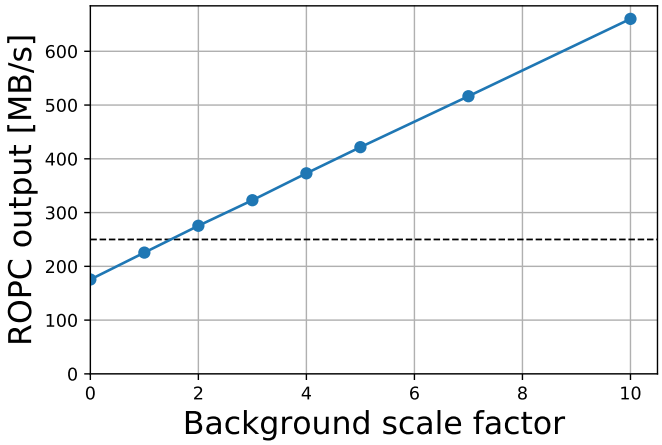

Fig. 2.2: The data rate at the ROPC output as a function of the background scale factor. The black dashed line shows the bandwidth of the ROPC output, 250 MB/s.

Even if the average data rate is within the bandwidth, the high data rate can still affect our data-taking. An instantaneous increase in the data rate causes back pressures to the buffer in the readout systems (such as APV25, FADC, COPPER, etc). To avoid the overflow and to keep DAQ running, we have two trigger veto systems for the SVD: one is APV25 trigger veto [8] and the other is a BUSY signal.

1. APV25 trigger veto
   On APV25, there is a FIFO memory for pipeline readout. To prevent this FIFO from overflowing, we implemented the APV25 FIFO emulator and to veto trigger if the emulated FIFO is almost full. This mechanism is implemented in the master of the FTSW, thus the trigger is vetoed independently from the BUSY. This trigger veto will cause 3.30±0.02% of dead time at a 30 kHz trigger.

2. BUSY signal
   If any subsystem including the SVD receives the trigger when readout data bandwidth is almost full, the subsystem issues the BUSY signal to the master of the FTSW. The FTSW stops sending the trigger when receives the BUSY signal from any sub-detectors. However, for the SVD, the buffers in the FADCs, FTBs, COPPERs, etc. are much deeper than those in APV25s. Thus, the trigger loss due to the BUSY signal from the SVD is much small compared to the APV25 trigger veto.

The reduction of the data rate will also help to suppress such trigger losses.

2.2 Track-reconstruction performance of the SVD

The track-reconstruction will also be affected by the beam background; the contamination by too many background hits will deteriorate the tracking performance. The track-finding efficiency and fake-rate of the SVD standalone track-reconstruction are shown in Fig. 2.3. We require a track-finding efficiency of 90%. Considering the track-finding efficiency in Fig. 2.3, with respect to the background effect on the tracking performance, we have a safety factor of around two for the nominal background.

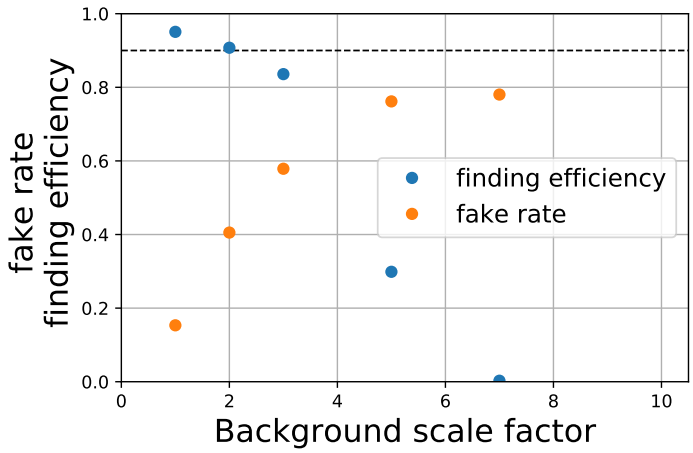

Fig. 2.3: The track-finding efficiency and fake-rate with respect to the background scale factor [13]. The black-dashed line shows the requirements on the track-finding efficiency, 90%.

The requirement on track-finding efficiency of 90% comes from the slow pion efficiency. Since CDC can efficiently reconstruct tracks, SVD standalone tracking efficiency is important only for the low-momentum track which does not reach CDC (transverse momentum less than around 36 MeV). If we assume that the decreasing rate of the SVD standalone track-finding efficiency holds for the low-momentum region, we can keep the slow pion efficiency as 9/10 of the original one by this requirement. Slow pion appears in the decay such as $B \to D^* \ell \nu$, $D^* \to D\pi$. In these cases, only one slow pion appears in the event. Thus, 9/10 of the efficiency leads to 9/10 of statistics, i.e., 1.05 times larger statistical error. We can conclude that the physics results will not be affected by such a small increase in the error.

2.3 Radiation damage

Since the VXD is the innermost detector, the SVD suffers from the radiation damage. This can lead to an increase in the reverse-bias current and the depletion voltage, and the decrease in S/N. For the SVD, we have a limitation of around 10 Mrad for total ionizing dose and around 10^{13} neq/cm^2 for the non-ionizing energy loss [14]. Conservatively assuming the 10 years of operation at the design luminosity, the total ionizing dose is estimated to be 1 Mrad and the non-ionizing energy loss is estimated to be 2×10^{12} neq/cm^2. Thus, the non-ionizing energy loss gives us a tighter limit, corresponding to the safety factor of five.

2.4 The amount of beam background at the design luminosity

We confirm that the data rate, track-finding efficiency, and radiation damage are not problematic at the nominal background. We have a safety factor of 1.5 for the nominal background as a total, which comes from the data bandwidth.

However, precise beam background simulation is difficult; there can be a large discrepancy in the simulation and the real experiment even at the current low-luminosity operation. The more realistic estimation has been made by scaling the simulated background to the observed one for each background component [15]. This gives us the Layer-3 occupancy of 7.0%, which corresponds to the almost five times larger background than the nominal one. Although this estimation still includes substantial uncertainties, the result suggests that the safety factor of two could be not enough at all for the stable operation at the design luminosity, and ideally we should have the safety factor of five or more.

In this study, we tackle the task to raise this safety factor to five for the stable operation at the design luminosity. For the radiation hardness, we already have the safety factor of five, thus we focus on the online data-rate and the offline tracking performance. To achieve the target, we test the possibility to implement the fewer-sample-mode in data-taking for the data rate reduction and develop the background hit rejection method using the hit-time information to moderate the deterioration of the track-reconstruction performance.

2.5 Overview of this thesis

In Chapter 3, we first develop the three-sample analysis method and evaluate the ideal performance of the three-sample-mode data-taking. In Chapter 4, we use hit-time information estimated in Chapter 3 to apply a selection on hits, then evaluate the background rejection performance in the track-reconstruction from the simulated sample. In Chapter 5, we evaluate the trigger jitter effect on the three-sample-mode data-taking. The final chapter is devoted to the conclusion of this study.

Chapter 3
Hit-time estimation in the reduced data-samples

As described in Section 2.1, the readout data rate of SVD can reach its data bandwidth limit at the design luminosity. To moderate the SVD data rate, we newly develop a method to read out reduced ADC samples. On the other hand, as described in Section 2.2, the tracking performance will deteriorate as the background increases. To suppress the background hit-rate, we newly develop a hit selection algorithm using the SVD hit-time.

In this chapter, we develop a new hit-time estimation method that only uses reduced ADC samples and evaluate its timing resolution in the physics data taken with the real system in the spring of 2019.

3.1 Three-sample-mode in data-taking

Since APV25 has to be operated in *Multi* mode where consecutive three samples are transmitted to the backend at each TRG signal reception (see also Section 1.4.2), we can take $n \times 3$ samples ($n \in \mathbb{N}$) per level-1 trigger signal. Currently, we are taking the data in six-sample-mode, which has a wide time-window of 6×31ns = 190 ns to accept triggers with large time jitter. Only a three-sample-mode is the possible way to reduce the current SVD data size from the six-sample-mode. A visualization of this data-taking mode is shown in Fig. 3.1. Compared to Fig. 1.8, the only difference is the number of readout APV25 samples.

3.2 Flow of Analysis

Here we briefly review the flow of analysis in this chapter. First, we see the new method to get the ADC samples with better resolution, and then we see the three-sample hit-time analysis flow in the six-sample-mode data.

As described in Section 1.4.4, in the current reconstruction flow of six ADC samples, we calculate the cluster charge and position from the strip amplitudes and the cluster hit-time from the strip hit-times. However, the strip ADC samples at the edge of the cluster are small and largely affected by the noise, which especially affects the estimation of the strip hit-time. Therefore, in this study, we develop a new flow of calculating the cluster hit-time, where we first calculate a 'clustered' ADC sample a_i defined as

$$a_i(cluster) = \sum_{strip \in cluser} a_i(strip). \tag{9}$$

Then, we estimate the hit-time from these clustered ADC samples.

We develop methods to estimate hit-time in the three samples, which are described in Section 3.4. Then, we evaluate the hit-time resolution in the real data taken in the spring of 2019, described in Section 3.5. However, those data are only taken with the six-sample-mode. Thus, we select three samples from the taken six samples ('clustered' six samples $a_0, \ldots a_5$ as defined in Eq. (9)). We describe this method in Section 3.3.

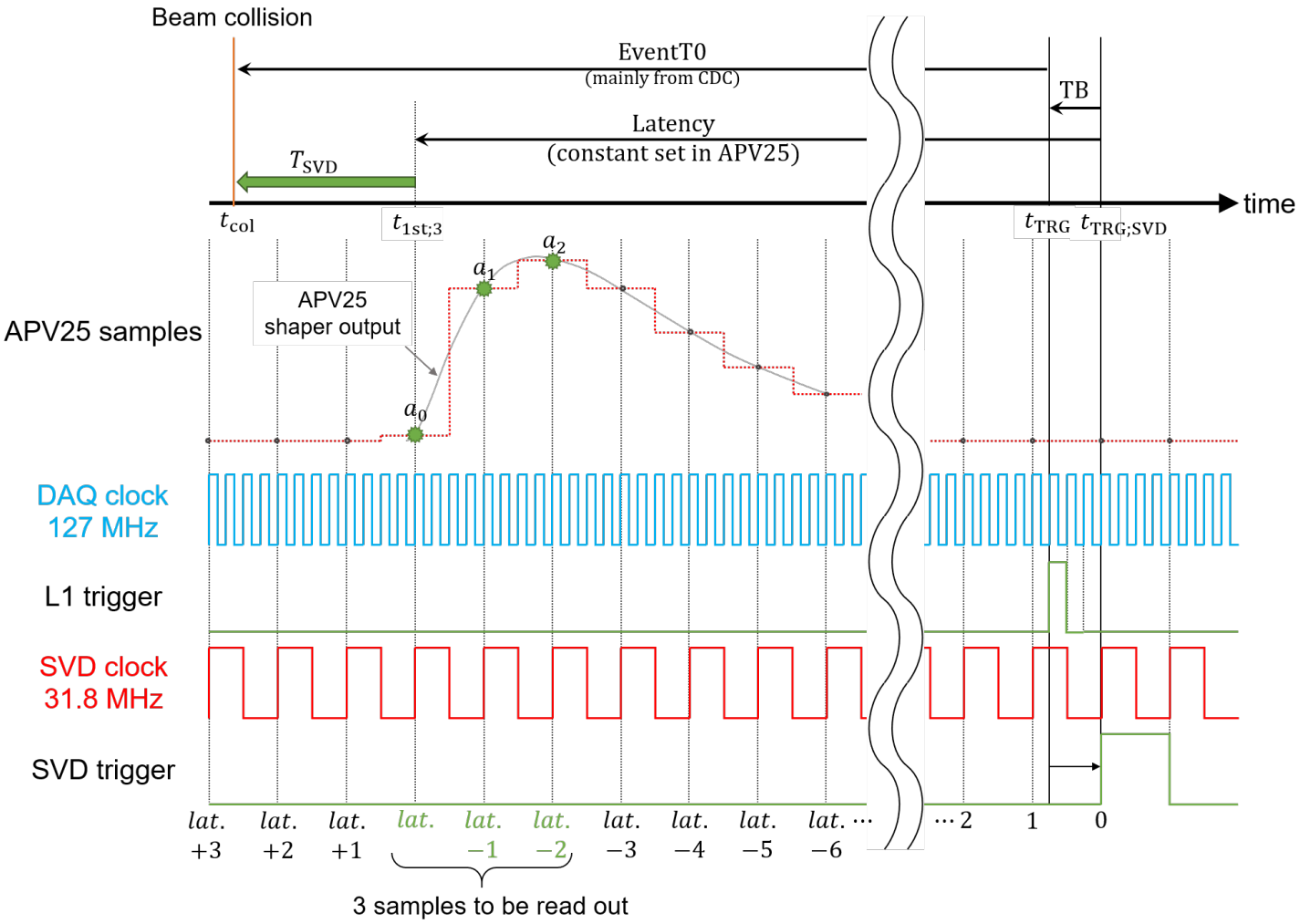

Fig. 3.1: An image of three-sample-mode in data-taking. a_0, a_1, and a_2 stand for the ADC value of each sample.

This flow of reconstruction is shown in Fig. 3.2. The flow of this chapter is as follows:

1. Develop an algorithm to choose three ADC samples from the six (Section 3.3)
2. Develop methods to estimate hit-time from three ADC samples (Section 3.4)
3. Analyze the three samples chosen from the 6 samples (Section 3.5)

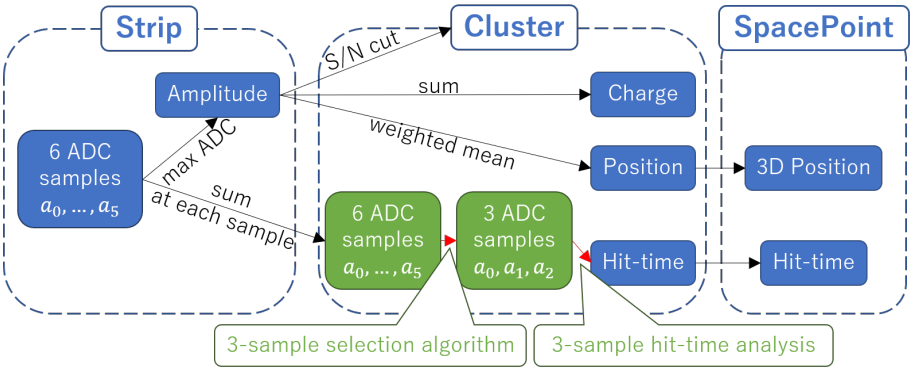

Fig. 3.2: Simplified diagram of SVD hit reconstruction in the six-sample-mode data, using the three-sample-mode hit-time estimation method for 'clustered' ADC samples.

3.3 Algorithms to choose three ADC samples from the six using the waveform information

In this section, we describe the method to get three ADC samples we analyze in this chapter from the six ADC samples in the real data.

Naively we can choose a_{i-1}, a_i, a_{i+1} from a_0, ..., a_5 with the same i for all the hits and events. However, so far the most precise timing trigger, TOP trigger, is not available yet, thus the trigger jitter is rather large. Therefore, the evaluated hit-time resolution will be heavily affected by this trigger jitter. To see the maximum performance of the three-sample timing, we select the best three samples from the six ADC samples using the waveform information, as follows.

To estimate the strip hit amplitude well by the largest ADC sample, the peak of the waveform should be included in the three samples. The simplest method to find the peak is just to use the sample a_i with the largest ADC value ('max. sample'). Then, assuming a_i is the max.

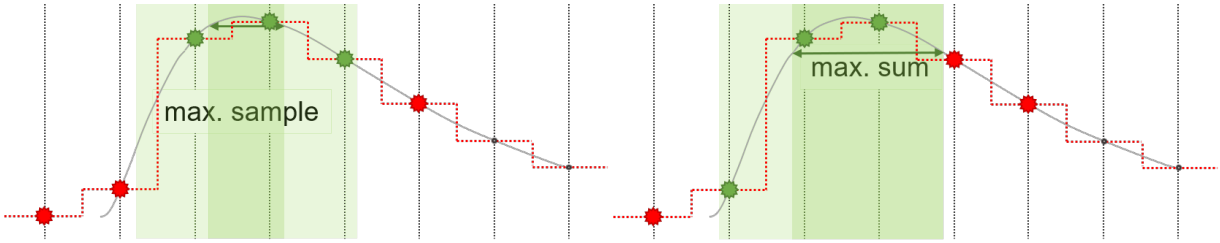

Fig. 3.3: Algorithms to choose three samples. The shaded area shows the corresponding window (ignoring the fluctuation). We use the MaxSum algorithm, shown in the right.

sample, we can satisfy the requirement by choosing $[a_{i-1}, a_i, a_{i+1}]$ as the three samples (*max. sample at the center* algorithm). Another possibility is to use the two neighboring samples with the largest sum of the ADC values ('max. sum')[5]. Assuming $a_i + a_{i+1}$ is the max. sum, if we choose $[a_{i-1}, a_i, a_{i+1}]$ (*max. sum at the latter* algorithm, hereafter 'MaxSum'), we can satisfy the requirements. These two algorithms to choose three samples are compared in Fig. 3.3.

The motivation of the MaxSum algorithm is explained as follows. Naively, we may want to use a robust algorithm, *max. sample at the center*, where we can keep the largest ADC sample in the three even if we shift the samples by one clock-cycle forward or backward. However, if we consider the signal waveform, we want to capture the rising edge for better timing resolution, as it is steeper than the falling tail. The MaxSum algorithm gives us the position of sampling slightly shifted toward the rising edge, thus we expect to have a better hit-time resolution. In Appendix A, we confirm that the MaxSum shows the optimal hit-time resolution.

When we apply those algorithms to six-sample data, in principle, such algorithms could suggest us to take three samples which are not included in the original six samples: $[a_{-1}, a_0, a_1]$ or $[a_4, a_5, a_6]$ where a_{-1} and a_6 are out of the six samples. In such case, we instead take the nearest possible three samples not to lose the efficiency by these selections: $[a_0, a_1, a_2]$ instead of $[a_{-1}, a_0, a_1]$ and $[a_3, a_4, a_5]$ instead of $[a_4, a_5, a_6]$.

The selection algorithm described in this section, the MaxSum algorithm, is not only used to analyze six samples with the three-sample analysis method but also suggests the best hit-waveform in the three-sample-mode. This information is useful when we decide the latency for the real three-sample-mode implementation (also useful for trigger emulation discussed in Chapter 5).

3.4 Methods to estimate hit-time from three ADC samples

Here we develop two methods to derive SVD hit-time T_{SVD} from three ADC samples. One is taking center-of-gravity (CoG3), the other is fitting by the least squares method with a shaper output (ELS). The estimated T_{SVD} in this section is calibrated in Section 3.5. Thus, we write as $T_{\mathrm{SVD;raw}}$.

3.4.1 Center-of-Gravity method with three samples (CoG3)

By this method, hit-time is simply estimated by taking a weighted mean of three ADC sample timings:

$$T_{\mathrm{SVD;raw}} = \frac{\sum_{i=0}^{2} a_i \cdot i\Delta t}{\sum_{i=0}^{2} a_i} \tag{10}$$

where a_i stands for the i-th sample of the three clustered ADC samples, Δt stands for the APV25 sampling period, 31 ns.

The CoG method using all six samples is currently used for reconstructing six-sample-mode data. If we assume that the shape of the hit signals does not depend on their amplitudes, this calculation gives the same hit-time for waveforms with different amplitudes. Since the result is divided by the sum of charges in this calculation, thus the error of this result is the order of noise/amplitude, suppressed by the amplitude.

[5]The position of max. sum is more stable than that of max. sample because the latter can be moved more easily by the application of a large strip noise to one sample.

3.4.2 Least Squares method with Exponentially decaying CR-RC shaper output (ELS)

Approximating the signal waveform with the impulse response of CR-RC shaper, we can derive the hit-time by fitting the three samples with the CR-RC shape function:

$$a(t) = \frac{A\left(t - T_{\mathrm{SVD;raw}}\right)}{\tau} \exp\left(1 - \frac{t - T_{\mathrm{SVD;raw}}}{\tau}\right) \tag{11}$$

where $a(t)$ for ADC sample at time t, which originated at the first sample timing of three samples $t_{1st;3}$, A for the amplitude, τ for the shaping time constant. An example of this function shape is plotted in Fig. 3.4.

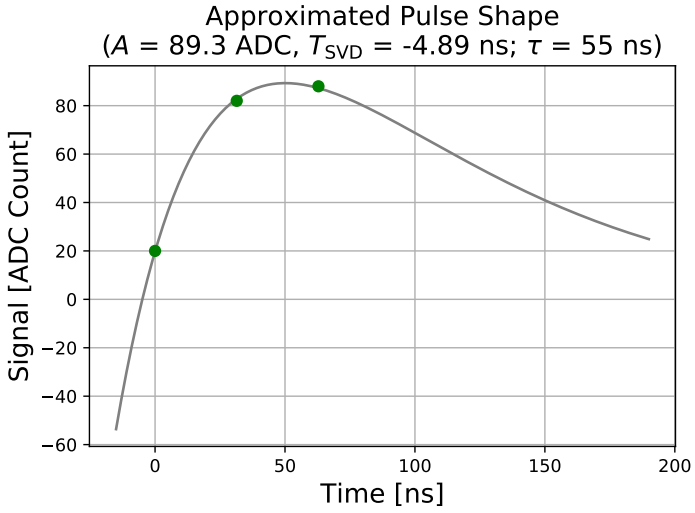

Fig. 3.4: An example of the approximation function shape and the result of the calculation. Green points show the three ADC samples used in the calculation, [20, 82, 88]. This function shape has fast-rising and long-tail because the peaking time is the same as the decaying time constant, τ.

One characteristic of this function is that the peaking time constant and the shaping time constant are identical to τ. Another important characteristic is that this function gives a value much smaller than 0 if $t - T_{\mathrm{SVD;raw}} < 0$. In data, on the other hand, recorded ADC values are around 0 (the pedestal; with no signal), and never appear to be negative due to the dynamic range. Issues induced by this feature are discussed in Section 3.5.2.

There are three parameters in this function: A, $T_{\mathrm{SVD;raw}}$, τ, where A and $T_{\mathrm{SVD;raw}}$ are free parameters while τ is a fixed parameter, 55 ns. Appendix B explains the tuning of this constant value τ. Here we fit with two parameters for three ADC samples by the least squares method. A big benefit to use the fit function Eq. (11) is that the minimization can be solvable analytically, i.e. no need to calculate the fitting on the machine. The fluctuations of the ADC samples a_i mainly due to the electrical noise are independent to the sample index i. Therefore, in the calculation of the squared sum $S(A, T_{\mathrm{SVD;raw}})$, an identical weight can be assumed for all the samples. Then, we can simply write down the $S(A, T_{\mathrm{SVD;raw}})$ as:

$$S(A, T_{\mathrm{SVD;raw}}) = \sum_{i=0}^{2} \left(a(i\Delta t) - a_i\right)^2 . \tag{12}$$

For the fitting, we require this $S(A, T_{\mathrm{SVD;raw}})$ to be stationary for the fit parameters. If we assume that A and $T_{\mathrm{SVD;raw}}$ are independent, as in CoG3 calcultaion, we can write down the conditions at the fit result as:

$$\frac{\partial S}{\partial A} = \frac{\partial S}{\partial T_{\mathrm{SVD;raw}}} = 0. \tag{13}$$

By solving this, we can get the fit results for $T_{\mathrm{SVD;raw}}$:

$$T_{\mathrm{SVD;raw}} = -\frac{2e^{-4\Delta t/\tau} + w\left(a_0, a_1, a_2; \tau\right) e^{-2\Delta t/\tau}}{1 - e^{-4\Delta t/\tau} - w\left(a_0, a_1, a_2; \tau\right)\left(2 + e^{-2\Delta t/\tau}\right)} \cdot \Delta t, \tag{14}$$

where $w\left(a_0, a_1, a_2; \tau\right)$ is a waveform-dependent factor in $T_{\mathrm{SVD;raw}}$:

$$w\left(a_0, a_1, a_2; \tau\right) = \frac{a_0 - e^{-2\Delta t/\tau} a_2}{2a_0 + e^{-\Delta t/\tau} a_1}. \tag{15}$$

For a derivation, see Appendix C.

3.5 Calibration and timing resolution study of the ideal three samples in the waveform

To compare the hit-time resolution among the two methods of hit-time estimation (CoG3 and ELS in Section 3.4), we analyze the clustered three samples which are chosen from the six using the waveform information, described in Section 3.3. The reconstruction method of such three samples is shown in Fig. 3.2. In this section, we perform *calibrations* of the hit-time estimation in CoG3 and ELS, then evaluate the hit-time resolution.

3.5.1 Formulation of calibration

The hit-time estimated by the methods described in Section 3.4 is not real-time. For example, the 10 ns difference in the true hit-time does not lead to the 10 ns difference in the estimated hit-time. This feature arises from the weighted-mean calculation itself for CoG3 and the discrepancy between the true signal waveform and the fit function shape (e.g. unrealistic negative value in the fit function) for ELS. We calibrate such 'raw' estimated SVD hit-time $T_{\mathrm{SVD;raw}}$ using well-calibrated (thus realistically scaled) event timing, called 'EventT0'. EventT0 is a time distance between the collision timing t_{col} and the trigger timing t_{TRG} mainly estimated by the CDC offline track-reconstruction. This calibration gives us the real SVD hit-time:

$$T_{\mathrm{SVD}} = g(T_{\mathrm{SVD;raw}}), \tag{16}$$

where g for the calibration function, and T_{SVD} for the real SVD hit-time in the three-sample analysis. The relation between T_{SVD} and EventT0 is shown in Fig. 3.5.

First, we consider the timing resolution of our detectors to compare T_{SVD} with EventT0. The evaluation of the resolution of SVD hit-time t_{hit} reconstruction is the purpose of this study. The resolution of EventT0 can be evaluated if the bunch fill pattern is synchronous to the trigger timing and the spacing is wide enough compared to the EventT0 resolution. We have such data on May 6th, 2018[6]. We can separate the bunch position and hence can separate the trigger jitter

[6]Exp 3, Run 786.

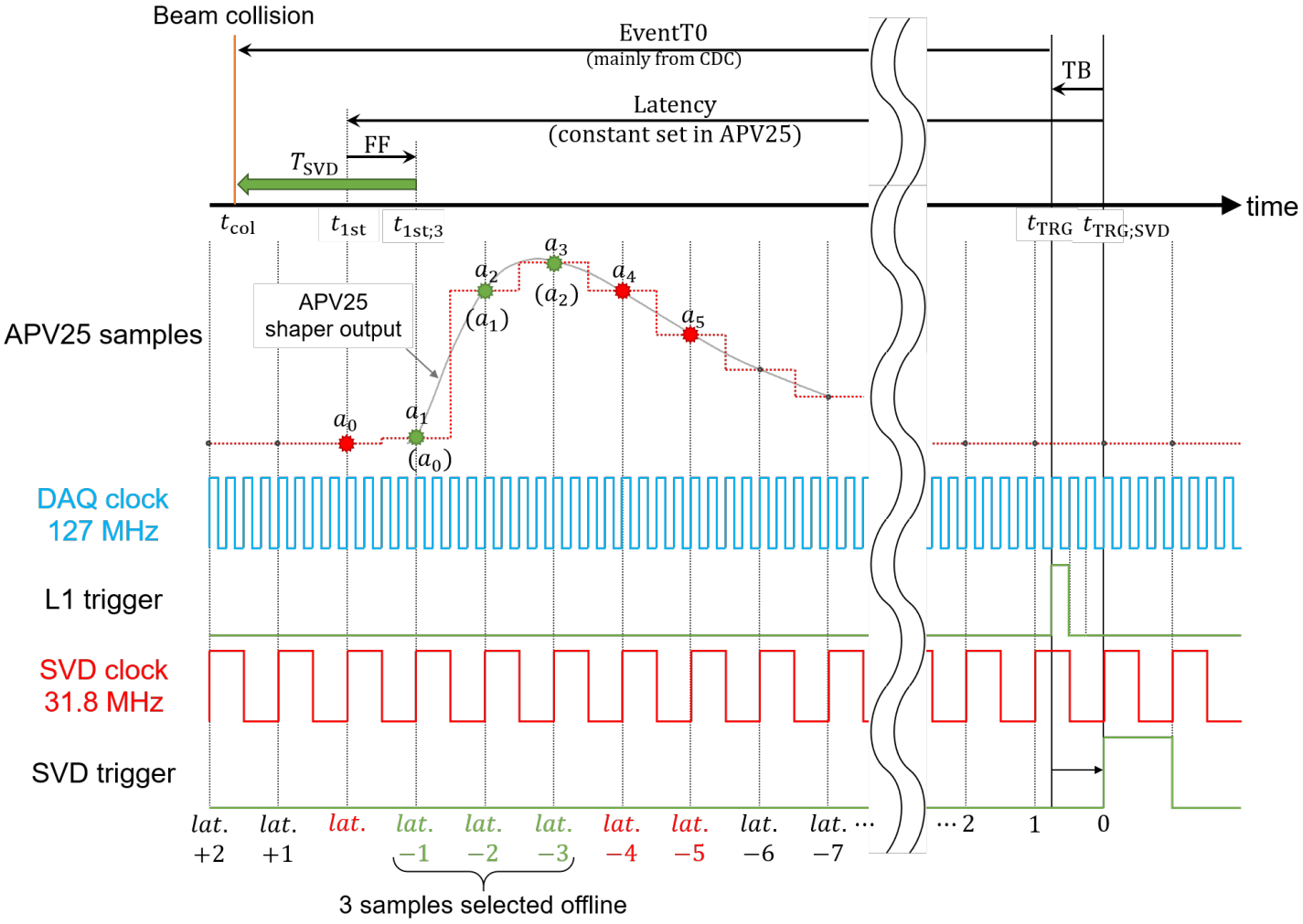

Fig. 3.5: The relations between timings. This chart explains three shifts between T_{SVD} and EventT0: one is the trigger bin correction due to the difference of the clock-phase between SVD and trigger distribution system, another is the latency to read out APV25 samples, and the other is the 1st frame correction which arises from the three-sample selection from six.

effect. The EventT0 distribution in the Bhabha events in this data-taking is shown in Fig. 3.6. By reading its σ of the fitted Gaussian for three bunch positions, we can tell that the EventT0 resolution is 0.65 ± 0.01 ns (the error comes from the fit uncertainty).

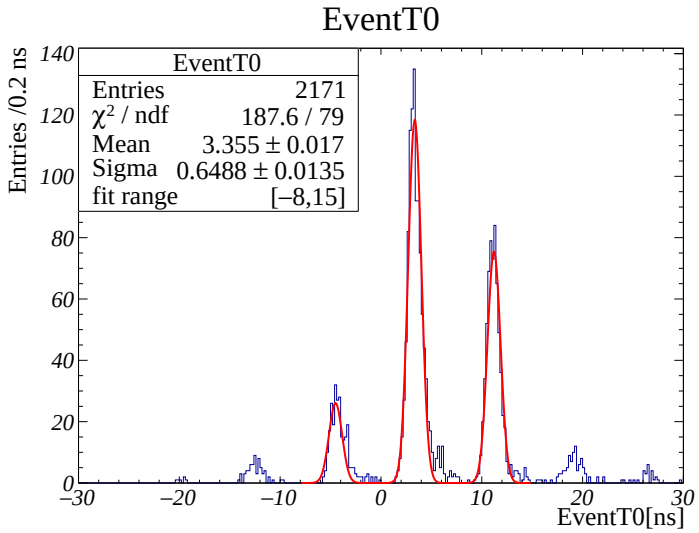

Fig. 3.6: EventT0 distribution in the special bunch-spacing condition. The width of the distribution at each bunch position leads to the resolution of EventT0. The distribution is fitted with multiple Gaussians, where the spacing is given by the bunch spacing and their sigmas are the same.

Second, we need to consider all the event-wise timing shifts[7]. Any time-information measured in the experiment is always a time difference; we measure the difference between the timing we want to know and the reference timing (usually the trigger timing). We consider the offsets in the reference timings of T_{SVD} and EventT0, listed below:

1. 1st frame (FF)
   In our calculation of hit-time, we place the timing reference at the timing of the 1st ADC sample $t_{1\mathrm{st};3}$ or $t_{1\mathrm{st}}$ (called '1st frame'), see Fig. 3.5. Thus, we need the correction for the shifts due to three-sample selection, i.e. the position of three samples in the six samples. Note that this correction is needed because we choose three samples out of six in this study; we cannot move the timing of three samples for each hit in the real three-sample-mode data-taking and there is no 1st frame correction. Using the 1st frame in the six-sample-mode $t_{1\mathrm{st}}$ and the 1st frame in the three-sample-mode $t_{1\mathrm{st};3}$, 1st frame correction is defined as
   $$i_{\mathrm{FF}} \times \Delta t = t_{1\mathrm{st};3} - t_{1\mathrm{st}}, \tag{17}$$
   where $i_{\mathrm{FF}} \in \{0, 1, 2, 3\}$ stands for the index of the first sample of the three, i.e. three samples can be written as $a_{i_{\mathrm{FF}}}$, $a_{i_{\mathrm{FF}}+1}$, and $a_{i_{\mathrm{FF}}+2}$.

2. Trigger bin (TB)
   As described in Section 1.4.2, clock-cycle of the APV25 is four times larger than that of trigger distribution system. To correct this difference, we use the trigger bin, the recorded

[7]Here we do not need to care about constant shifts in timing (e.g. a delay due to trigger distribution) because EventT0 is shifted so that the center value is at 0 for each calibration period.

four-fold phase difference of the two clocks (see also Fig. 1.7). Using the global trigger timing t_{TRG} and APV25 trigger time $t_{\mathrm{TRG;SVD}}$, trigger bin correction is defined as

$$(4 - i_{\mathrm{TB}}) \times \Delta t/4 = t_{\mathrm{TRG;SVD}} - t_{\mathrm{TRG}}, \tag{18}$$

where $i_{\mathrm{TB}} \in \{0, 1, 2, 3\}$ stands for the trigger bin.

These two differences in the time references of three-sample SVD hit-time T_{SVD} and event timing EventT0 are drawn in Fig. 3.5. An important note is that values of those time differences i_{FF} and i_{TB} are recorded and available in the offline analysis for every event. Using those time differences, we can relate T_{SVD} to EventT0 as

$$\begin{aligned}
T_{\mathrm{SVD}} &= t_{\mathrm{col}} - t_{\mathrm{1st;3}} \quad \text{(with the SVD hit-time resolution)} && (19)\\
&= t_{\mathrm{col}} - t_{\mathrm{TRG}} - (4 - i_{\mathrm{TB}}) \times \Delta t/4 - lat. \times \Delta t - i_{\mathrm{FF}} \times \Delta t && (20)\\
&= \mathrm{EventT0} + Const. - (4 - i_{\mathrm{TB}}) \times \Delta t/4 - lat. \times \Delta t - i_{\mathrm{FF}} \times \Delta t \quad \text{(with EventT0 resolution)} && (21)\\
&= \mathrm{EventT0} + i_{\mathrm{TB}} \times \Delta t/4 - i_{\mathrm{FF}} \times \Delta t && (22)
\end{aligned}$$

In the last line we remove all the constant terms for the simplicity[8]. Here, we can define the calibration function g to estimate hit-time T_{SVD} from the 'raw' hit-time $T_{\mathrm{SVD;raw}}$:

$$g(T_{\mathrm{SVD;raw}}) \coloneqq \mathrm{EventT0} + i_{\mathrm{TB}} \times \Delta t/4 - i_{\mathrm{FF}} \times \Delta t \tag{23}$$

Hereinafter, the right hand side is denoted as 'T0+TB−FF'. From this formula, we can get the calibration function g by taking the correlation .

3.5.2 Calibration

For the calibration, we use the data sample of the Bhabha events, taken in the four-hours of a physics run on 29th, May 2019[9]. In this sample, the scattered electron and positron have sufficient energies and their kinematics is simple. Additionally, as a signal selection, we only analyze clusters associated with the reconstructed tracks.

We first check the correlation between $T_{\mathrm{SVD;raw}}$ and T0+TB−FF, in Layer 3 Ladder 1 Sensor 1 N-Side as an example, shown in Fig. 3.7. As pointed in Section 3.4.2, we have distortion in correlation due to ELS fit function. This effect appears as the wider T0+TB−FF distribution.

We extract the calibration function from this correlation plot. To represent this correlation, we use simple functions with only four parameters.[10] We determine the form of calibration functions for CoG3 and ELS as follows:

$$g(x) = \begin{cases} a + bx + cx^2 + dx^3 \quad \text{(CoG3)} & (24)\\ a + bx + \dfrac{c}{x - d} \quad \text{(ELS)} \left(\text{for } x \leq d - \dfrac{\sqrt{-c}}{4}, \text{ else NaN}\right) & (25) \end{cases}$$

[8]These constants are absorbed in either EventT0 calibration or T_{SVD} calibration in Eq. (23).

[9]Exp 8, Run 1539.

[10]To get the calibration function, one may think that the spline fit is the most accurate. However, there are some problems in practice. First, the spline fit is only interpolation; it gives us no estimation outside the fit range, which can lead to some loss of efficiency. Second, it needs many parameters (four parameters for each bin). Thus, instead we use simple functions with fewer parameters.

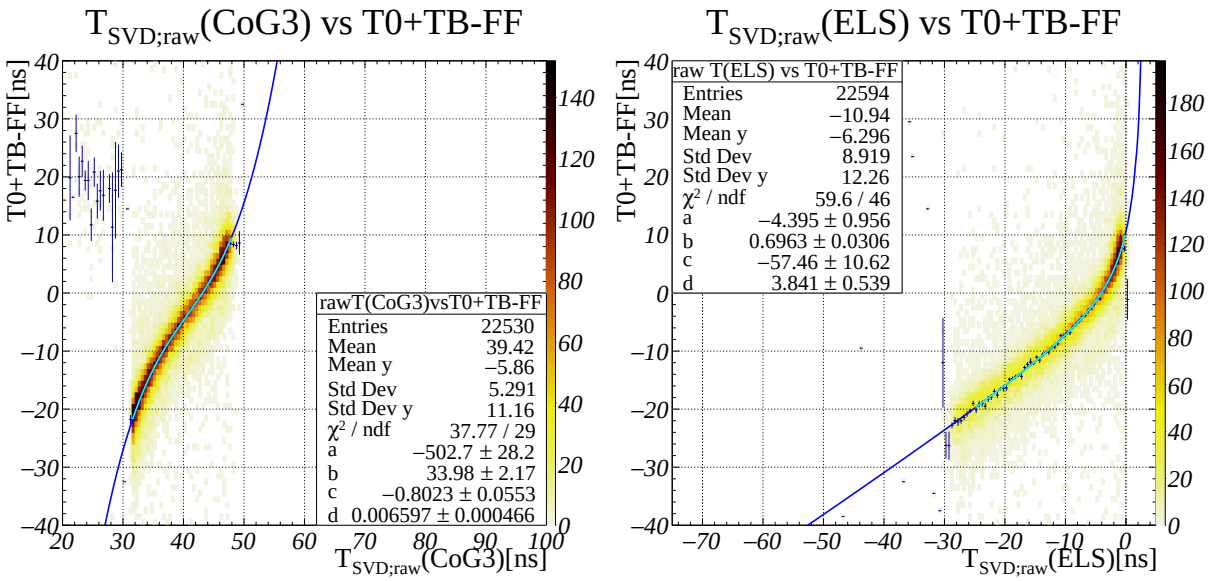

Fig. 3.7: Correlation between $T_{\mathrm{SVD;raw}}$ and T0+TB−FF in *max. sum at the latter* with CoG3 (left) and ELS (right). The dark-blue point with error bars shows the mean of the T0+TB−FF distributions at each $T_{\mathrm{SVD;raw}}$ bin, with an error calculated by its standard deviation divided by the square root of the total entries. The light-blue line and blue line represent the fit curve in the fit range and outside the fit range, respectively.

For CoG3, we use the simple third-degree polynomial.

For ELS, there are notable characteristics in the correlation between $T_{\mathrm{SVD;raw}}$ and T0+TB−FF. In the region $T_{\mathrm{SVD;raw}} < 0$, the correlation seems to be almost linear, which is represented in the term $a + bx$ in $g(x)$. In the region around $T_{\mathrm{SVD;raw}} \sim 0$, the correlation becomes distorted and the slope gets steeper, losing the correlation. This distortion can be explained by the wrong estimation of the waveform as following. We have approximated the waveform by CR-RC shaper output function $a(t)$, defined in Eq. (11). This function has one bad characteristic: $a(t) < 0$ for $t < T_{\mathrm{SVD;raw}}$, while the actual waveform in this region is almost 0 with a small noise fluctuation. Thus the hit-time estimated by the fit with $a(t)$ is strongly biased to the 1st sample timing $t = 0$ and creates the steep slope on the correlation. This characteristic is represented in the term $c/(x - d)$ in $g(x)$. In this term, we have a pole around $x = d$ which gives the steep slope. However, this could affect the calculation badly. Thus, we cut off the samples with $x > d - \sqrt{-c}/4$ and return Not a Number (note that here $c < 0$). Though this could cause efficiency loss, almost no signal is included in this region.

These fitted functions are also plotted in Fig. 3.7. Note that the determined fit functions have no fully theoretical background, while they well represent the correlations and empirically work.

To decide above calibration parameters, the most straight-forward and usual way would be fit to the points of (x, y) in a fit range by minimizing χ^2 for y. Here we discretize the x-axis by 0.5 ns binning. The χ^2 at the bin i is defined as:

$$\chi_i^2(g, y, \sigma) = \sum_j^n \frac{(y_{ij} - g(x_i))^2}{\sigma_{ij}^2}, \tag{26}$$

where index j for data entry and n for total entries at the $T_{\mathrm{SVD;raw}}$ bin i, y_{ij} for the T0+TB−FF value at the $T_{\mathrm{SVD;raw}}$ bin i and the entry j, and σ_{ij} for their errors.

Here we assume the constant noise for each entries of the bin: $\sigma_{ij} = \sigma_i \; for \; \forall j$. Then,

$$\chi_i^2(g, y, \sigma) = \frac{\sum_j^n (y_{ij} - g(x_i))^2}{\sigma_i^2} \tag{27}$$

$$= \frac{\sum_j^n \{(y_{ij} - \mu_i) + (\mu_i - g(x_i))\}^2}{\sigma_i^2} \tag{28}$$

$$= \frac{\sum_j^n \{(y_{ij} - \mu_i)^2 + 2(\mu_i - g(x_i))(d_{ij} - \mu_i) + (\mu_i - g(x_i))^2\}}{\sigma_i^2}. \tag{29}$$

The first term does not depend on $g(x)$, thus we can drop it. Additionally, if we take μ_i as the mean of data in bin i, i.e.

$$\mu_i = \frac{\sum_j^n y_{ij}}{n}, \tag{30}$$

then the second term also drops. Only the third term remains and χ^2 is given by

$$\chi_i^2(g, y, \sigma) = \frac{n(\mu_i - g(x_i))^2}{\sigma_i^2} \tag{31}$$

$$= \chi_i^2(g, \mu_i, \sigma_i/\sqrt{n}). \tag{32}$$

This means that the fitting to all entries of the two-dimensional plot approximately corresponds to the fitting to the means of the distributions at the $T_{\mathrm{SVD;raw}}$ bins, with the errors on the means $(\sigma_i/\sqrt{n})$. Here we estimate σ_i's by the standard deviations of the distributions at the $T_{\mathrm{SVD;raw}}$ bins. One example of such distributions is shown in Fig. 3.8. The tail component of the distribution is not large, and the distribution have single peak. Thus, the mean value we use for the fitting is indeed a good estimator for the center of the distribution.

By applying the calibration $T_{\mathrm{SVD}} = g(T_{\mathrm{SVD;raw}})$ to the same data sample as we used for the calibration, we can get the calibrated correlations shown in Fig. 3.9. Here we fit with linear function $a + bx$ to confirm that the calibration works fine. Except that shift a in CoG3 deviates from 0 by about 3σ, the correlation after calibration is consistent with $T_{\mathrm{SVD}} = \mathrm{T0} + \mathrm{TB} - \mathrm{FF}$.

We explain the calibration on one side of one specific sensor. The fit quality χ^2/NDF is checked in the calibration in each sensor and side, and the results are shown in Fig. 3.10. The distribution is concentrated along $\chi^2/\mathrm{NDF} = 1$, thus we confirm that the fit of the calibration function goes well in all the sensors/sides. Also all the calibration parameters are checked in Appendix D and confirmed to be reasonable.

3.5.3 Timing resolution study and the best analysis method

The determined calibration function g enables us to calculate $T_{\mathrm{SVD}} = g(T_{\mathrm{SVD;raw}})$. Calibration is done on each sensor and side to the common EventT0, and here we combine the results of all.

Also, selections for the events and the tracks listed in Table 4 are applied, so that we use only clusters from pure Bhabha e^+e^- tracks. With this selection, we can achieve almost 100% purity. This can be checked in the supplementary angle distribution with the other cuts applied, shown in Fig. 5.6. The width of the peak is around 0.2°, which is sufficiently narrow for the purification of the signal. Here, if we assume the background exponentially decaying as supplementary

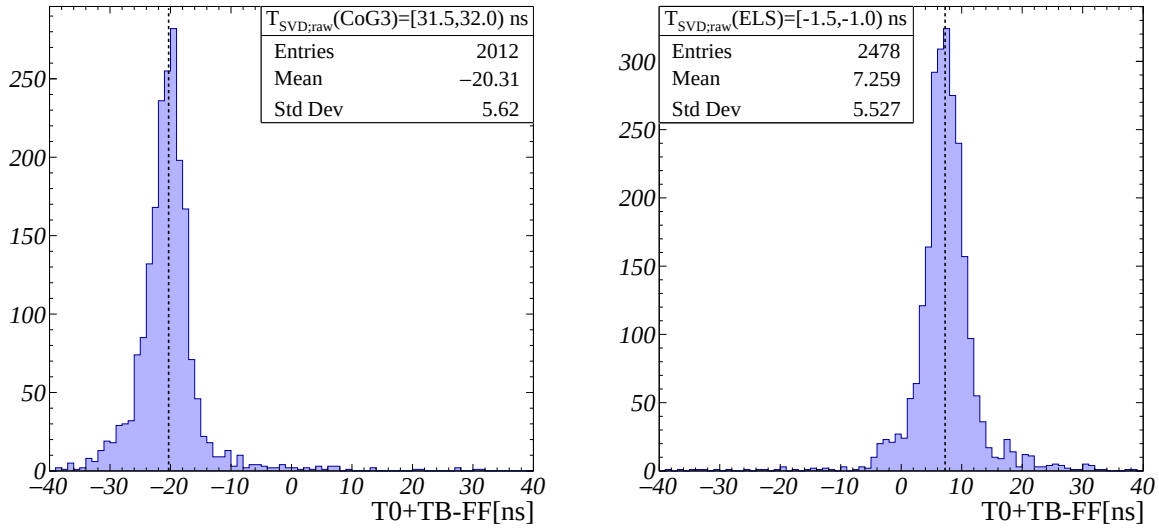

Fig. 3.8: An example of T0+TB−FF distributions for one bin of $T_{\mathrm{SVD;raw}}$. The distribution with the largest entries is chosen; the corresponding range is [31.5, 32.0) ns for CoG3 and [-1.5, -1.0) ns for ELS. The dotted line stands for the mean of each distribution.

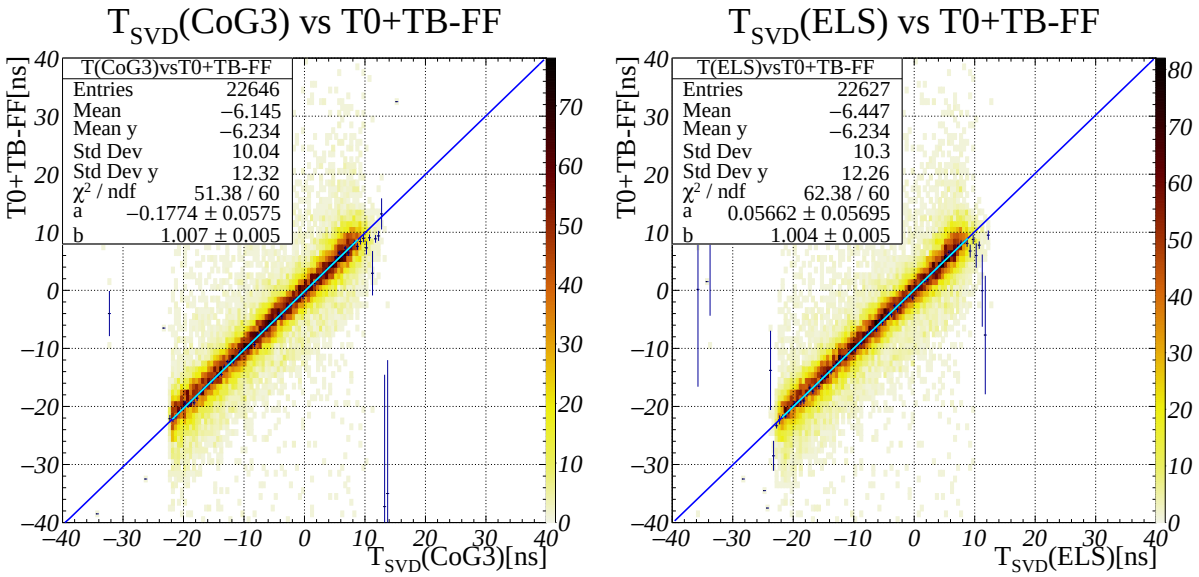

Fig. 3.9: Correlation between T_{SVD} and T0+TB−FF in *max. sum at the latter* with CoG3 (left) and ELS (right). The dark-blue point with error bars shows the mean of the T0+TB−FF distributions at each $T_{\mathrm{SVD;raw}}$ bin, with an error calculated by its standard deviation divided by the square root of the total entries. The light-blue line and blue line represent the fit line in the fit range and outside the fit range, respectively.

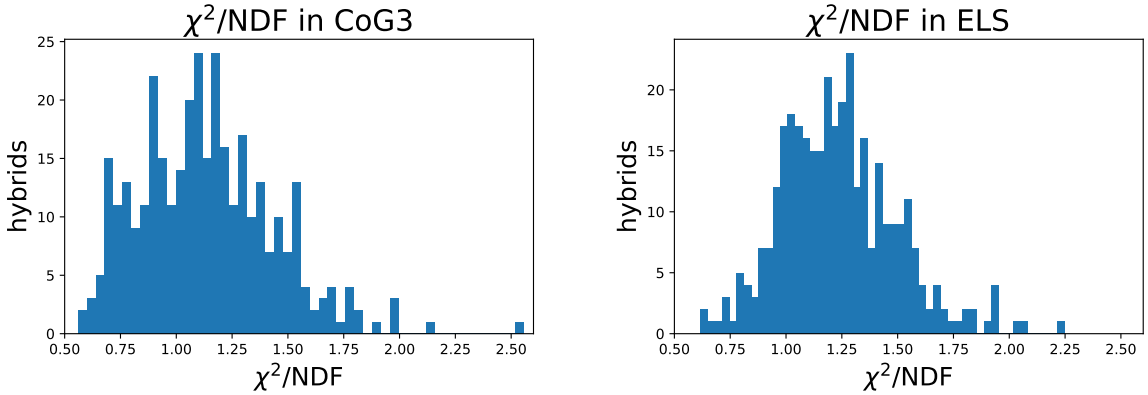

Fig. 3.10: χ^2/NDF distribution in CoG3 (left) and ELS (right) calibration.

Table 4: Cuts on track parameters applied for the signal selection. Here we make use of the simple kinematics of Bhabha scattering.

Parameters	Cut
number of tracks in the event	2
D0 (for both tracks)	(-0.07, 0.07) cm
Z0 (for both tracks)	(-0.2, 0.3) cm
the supplementary angle of 2 tracks	[0,0.1)°
momenta in the center-of-momentum frame	(5.06, 5.46) GeV

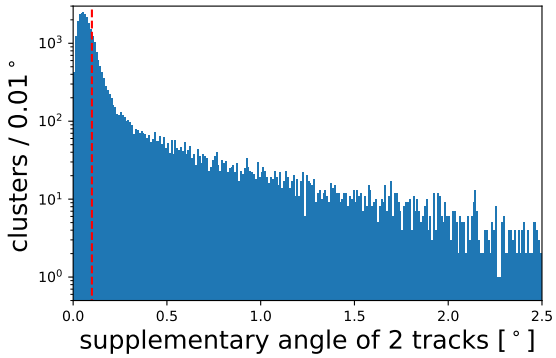

Fig. 3.11: The log-scale distribution of the supplementary angle of 2 tracks after the other cuts listed in Table 4. The red dotted line shows the cut on this variable. A sharp peak near 0 is observed, corresponds to the signal.

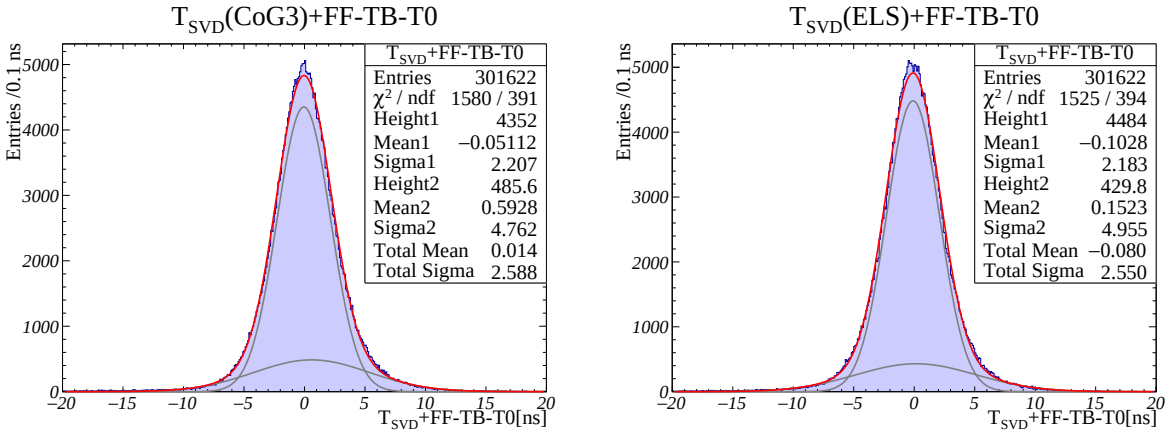

Fig. 3.12: Total distribution of $T_{\mathrm{SVD}} - \mathrm{TB} - \mathrm{T0}$ (top: *max. sample at the center*, middle: *max. sum at the latter*, bottom: *max. sample at the last*). The width of this distribution approximately consists of small t_{col} reconstruction resolution in EventT0 and the SVD hit-time resolution.

angle increases (linear in the semi-log plot of Fig. 5.6), we can roughly estimate the purity to be around 95%.

Then, we can get the distribution of $T_{\mathrm{SVD}} - (\mathrm{T0} + \mathrm{TB} - \mathrm{FF})$, shown in Fig. 3.12. As already pointed in Section 3.5.1, the width of this resolution consists of EventT0 resolution, which is around 0.65 ns, and the SVD hit-time resolution. There are small tail components and the distribution is not exactly Gaussian, thus we fit the distribution with double-Gaussian. Then, the mean and width of the distribution are given by the total mean μ_{total} and the total sigma σ_{total} of the double-Gaussian $C_1 G(\mu_1, \sigma_1) + C_2 G(\mu_2, \sigma_2)$, calculated as

$$\mu_{\mathrm{total}} = \frac{C_1\mu_1 + C_2\mu_2}{C_1 + C_2}, \tag{33}$$

$$\sigma_{\mathrm{total}} = \sqrt{\frac{C_1\sigma_1^2 + C_2\sigma_2^2}{C_1 + C_2} + \frac{C_1 C_2(\mu_1 - \mu_2)^2}{(C_1 + C_2)^2}}. \tag{34}$$

This enables us to estimate the SVD hit-time resolution σ_{SVD} as

$$\sigma_{\mathrm{SVD}} \simeq \sqrt{\sigma_{\mathrm{total}}^2 - (0.65\ \mathrm{ns})^2}. \tag{35}$$

We summarized σ_{total} and σ_{SVD} for CoG3 and ELS in Table 5. The both hit-time estimation methods have a competitive resolution, around 2.5 ns. Thus, we keep studying in the both methods. Compared to the SVD clock-cycles of 31.4 ns, we can conclude that this hit-time resolution can be a great help to distinguish the background hits. This is further discussed in Chapter 4.

Table 5: σ's of the fitted double-Gaussian and the SVD hit-time resolutions for the two hit-time estimation methods.

Method	CoG3	ELS
σ_{total} [ns]	2.59	2.55
σ_{SVD} [ns]	2.51	2.47

Chapter 4
Background rejection using hit-time

In Chapter 3, we develop two methods to estimate hit-time in three samples and evaluate the SVD hit-time resolution in the best three samples selected by the MaxSum algorithm. The result is promising, and the method we use in this study (see Fig. 3.2) can be directly used to analyze current six-sample data, i.e., we can always select the best three samples if we use six-sample data. Thus, in this chapter, we study the background hit rejection using this SVD hit-time for six-sample-mode analysis.

4.1 Hit-time distribution of beam background

The beam background comes from the electron and positron beams, thus the timing distribution of beam background is correlated to some extent with the beam-bunch crossing. This occurs at the intervals of 4–8 ns depending on the bunch fill pattern, and if this pattern is asynchronous to the DAQ clock (every 8 ns), the bunch crossing can occur in the all four 2-ns 'pockets' in the 8 ns clock-cycles and the distribution has discrete structure every 2 ns. However, the resolution of the SVD hit-time, $T_{\rm SVD}$ + FF − TB − T0, is over 2 ns as we see in Section3.5.3. Thus, such a discrete structure cannot be observed[11]. Moreover, the beam background event occurs at each bunch crossing at the same rate. Thus, the background hit-time distribution is almost flat in the time window. This can also be confirmed in Fig. 4.1.

4.2 Methods and hit-level performance of background rejection

Here we briefly describe our methods to estimate hit-time and to apply timing cut, and also the hit-level results.

4.2.1 Method to estimate hit-time

To estimate hit-time, we utilize the analysis of three samples. We select three samples with the MaxSum algorithm (see also Section 3.3) and analyze them. We use CoG3 and ELS methods to estimate 'raw' hit-time and calibrate it with EventT0. The detailed description is in Chapter 3.

4.2.2 Application of timing cut

The timing $T_{\rm SVD}$ + FF − TB − T0 distributions for signal and background are shown in Fig. 4.1. We apply the signal event selection as in Section 3.5.3, because high purity is needed to correctly evaluate the efficiency close to 100%. The detailed values of cuts are summarized in Table 4. For background, we use the events taken with the 2 Hz random trigger in the same run of data-taking. In the background event, there should be no EventT0 because there is no common event

[11] In addition to the SVD hit-time resolution, the background distribution gets smeared by the width of the hit-time distribution of background from one bunch crossing, though we do not measure.

timing among the hits. However, our analysis method, subtracting EventT0, should affect as a jitter for background hits, because there is no correlation between the background hit-time and the EventT0. Thus, to take into this effect account, we use randomly generated EventT0 instead to emulate the T0 correction on the background hit-time. Here we have a broad distribution

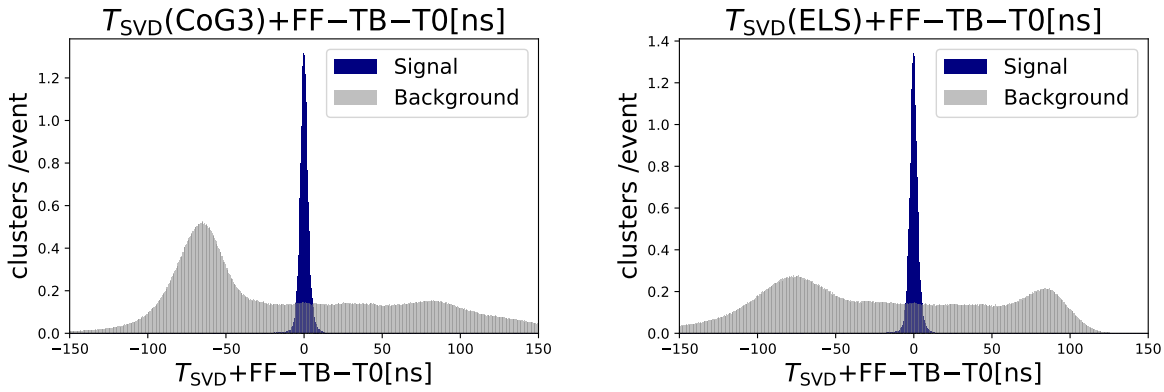

Fig. 4.1: Total distribution of T_{SVD} + FF − TB − T0 for signal (navy) and background (gray). The distributions are normalized with the number of triggers (or events) in the count.

for background corresponding to the time window of six samples. On this timing, we apply a symmetric cut with various full window width from 20 ns to 100 ns.

4.2.3 Hit-level background rejection and signal efficiency

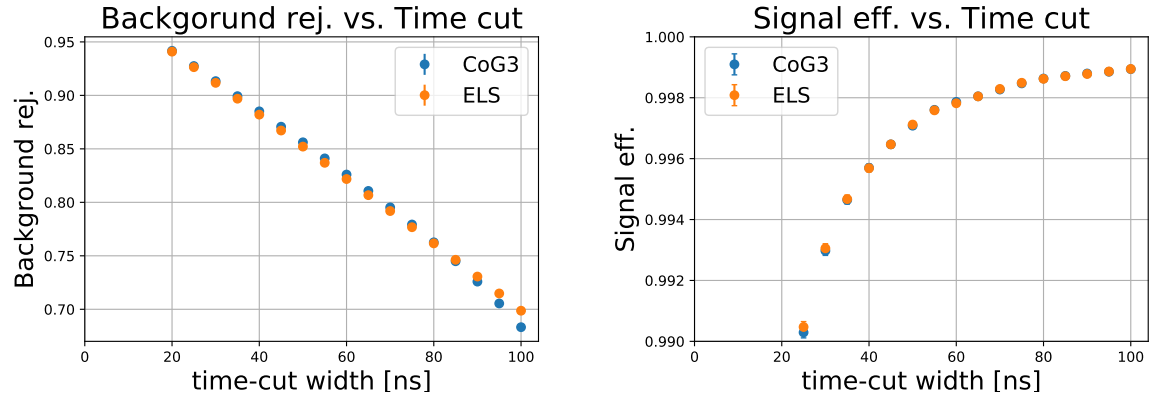

Fig. 4.2: Backgournd rejection of timing cut respect to the full width of the timing cut [ns] for CoG3 and ELS. For example, the width 30 ns corresponds to the cut (-15, 15) ns on the timing distributions in Fig. 4.1. The errors at each jitter are calculated as the Bayesian interval (CL=0.683) for the uniform prior. The plotted error bars are small and almost invisible.

The signal efficiency and background rejection of this simple time-cut are shown in Fig. 4.2. Note that we have 100% efficiency for the MaxSum algorithm, as described in Section 3.3. Though this efficiency includes the efficiency of calibration in ELS, both methods are consistent within the errors. The background rejection rate is also around the same. Here we can reject 88.51±0.02% (CoG3) or 88.20±0.02% (ELS) of background with 99.57±0.01% (both CoG3

and ELS) signal efficiency by applying [-20, 20] ns cut. We can refer these plots as the performance of the time-cut when we determine (or change) the range of the time-cut for more severe background conditions than now.

4.3 Background rejection analysis in the Monte Carlo simulation

In the previous section, we analyze the signal sample and background sample from the real data. In the current beam background condition, the track-reconstruction in SVD can be performed with good efficiency and a low fake-track rate. However, in the future background conditions where we expect rather higher hit occupancy, the tracking performance cannot be kept. Moreover, at a certain background amount, the SVD tracking itself cannot be possible. Thus, we estimate this effect from the Monte Carlo (MC) simulation.

4.3.1 MC simulation in Belle II software

The simulation procedure in Belle II can be divided into three steps [10]:

1. *event generation*
   First, we simulate physics events, i.e. creations and decays of particles. EvtGen [16] is used for this purpose. Additionally, we perform accelerator simulation SAD [17] for the event generation of the beam background.

2. *detector material simulation*
   Here we simulate the interactions between the detector material and the generated particles, for example, energy deposit in the sensor. For this simulation, a package based on the Geant4 [18] is used.

3. *detector readout simulation (digitization)*
   As for SVD, we emulate the DSSD sensor response from the simulated energy deposit (drift, charge accumulation, etc.), and the digitization on the SVD readout (including event and trigger timing). The output of the digitization has an identical format as the read data taken in the experiment.

Before we apply our analysis on the MC output, we check the correctness of the trigger jitter and the trigger timing conversion from the 127-MHz regime to the 31-MHz regime on the MC simulation, because the time propagation of the trigger signal is not fully simulated in MC.

First, we set the reference of timings to the trigger timing, as in the real data. This leads to the trigger timing $t_{\mathrm{TRG}} = 0$ at every event. For the trigger jitter, it appears in the event timing instead of the trigger timing, thus we applied the trigger jitter on event timing. The trigger jitters are randomly generated according to a Gaussian distribution with $\sigma = 10$ ns. After the trigger jitter is applied, the event timing is discretized according to the beam-bunch crossing timings. We simulate two bunch crossings per one 127 MHz clock-cycle (i.e. bunch crossing every about 4 ns). An example of the reconstructed event timing (EventT0) distributions is shown in Fig. 4.3. These bunch structures can also be observed in data as in Fig. 3.6, while the resolution of EventT0 is better in MC.

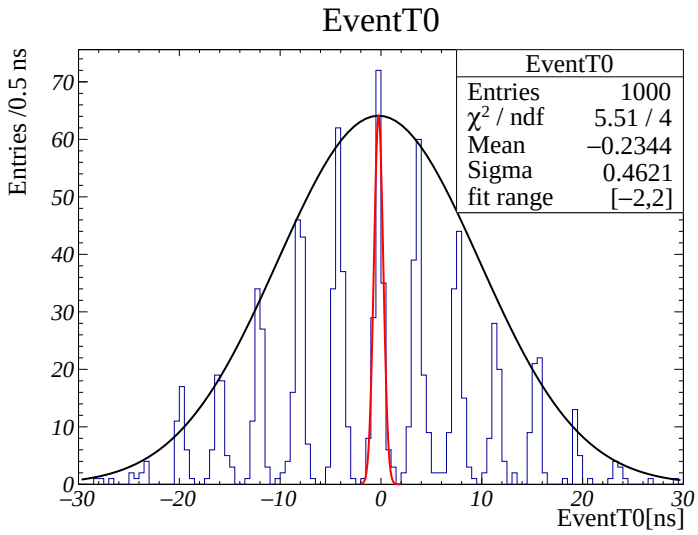

Fig. 4.3: An example of EventT0 distributions in the MC simulation, with the trigger jitter simulated. The red-line stands for the Gaussian curve fitted to the distribution of bunch crossing at the trigger timing. The black line shows the Gaussian with $\sigma = 10$ ns and with the same constant and the mean as those of the red-line.

The hit-time of the beam background is randomly generated without correlation to the trigger timing in the simulation because the beam background events, in reality, have no time-correlation with the physics events which issue the triggers. The trigger timing in the SVD 31MHz clock regime (or the trigger bin) is simulated by generating the random number i_{TB} from {0,1,2,3} and set the SVD clock phase to the timing shifted by $i_{\mathrm{TB}} \times 8$ ns from the trigger timing. By this method, timing relations are correctly handled, and consistent with what we see in the data. Thus, we can use simulated samples to estimate tracking performance.

4.3.2 Calibration in the MC sample

While the signal shape in the MC simulation is a good approximation of the real signal shape, they are not exactly same. Therefore, the calibration functions in the T_{SVD} calculation between the MC and real data can be different. For our timing analysis of the MC simulation, we use new calibration functions determined from the MC data using the same method described in Section 3.5.

Here we overview the results of the calibration done with the MC data. As in Section 3.5.2, the correlation in one side of one specific sensor (Layer 3 Ladder 1 Sensor 1 U-side) is shown for CoG3 and ELS in Fig. 4.4. Since the T0 distribution is discrete as shown in Fig. 4.3, the distribution of T0+TB−FF, which is the vertical axis of the correlation plots, is also discrete. Though this discreteness might have affected the fit, the fit looks working well to represent the correlation. With these calibrations, we derive T_{SVD} in the MC simulation.

In order to check the hit-time resolution in MC, the distributions of T_{SVD} + FF − TB − T0 is produced as shown in Fig. 4.5. As well as the real data analysis in Section 3.5.3, the distributions are fitted with double-Gaussian. The total sigmas are 2.31 ns for both the CoG3 and ELS methods, smaller than the results in data (CoG3: 2.57 ns, ELS: 2.54 ns).

Although we have a better hit-time resolution in MC, we observe two undesirable behaviors

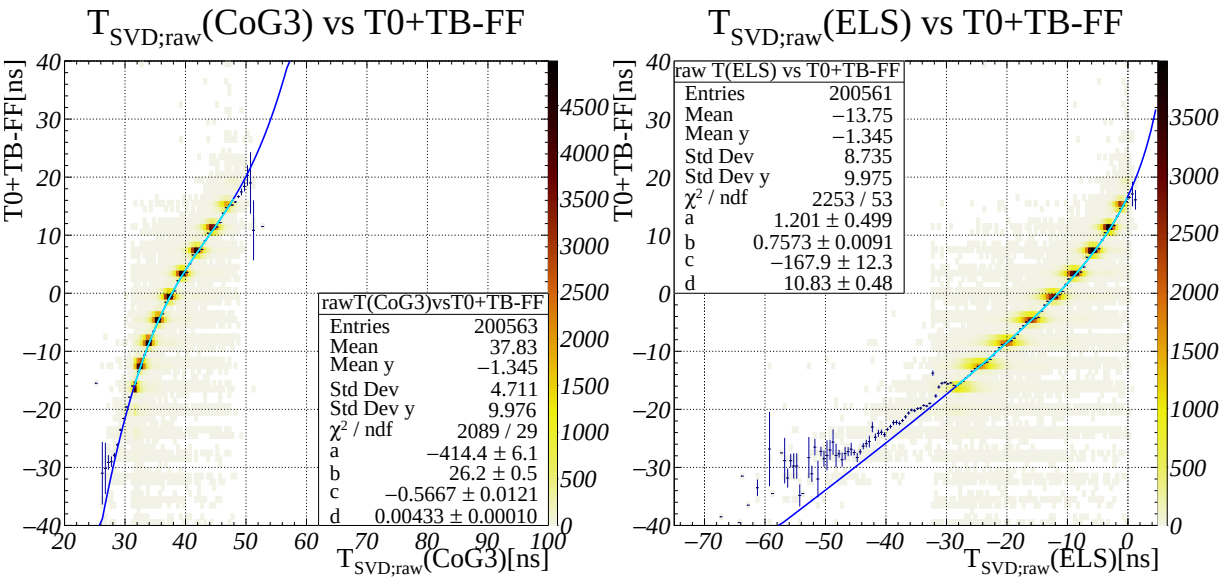

Fig. 4.4: Correlation between $T_{\mathrm{SVD;raw}}$ and T0+TB−FF in *max sum at the latter* in simulation sample with CoG3 (left) and LS (right). The dark-blue point shows the mean of the T0+TB−FF distributions at each $T_{\mathrm{SVD;raw}}$ bin, with an error calculated as its standard deviation divided by the square root of the total entries. The light-blue line and blue line represent the fit curve in the fit range and outside the fit range, respectively.

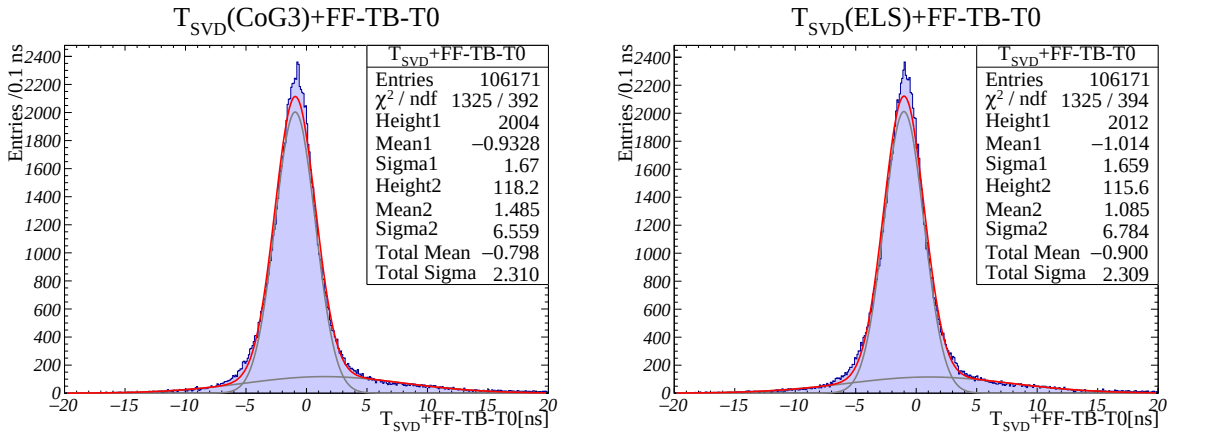

Fig. 4.5: Total distribution of T_{SVD}+FF−TB−T0 in *maximum sum at the latter*. The distributions are fitted with double Gaussian, and the width of this distribution approximately corresponds to the resolution of SVD hit-time.

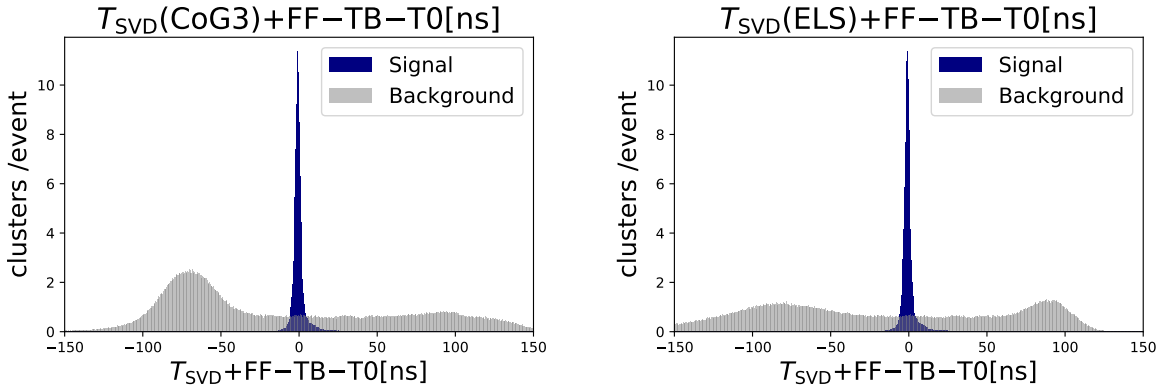

Fig. 4.6: Total distribution of $T_{SVD} + FF - TB - T0$ for signal (navy) and background (gray) from the MC simulation. The distributions are normalized with the number of triggers (or events) in the count.

in MC which are not observed in data[12]. First, the mean of the core Gaussian is around 1 ns shifted from 0, both in CoG3 and ELS, while in data the shift is less than 0.1 ns. In principle, calibration also corrects the constant shifts, thus we should have the distribution of 0-mean. This shift suggests some errors in the calibration where we cannot see in the plot. Second, we have a longer tail on the right side of the distribution. This tail decreases the signal efficiency after the time-cut as we see in Section 4.3.4.

While we do not understand the reason for these discrepancies, we do not observe such undesirable behaviors in data, and we do not have other simulation methods, thus we use this MC as it is.

4.3.3 Hit-time distributions and cut in the MC sample

The comparison of timing distributions between signal and background are shown in Fig. 4.6. While the details of the distributions are not matched completely, we have almost the same shapes of distributions as in the real data shown in Fig. 4.1. Thus, we expect the background rejection performance to be consistent with that in the real data.

Comparing the hit rate per event with the one in the real data, we have around 5 times larger background and 10 times larger signal. The background in MC is large because it is simulated at the design luminosity of SuperKEKB. The signal in MC is larger because we simulate $B\bar{B}$ events in MC while we use Bhabha events from the real data, and $B\bar{B}$ events have more final state particles than Bhabha events.

4.3.4 Hit-level background rejection and signal efficiency in the MC sample

Here we see the background rejection performance in MC and compare the results with the results in data (see Fig. 4.2). The background rejection and signal efficiency in MC are plotted in Fig. 4.7. The background rejection is almost the same as the one in the real data, but the

[12]The event type is also different, Bhabha events and hadron events, while we do not see such a big difference between the Bhabha events in data and hadron events in data.

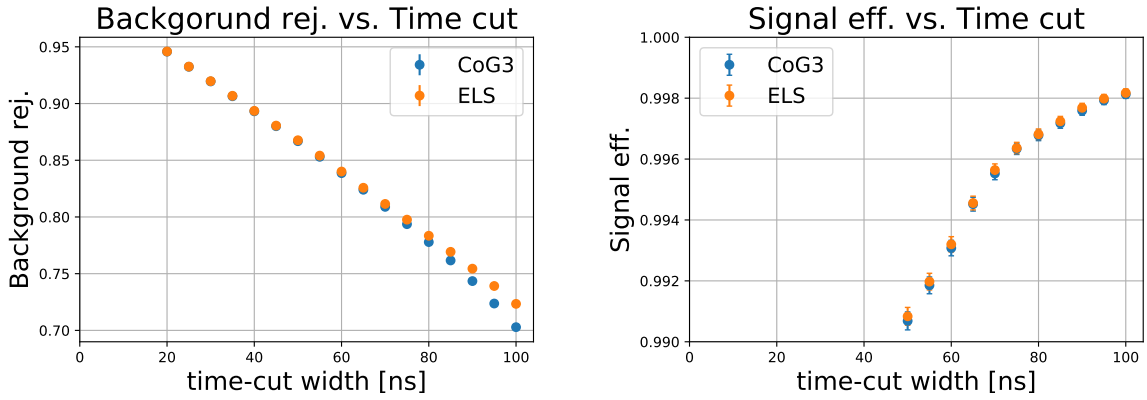

Fig. 4.7: Backgournd rejection of timing cut respect to the full width of the timing cut [ns] for CoG3 and ELS. For example, the width 30 ns corresponds to the cut (-15, 15) ns on the timing distributions in Fig. 4.1. The errors at each jitter are calculated as the Bayesian interval (CL=0.683) for the uniform prior. The signal efficiencies for time-cut width below 50 ns are less than 99.0% and not shown in the plot.

signal efficiency is much worse. This efficiency loss can be explained by the later tail of the signal timing distribution, as we see in Fig. 4.5.

We can refer to these plots to estimate the performance of background rejection. For the following track-reconstruction performance study described in Section 4.4, we use [-35, 35] ns cut to ensure 99.5% signal efficiency: 99.55±0.02% for CoG3 and 99.56±0.02% for ELS. With this cut, we can reject around 81% of backgrounds: 80.89±0.06% for CoG3 and 81.15±0.06% for ELS. Note that the result in MC is conservative; the background rejection rate in MC is smaller than that in data with the same signal efficiency.

4.4 Tracking reconstruction performance

In the current SVD cluster reconstruction without the hit time selection, the large degradation on the tracking performance is expected and the layer-3 sensor occupancy cannot become higher than 2–3% to keep the tracking performance, as discussed in Section 2.2. As well as the limitation on the data rate, this occupancy constraint currently limits the acceptable beam background rate on SVD.

Now we confirmed excellent hit-time resolutions of SVD with the newly developed method, and we also confirmed this enables us to reject the background a lot. Rejecting the beam background, the degradation of the tracking performance must be mitigated.

In this section, we study the improvement in the tracking reconstruction efficiency and fake-rate due to the time-cut. We evaluate the performance in the different SVD occupancy conditions, which are created by adding the SuperKEKB beam background at the design luminosity with various multiplication factors (×1–×10) on the simulation.

4.4.1 Methodology

Here, instead of the current hit-time which is derived with the six-sample CoG method, we are implementing the new hit-time which is derived with the three-sample algorithm, to reject

the beam background cluster hits using the new hit-time information. The reconstruction flow in this method is drawn in Fig. 3.2[13]. Additionally, we apply the hit selection after clustering using CoG3[14] timing $T_{\mathrm{SVD}}(\mathrm{CoG3})$ + FF − TB − T0. There is a remark on this hit-time cut. If the background is large, the track reconstruction in CDC possibly fails and EventT0 is not created. If we reject such events, we suffer from a large positive bias. Thus, to avoid this bias, we alternatively use 0 instead of EventT0 value; i.e., we cannot correct the trigger jitter effect with EventT0.

The tracking performance is factorized into track-finding efficiency and fake-rate. First of all, we prepare two sets of tracks: one with the tracks ideally reconstructed with true MC information (mcRecoTracks), and the other with the tracks reconstructed by pattern recognition algorithm (prRecoTracks). Then, we acquire sets of hits included in these tracks (mcRecoTrack and prRecoTrack), H_{mc} and H_{pr}. If we relate one hit to a track twice or more, we do not doubly count that hit. Using these two sets of hits, we define efficiency and purity for a pair of a mcRecoTrack and a prRecoTrack.

$$(\text{efficiency}) = \frac{\left|H_{\mathrm{pr}} \cap H_{\mathrm{mc}}\right|}{|H_{\mathrm{mc}}|}, \quad (\text{purity}) = \frac{\left|H_{\mathrm{pr}} \cap H_{\mathrm{mc}}\right|}{\left|H_{\mathrm{pr}}\right|}. \tag{36}$$

Here, $|A|$ and $A \cap B$ mean the number of the hits in the set A, and the intersection of the sets A and B, respectively. The *matching* between a mcRecoTrack and a prRecoTrack consists of two conditions:

1. the prRecoTrack is the highest efficiency track of the mcRecoTrack, and the purity is > 0.66
2. the mcRecoTrack is the highest purity track of the prRecoTrack, and the efficiency is > 0.05

There is a possibility that multiple prRecoTracks are related to one identical mcRecoTrack, i.e. satisfy the matching condition 2, but not 1. Such prRecoTracks are called to be *clones* of the mcRecoTrack.

We can calculate the track-finding efficiency, which is defined as

$$(\text{track-finding efficiency}) = \frac{\text{mcRecoTracks from primary particles matched to prRecoTracks}}{\text{all mcRecoTracks from primary particles}}. \tag{37}$$

Here, the word 'primary' means that the particles are created in the generator (i.e. physics events), not in the detector simulation. This track-finding efficiency stands for the ratio of mcRecoTracks that are found by the pattern-recognition algorithm. Note that mcRecoTracks are only part of true tracks which can be 'related' to SVDClusters and thus confirmed to be reconstructable, in principal. This 'relation' can be affected by the background condition. Comparing the BG×1 and BG×10, the denominator decreases by ∼7%. This feature possibly causes a positive bias toward efficiency.

On the other hand, the fake-rate is defined as

$$(\text{fake-rate}) = 1 - \frac{\text{prRecoTracks matched to or a clone of mcRecoTracks}}{\text{all prRecoTracks}}. \tag{38}$$

[13]Hit-time is also used in the SpacePoint creation and the track finding, while the cut is too loose or even there is no cut. Thus, the hit-time cut we apply is the dominant.

[14]The hit-level performance with [-35, 35] ns cut is almost the same for CoG3 and ELS.

This stands for the ratio of reconstructed tracks that are not related to MC true particles.

We study these two indicators for tracking performance. To estimate only the effect of the SVD beam background independently, we study the performance of the SVD-standalone tracking, where only the SVD hits are used to reconstruct tracks[15].

4.4.2 Results

First, we compare the track finding efficiency for the different background levels, see the left plot of Fig. 4.8. Even with the five times higher background than the nominal background, we achieve 89% of track finding efficiency. As for the fake rate (see the right plot of Fig. 4.8), we can suppress it to 31% at BG×5. Note that here we simply apply the symmetric timing cut, same for any background level, without any optimization. Thus, the evaluation of the performance is conservative. The cut range will be tuned for the real implementation, and the performance will get better.

We already know that hit-level background rejection is 81%, which means only about one-fifth of the beam background hits can be survived with the time-cut. However, the result in BG×1 without time-cut is inconsistent with that in BG×5 with time-cut. One possible explanation is because the background hits and signal hits are merged into one cluster. Such things are more likely to happen in heavier background conditions. Another possibility is that the background hits with similar timing to the signal affect tracking performance more badly than the off-time background hits.

To conclude, we can say that the tracking performance will be improved with the implementation of the time-cut. We achieve the safety factor of almost five to the nominal background, requiring the track-finding efficiency of 90%.

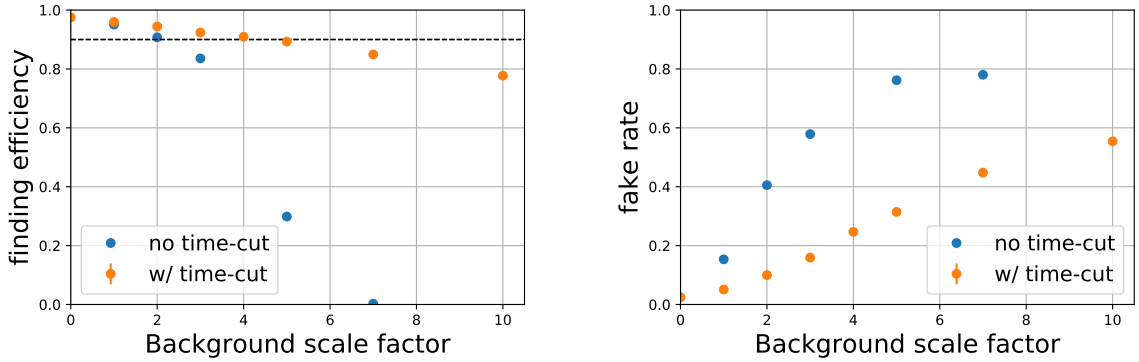

Fig. 4.8: Comparison of track finding efficiency (left) and fake rate (right) between with and without time-cut. The errors at each BG-Level are calculated as the Bayesian interval (CL=0.683) for the uniform prior. The black-dashed line in the left plot shows the requirements on the track-finding efficiency, 90%.

[15]In the usual tracking, we first find tracks in CDC and then extrapolate them to SVD. In this analysis, we need to evaluate the tracking performance as a function of the amount of the SVD beam background. However, in our current framework of the background simulation, changing the beam background affects not only SVD but also CDC. If we use the CDC tracks in this study, the CDC beam background largely affects the tracking performance.

Chapter 5
Three-sample-mode data-taking under trigger jitter

In this chapter, we evaluate the effect of trigger jitter on the SVD performance in three-sample-mode data-taking.

In Chapter 3, we can select the best three samples out of six samples with the maximum information of the hit-signal waveform. However, regardless of the sampling number, three or six, the starting time of the data samples is determined by the adjustable latency before the trigger timing, shown in Fig. 3.1. Therefore, we want to adjust this latency for three-sample-mode data-taking to obtain the best three samples with the maximum information of the hit-signal waveform. If the trigger timing is precise enough (with a low jitter), both the true SVD hit-time and the trigger timing t_{TRG} are determined by the true event timing t_{col}. In other words, we can adjust the latency well with the precise timing trigger so that we can take three samples with the best SVD performance.

5.1 The SVD performance in three-sample-mode

As the number of the samples is less, it is obvious that the three-sample-mode data have less information compared to the six-sample-mode data. Thus, one possible concern with the three-sample mode is the degradation of the SVD performance due to such loss of information. Therefore, before implementing this new mode of data-taking, we need to confirm that the performance is not sacrificed for this data size reduction.

As the intrinsic performance of SVD, i.e., before the track-reconstruction, SpacePoints are the final results and thus most important. Here the SpacePoint information is equivalent to the cluster information because SpacePoint is no more than a change of coordinates. Thus, we study the performance in the following parameters of clusters: charge, position, and hit-time. Also, we briefly check the strip amplitudes because it is the basic information and used in the calculation of the above three parameters.

Additionally, for the three-sample-mode performance, the *efficiency* of signal detection compared to the six-sample-mode is also important. We need to confirm that the three-sample-mode time-window of $3\Delta t$ = 94 ns is wide enough to cover almost all the signal, even with jitter.

Besides the current reconstruction flow, the particle identification with the energy loss information at SVD using the cluster charge and the background hit rejection using the hit-time information of SVD are under development (the latter is described in Chapter 4). Here we also estimate the background rejection performance utilizing the newly-derived hit-time information.

Therefore, in this study, we develop a new flow of calculating the cluster hit-time, which is shown in Fig. 5.1.

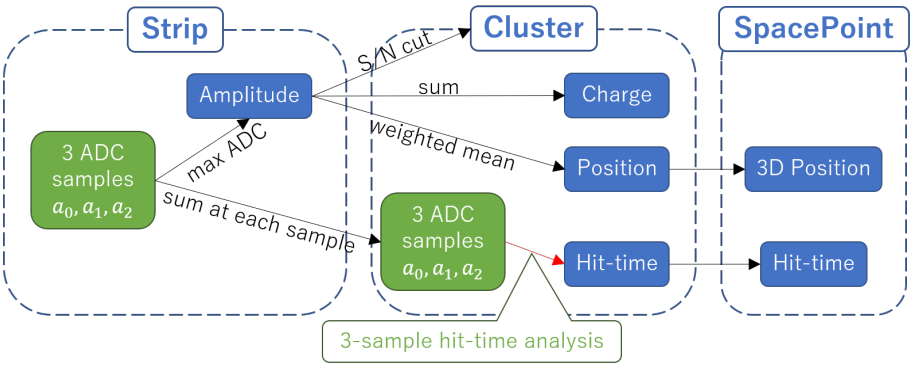

Fig. 5.1: Simplified diagram of SVD hit reconstruction in three-sample-mode data-taking. We calculate clustered three samples before the hit-time estimation.

5.2 Effect of trigger jitter on data-taking and its emulation

First, we discuss the effect of trigger jitter in the real data taking. In APV25, we only take the sample at each clock-signal. Then, the change of level-1 trigger timing by $\Delta t = 31$ ns should lead to the change of the SVD trigger by one clock-cycle. This is the only effect of the trigger jitter.

To discuss the trigger jitter effect in the more precise way, first we consider the ideal trigger, whose timing has no jitter and is not synchronized to clocks anymore. This ideal trigger timing can be written as

$$t_{\mathrm{TRG;ideal}} = t_{\mathrm{col}} + Const. \tag{39}$$

We simply assume that this ideal trigger is latched by the DAQ clock to give the level-1 trigger:

$$t_{\mathrm{TRG}} - \Delta t/4 \leq t_{\mathrm{TRG;ideal}} < t_{\mathrm{TRG}}. \tag{40}$$

By writing the level-1 trigger timing with the SVD trigger timing,

$$t_{\mathrm{TRG;SVD}} - (5 - i_{\mathrm{TB}}) \times \Delta t/4 \leq t_{\mathrm{TRG;ideal}} < t_{\mathrm{TRG;SVD}} - (4 - i_{\mathrm{TB}}) \times \Delta t/4. \tag{41}$$

Here $i_{\mathrm{TB}} \in \{0, 1, 2, 3\}$, thus

$$t_{\mathrm{TRG;SVD}} - 5 \times \Delta t/4 \leq t_{\mathrm{TRG;ideal}} < t_{\mathrm{TRG;SVD}} - \Delta t/4. \tag{42}$$

If $t_{\mathrm{TRG;ideal}}$ is within this range, the SVD trigger timing does not change and hence the three (or six) samples. This relation is drawn in Fig. 5.2. Here, the trigger jitter effect is not uniform; the effect is large if $t_{\mathrm{TRG;ideal}}$ is near the edge of the window, $t_{\mathrm{TRG;SVD}} - 5 \times \Delta t/4$ and $t_{\mathrm{TRG;SVD}} - \Delta t/4$.

Farther transformation leads to

$$t_{\mathrm{TRG;SVD}} - 5 \times \Delta t/4 \leq t_{\mathrm{col}} + Const. < t_{\mathrm{TRG;SVD}} - \Delta t/4 \tag{43}$$

$$t_{\mathrm{TRG;SVD}} - 5 \times \Delta t/4 \leq \mathrm{EventT0} + t_{\mathrm{TRG}} + Const. < t_{\mathrm{TRG;SVD}} - \Delta t/4 \tag{44}$$

$$-5 \times \Delta t/4 \leq \mathrm{EventT0} - (4 - i_{\mathrm{TB}}) \times \Delta t/4 + Const. < -\Delta t/4 \tag{45}$$

$$0 \leq \mathrm{EventT0} + i_{\mathrm{TB}} \times \Delta t/4 - t_0 < \Delta t \tag{46}$$

$$t_0 \leq \mathrm{T0{+}TB} < t_0 + \Delta t \tag{47}$$

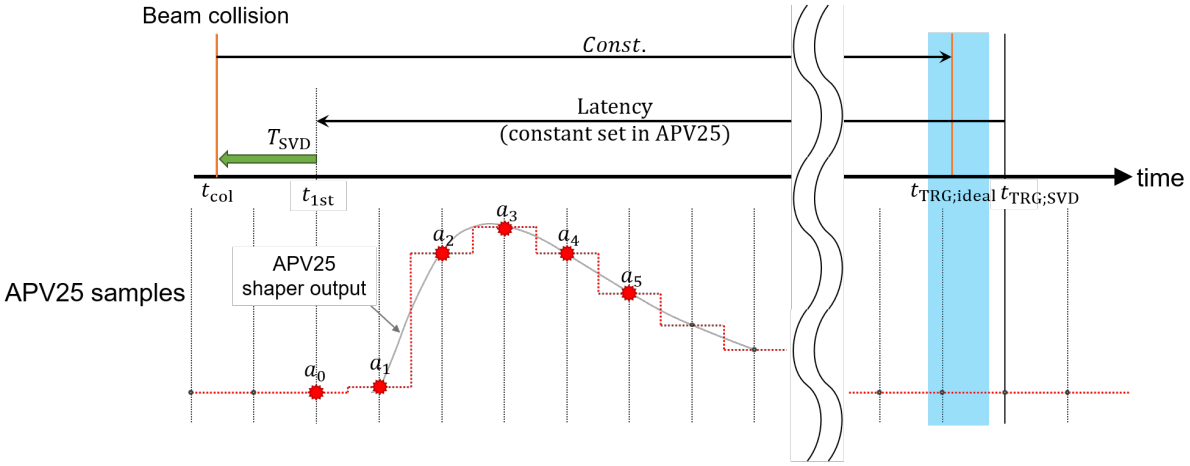

Fig. 5.2: The timing relation between $t_{\mathrm{TRG;ideal}}$, $t_{\mathrm{TRG;SVD}}$, and $t_{1\mathrm{st}}$. The $t_{\mathrm{TRG;SVD}}$ in this image corresponds to the $t_{\mathrm{TRG;ideal}}$ in light-blue region.

Here we substitute reconstructed collision timing EventT0 ($+t_{\mathrm{TRG}}$) for t_{col}. In the one line before the last, we combine all the constant terms into t_0, which corresponds to the position of the time-window(the left edge of the light-blue region in Fig. 5.2).

This time-window does not need to be synchronized to the SVD system clock. We can tune the position of the time-window using TB information. For example, we add a delay of one clock only for $i_{\mathrm{TB}} = 3$, then the window shifts $\Delta t/4$ before. Moreover, it does not need to be synchronized to the DAQ clock if the trigger has TOP timing; it can be tuned with the fine-timing information of $\Delta t/16$. For simplicity, we assume that we can tune this time-window t_0 continuously.

By using this time-window in Eq. 47, we can emulate the ideal trigger by T0+TB. For example, we choose to take $[a_0, a_1, a_2]$ if T0+TB is in the range as in Eq. 47. If the T0+TB is larger than $t_0 + \Delta t$ but smaller than $t_0 + 2\Delta t$, which corresponds to the later issue of the trigger, we take $[a_1, a_2, a_3]$. In this way, we can emulate the trigger timing with a very small jitter of 0.65 ns (EventT0 resolution) by using T0+TB. The more detailed application is shown in Eq. 49 and 50.

Moreover, we can apply trigger jitter on $t_{\mathrm{TRG;ideal}}$ by applying the jitter on T0+TB. Here we add some random jitter generated according to one Gaussian with a specific σ to the T0, which results in the jitter σ on $t_{\mathrm{TRG;ideal}}$. In this way, we can also emulate the trigger with an arbitrary size of jitter and hence we can evaluate its effect.

The tuning of this time-window t_0 corresponds to the tuning of the latency. To get the ideal latency, we tune t_0 for the MaxSum algorithm. As a result, we have

$$t_0 = -22.40 \text{ ns}. \tag{48}$$

The detailed explanation can be found in Appendix E.

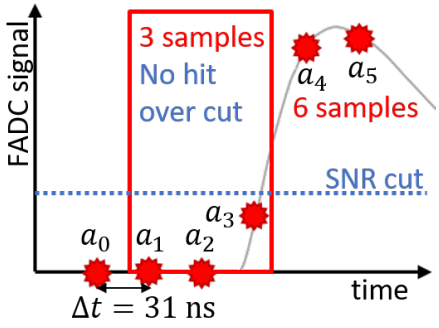

Fig. 5.3: A picture for the three-sample-mode data taking for the off-time hit. In this case, there is no hit over the S/N cut in the three samples, thus we lose the hit.

5.3 Performance study

Finally, we evaluate the performance of SVD reconstruction under the emulated three-sample mode. We analyze three-sample data selected with the above time-window emulated by T0+TB values, assuming the trigger-timing jitter of 0 ns (no jitter), 5 ns, 7 ns, 10 ns, 15 ns, and 20 ns. The current finest trigger (ECL timing) has a jitter around 5 ns in RMS for Bhabha events and 7 ns for hadron events. The original six-sample-mode data used in this study is the same as in the calibration (Section 3.5.2).

Unfortunately, the three samples selected with the above method are not ideal in the point that they are restricted to the original six samples. If the EventT0 value is too small, we cannot take (-1, 0, 1) or earlier samples and instead take (0, 1, 2). As we see in Fig. 6.8, in most of the event i of max. sum is 1 or 2, thus such a three-sample selection leads to higher signal efficiency. To estimate such trigger jitter effect, we expand a_i for samples earlier than 1st sample a_0 with 0 ADC value, namely $a_i = 0$ for $i < 0$, while for the samples later than sixth sample a_5 we keep our current method. This is because we have only noise before the arrival of the signal, while we have a large tail after the signal. The three samples are selected as:

$$\begin{cases} [a_{i-1}, a_i, a_{i+1}] & i < 4 \\ [a_3, a_4, a_5] & i \geq 4 \end{cases} \quad \left(i = \left\lfloor \frac{\text{T0+TB}-t_0}{31 \text{ ns}} \right\rfloor + 1 \right). \tag{49, 50}$$

As we discussed in Section 5.1, we analyze the strip amplitudes, cluster charge, cluster position, cluster hit-time, the signal efficiency, and the background rejection with time-cut as the SVD reconstruction performance. Additionally, we see the background rejection without time-cut, i.e. background rejection of three-sample selection, like the signal efficiency. We devote one section for each of the parameters.

5.3.1 Background rejection

We applied the three-sample selection on the strip hit (or RecoDigit) level. The same S/N cut as six sample reconstruction is applied to these three samples. This loss of samples possibly leads to loss of hit after the S/N cut. The image of such loss of hits for the off-time hit is shown in Fig. 5.3. In such a case, 'the loss of hits' means 'the rejection of background hits'. Here we

define the hit efficiency $\epsilon_{3/6}$ (NOT the signal efficiency) at the cluster level as

$$\epsilon_{3/6} = \frac{|\text{clusters reconstructed in the three-sample-mode data emulated from the six-sample-mode data}|}{|\text{clusters reconstructed in the six-sample-mode data}|}. \tag{51}$$

There are some cases where we get multiple three-sample clusters for an identical six-sample cluster. The distribution of the number of three-sample-mode clusters found in a six-sample-mode cluster is checked in the signal. Figure 5.4 shows the distribution. As this shows, the probability to split a single six-sample-mode cluster into multiple three-sample-mode clusters is negligibly small (<0.1%). Just to be on the safe side, we allow multiple counts of the split clusters not to overestimate the background rejection performance. Note that this treatment of the multiplication of clusters is different in the signal efficiency analysis.

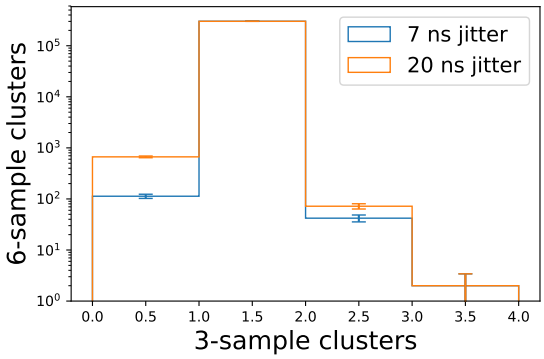

Fig. 5.4: The log-scaled distribution of the number of three-sample clusters reconstructed from one six-sample cluster in the signal (see Table 4). The errors are calculated according to the standard deviation of the Poisson distribution, i.e. the square-root of the number of entries. Around 99.9% of six-sample clusters are reconstructed as one three-sample cluster.

The background rejection performance is expressed as $1 - \epsilon_{3/6}$ for background data. The data for the background clusters are taken with 2 Hz random triggers in the same run, to ensure that we have the same background condition. The estimated background rejections for several trigger jitters are plotted in Fig. 5.5. The difference of ~0.5% for 20 ns trigger jitter is negligibly small compared to the absolute value of rejection ~30%. Here, we regard these deviations as systematic uncertainties, then we can say that the background rejection by the three-sample mode is not affected by the trigger jitter.

The reason for this stability can be easily understood: the hit rate of the beam background is thought to be constant for the time and the width of the time-window does not affect by the trigger jitter. Thus, the time-integrated rate of background is constant for the trigger jitter. While the rejection rate ~30% does not seem to be explained by this time window shrink at first sight (naively 6 to 3 would cause ~50% rejection), this can be explained with the tail background: if the amplitude of the background is higher enough, the signal earlier to the time-window could also create the hit even from the outside of the window.

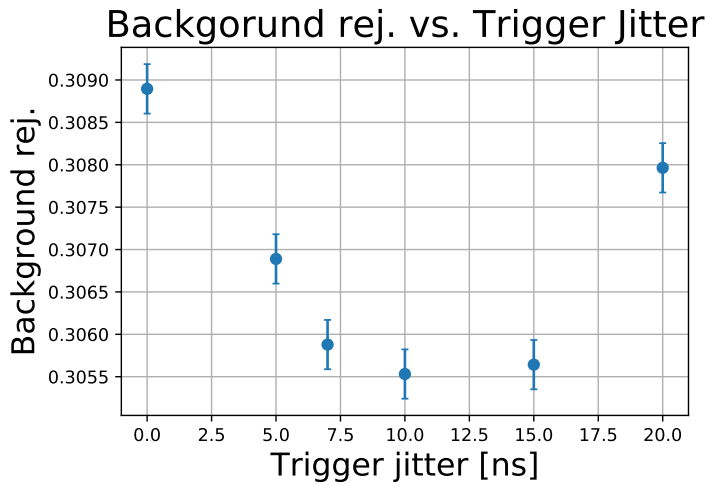

Fig. 5.5: Backgournd rejection of three-sample selection for various trigger jitters. The errors on the points are calculated as the Bayesian interval (CL=0.683) for the uniform prior. Note that the difference between the highest and the lowest ticks is only 0.5%. The dependence for the trigger jitter is negligibly small.

5.3.2 Signal efficiency

The loss of the hit due to the three-sample selection is not only observed in the background hits but also the signal hits. This means we lose the signal efficiency by this selection. The signal efficiency is directly expressed by $\epsilon_{3/6}$ in the signal data. In contrast to the background rejection calculation, here we treat multiple three-sample clusters for an identical six-sample cluster as just one count, not to overestimate the signal efficiency (though the effect is very small as in Fig. 5.4). For this efficiency analysis, only clusters created by real tracks from the IP are used. Also, signal selections for the events and the tracks are applied as in Section 3.5.3, listed in Table 4.

Then, we can get the signal efficiency as plotted in Fig. 5.6. Overall the signal efficiency decreases for increasing trigger jitter. This can be explained that the larger trigger jitter causes the larger shift of the three-sample time-window from the signal hit-time, leading to the more signal out of the time-window. From Fig. 5.6, the signal efficiency is $99.943 \pm 0.004\%$ even with 15 ns trigger jitter. The impact on efficiency is only visible when the jitter exceeds $\Delta t/2 = 16$ ns. We can conclude the hit clusters are almost not lost with the three-sample-mode data taking using triggers with trigger jitter less than 15ns.

To summarize, we confirm no substantial degradation on the signal efficiency and the background rejection due to the trigger jitter of fewer than 10 ns achieved in the future level-1 trigger timings, and most of the existing level-1 trigger is also allowable.

5.3.3 Strip amplitude performance

The strip amplitude is the fundamental parameter of the three-sample-mode data-taking. It is important to confirm the quality of the sampling.

To estimate the amplitude performance of the strip, we calculate the amplitude ratio, (amplitude in three-sample-mode data-taking)/(amplitude in six-sample-mode data taking), then take

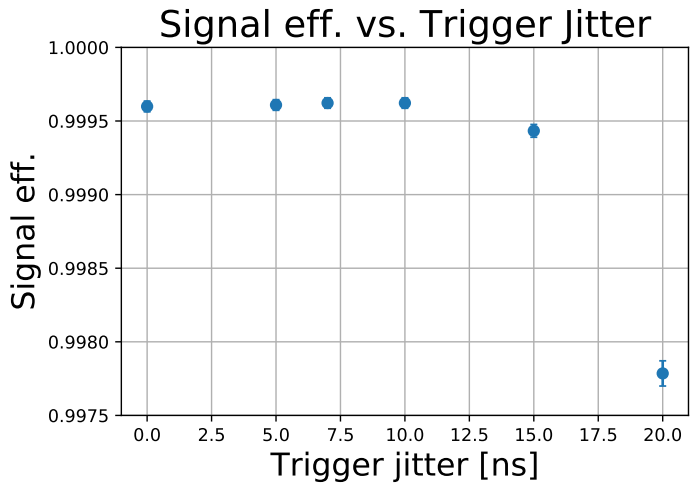

Fig. 5.6: Three-sample selection efficiency for various trigger jitters. The errors on the points are calculated as the Bayesian interval (CL=0.683) for the uniform prior. The efficiency decreases for the larger trigger jitter.

the average. The results are summarized in Fig. 5.7. With 10 ns jitter, we still have 99.0% of the six-sample amplitude at the strip level. Even with 20 ns jitter, we achieve 97.5% of the strip amplitude. Thus, we confirm the validity of this analysis with trigger jitter up to 20 ns, i.e., the data-taking at such a high jitter does not completely collapse the performance.

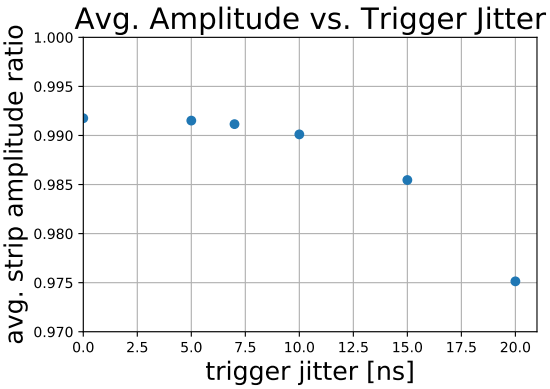

Fig. 5.7: The average of the ratio between the three-sample strip amplitude and the six-sample strip amplitude.

5.3.4 Cluster hit-time resolution

Using the three ADC samples of the three-sample-mode data emulated from the six-sample-mode data, we can estimate the hit-time with the methods introduced in Section 3.4: CoG3 and ELS.

For the hit-time resolution, we first check the correlation between $T_{\mathrm{SVD;raw}}$ and T0+TB−FF. The 2-dimentional correlations for no jitter, 10 ns jitter, and 20 ns jitter and for the CoG3 and ELS timing calculations are plotted in Fig. 5.8.

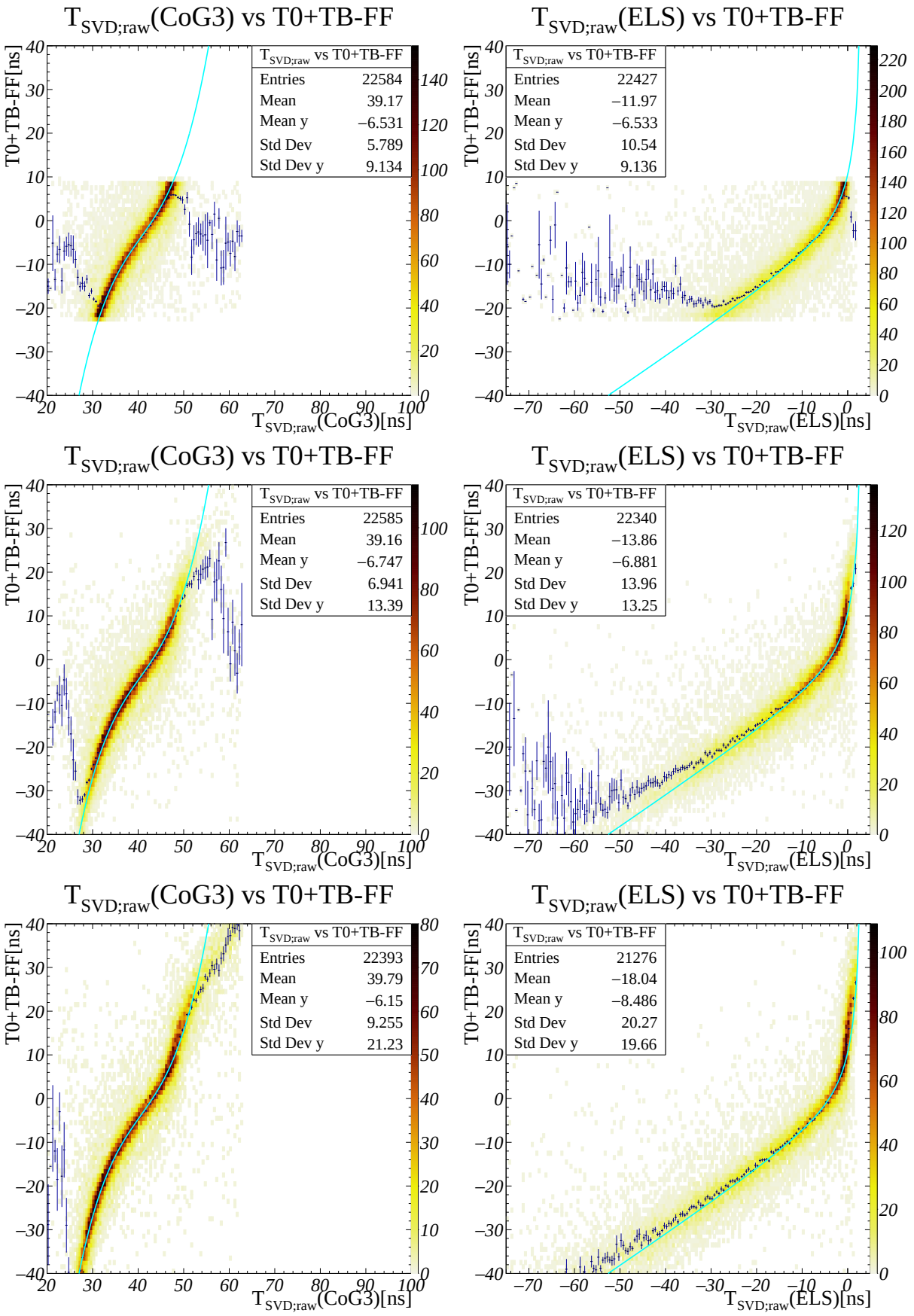

Fig. 5.8: Correlation between $T_{\mathrm{SVD;raw}}$ and T0+TB−FF in emulated timing (left: CoG3, right: ELS, upper: no jitter, middle: 10 ns jitter, lower: 20 ns jitter). The dark-blue point shows the mean of the T0+TB−FF distributions at each $T_{\mathrm{SVD;raw}}$ bin, with an error calculated by its standard deviation divided by the square root of the total entries. The blue line represent the fit curve in *maximum sample at the latter*.

In the correlation with no jitter, we have no entries outside the region $[t_0, t_0 + 31\ \mathrm{ns}]$ in the T0+TB−FF distribution. This arises from our selection algorithm using T0+TB. Transforming Eqs. (49) and (50), in terms of the 1st frame correction FF,

$$\mathrm{FF}/\Delta t = \begin{cases} \left\lfloor \dfrac{\mathrm{T0} + \mathrm{TB} - t_0}{\Delta t} \right\rfloor & \text{if } \left\lfloor \dfrac{\mathrm{T0} + \mathrm{TB} - t_0}{\Delta t} \right\rfloor < 3 \\ 3 & \text{otherwise} \end{cases}. \tag{52}$$

(53)

If we ignore the contribution from Eq. (53) (which has smaller statistics as shown in Fig. 6.8), we can get the simple relation:

$$\mathrm{FF}/\Delta t = \left\lfloor \frac{\mathrm{T0} + \mathrm{TB} - t_0}{\Delta t} \right\rfloor \tag{54}$$

$$\mathrm{FF}/\Delta t \leq \frac{\mathrm{T0} + \mathrm{TB} - t_0}{\Delta t} < \mathrm{FF}/\Delta t + 1 \tag{55}$$

$$\mathrm{FF} \leq \mathrm{T0} + \mathrm{TB} - t_0 < \mathrm{FF} + \Delta t \tag{56}$$

$$t_0 \leq \mathrm{T0} + \mathrm{TB} - \mathrm{FF} < t_0 + 31\ \mathrm{ns}. \tag{57}$$

Then we can derive the constraint appears in the distribution. This constraint affects the 1-dimensional projection distribution of T0+TB−FF at each $T_{\mathrm{SVD;raw}}$ bin, and the mean of the distribution does not match to the correlation, shown in Fig. 5.8 with the dark-blue points. Here, we should not fit the function to the mean of the correlation. Throughout this study with and without trigger jitter, we use the fit function obtained in Section 3.5.2 for the MaxSum-selected samples. This fit function is also plotted in Fig. 5.8. We can see that the calibration well matches the correlation.

With the 10 ns trigger jitter, we have wider T0+TB−FF distribution, though we have still some distortions on the shape. One concern is that our calibration function shape does not fit well around $T_{\mathrm{SVD;raw}} = 0$ in ELS. This is because the range of $T_{\mathrm{SVD;raw}}$ is wider than that in the MaxSum-selected samples, and the extrapolation of the fit function does not behave well near the pole.

If we see the 20 ns jitter result, we have almost no distortion in the T0+TB−FF distribution. Though the calibration does not perfectly agree to the distribution, we keep using the same calibration as above: though it could be possible to perform the calibration using these data, we will not use the three samples at such a large trigger jitter.

To perform the calibration we decide to use in this analysis in the real setup, we have to take the six-sample-mode data for the calibration, along with the three-sample-mode data. This is straightforward if we use the three-sample-mode only for fine-timing triggers. In this case, we can use, for example, six-sample-mode data in Bhabha events for calibration. If we plan to take only three samples for any trigger, we can get in trouble because our usual calibration method does not work, as we see in Fig. 5.8. One possible solution is to perform the calibration for the inverse function of g by fitting to the mean of $T_{\mathrm{SVD;raw}}$. These studies are left for future studies.

Using the calibration functions, we obtain T_{SVD} from $T_{\mathrm{SVD;raw}}$. The timing resolution of T_{SVD} can be evaluated from the distribution of $T_{\mathrm{SVD}} + \mathrm{FF} - \mathrm{TB} - \mathrm{T0}$, with the same technique used in Section 3.5.3. These distributions are drawn in Fig. 5.9. Here, we have a smaller height of the peak and the larger tail with higher jitter. This can be evaluated by the total σ of the fitted double-Gaussian, plotted in Fig. 5.10.

One of the characteristics of these distributions is that only the right tail for CoG3 and the left for ELS is affected by the trigger jitter. This effect is already visible at the 10 ns jitter

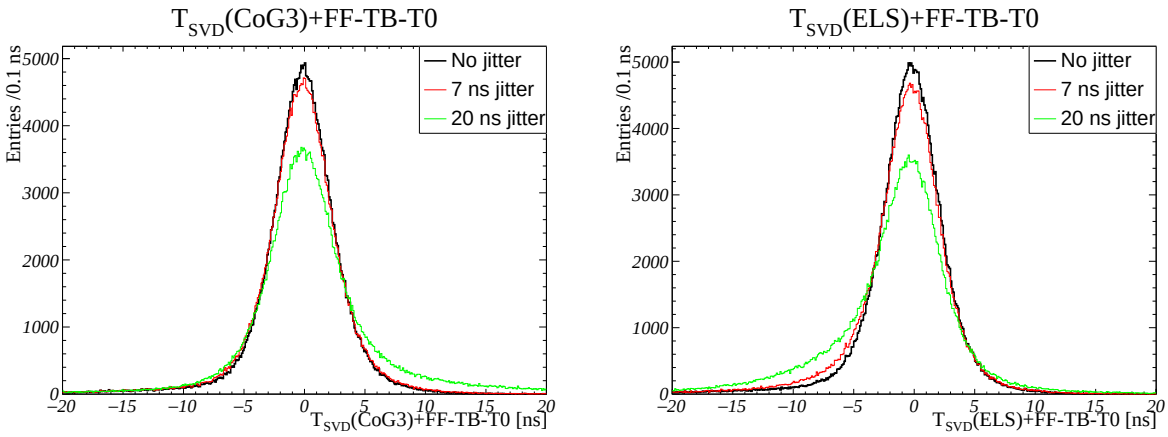

Fig. 5.9: Total distribution of $T_{\mathrm{SVD}} + \mathrm{FF} - \mathrm{TB} - \mathrm{T0}$ in emulated three-sample-mode data taking. As examples, the distributions at the trigger jitter of 0 ns, 7 ns, 20 ns are plotted. The width of this distribution approximately corresponds to the resolution of the SVD hit-time.

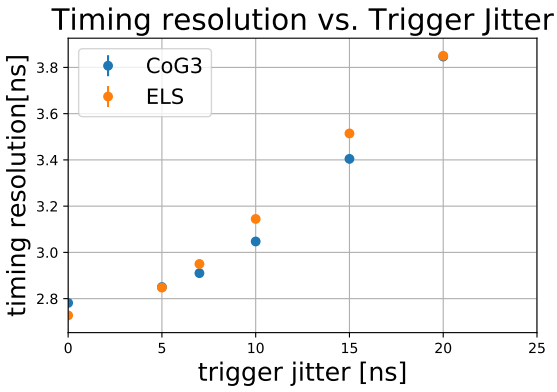

Fig. 5.10: The total σ's of the fitted double-Gaussian for the distributions in Fig. 5.9. The errors are estimated by those of standard deviation (Eq. 58), which are smaller than the size of points.

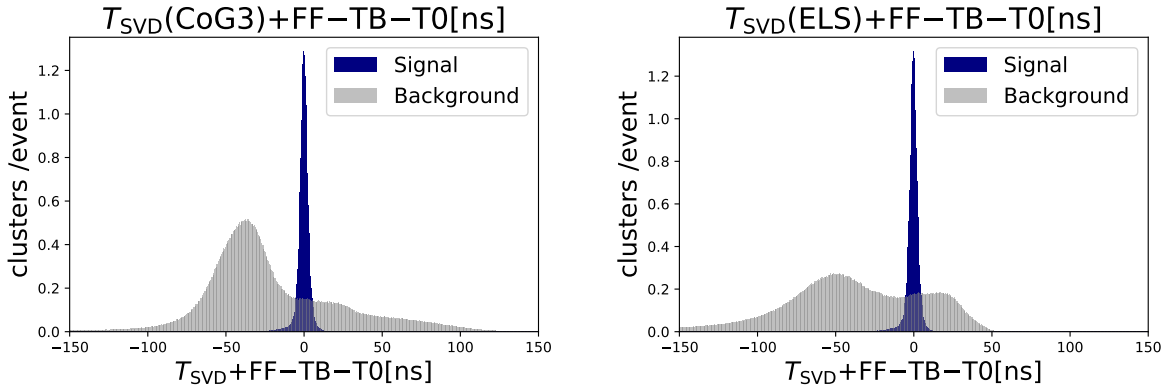

Fig. 5.11: Total distribution of $T_{SVD} - TB - T0$ in emulated timing (signal distribution (navy) and background distribution (gray) are shown). The distributions are normalized with the number of triggers (or events) in the count.

for ELS, and we confirm that this tail comes from the bias in calibration around $T_{SVD} = 0$, as mentioned above. For the CoG3, we cannot see such a discrepancy between the calibration and the correlation in the data with 10 ns jitter. However, we can confirm such a discrepancy in the data with 20 ns jitter. In the bottom-left plot in Fig. 5.8, the correlation cannot be expressed in pol 3, and there is a clear disagreement around $T_{SVD} = 30$ and 50–60 ns. Thus, the tail-growing effects in both CoG3 and ELS are due to the calibration failure with large jitter.

5.3.5 Background rejection with time-cut

The trigger jitter effect should be checked also in the background rejection performance. We first check the timing distribution of background and signal, shown in Fig. 5.11. The cut for the signal selection is summarized in Table 4 and the background is taken from the random trigger with 2 Hz. As in Section 4.2.2, we use randomly generated EventT0 to emulate the T0 correction on the background hit-time.

Here we simply apply the symmetric cut from the signal peak: we assume that calibration works well and the cut is reduced to simple symmetric cut $[-c, +c]$. The background rejection as a function of the full width of the timing cut is plotted in Fig. 5.12. Note that the background rejection and signal efficiency here do not include those by three-sample selection: they are calculated after the selection. Here we have almost the same rejection performance for different trigger jitters, which decreases almost linearly with the width of the time cut.

With these cuts, we can at least keep the signal efficiency plotted in Fig. 5.13. The difference between CoG3 and ELS comes from the NaN in ELS calibration. We have higher background rejection and lower signal efficiency for ELS. We can confirm that the timing resolution is precise enough for rejecting the off-time background. For example, in CoG3, if we have 10 ns jitter, we can ensure the 99.5% signal efficiency with (-30, 30) ns cut, leading to 65% background rejection. With these two plots for two methods, we can apply the timing cut depending on the background condition and the trigger jitter. As a comparison, the current performance in the six-sample is discussed in Section 4.2.3.

To get a rough estimation for the tracking performance studied in Section 4.4, we compare the performance of this cut with that in MC, actually used to evaluate the tracking performance.

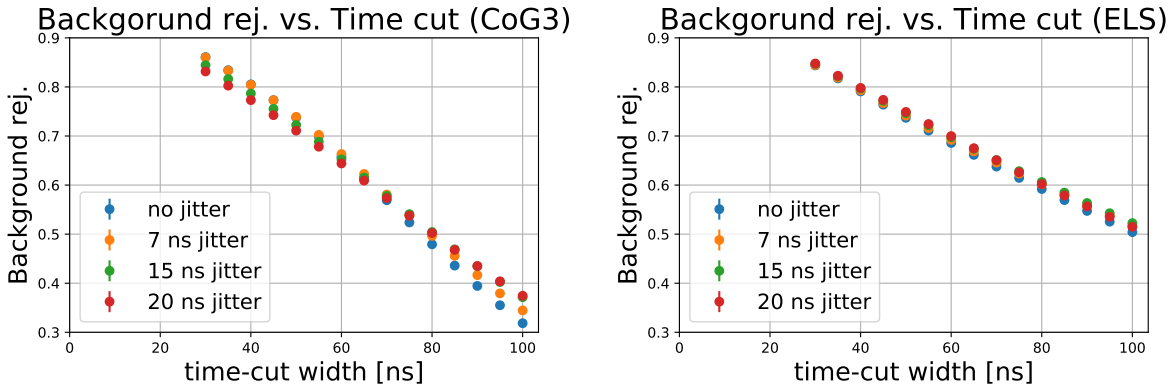

Fig. 5.12: Backgournd rejection of timing cut respect to the full width of the timing cut [ns] for each trigger jitter (omitting 5 ns and 10 ns for visibility). For example, the width 30 ns corresponds to the cut (-15, 15) ns on the timing distributions in Fig. 5.11. The errors at each jitter are calculated as the Bayesian interval (CL=0.683) for the uniform prior. The plotted error bars are small and almost invisible.

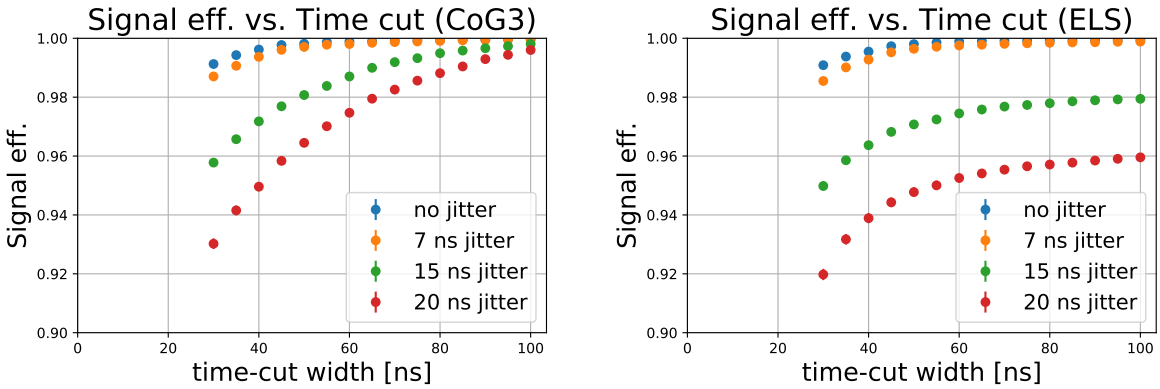

Fig. 5.13: calibration + timing cut efficiency respect to the full width of the timing cut for each trigger jitter (omitting 5 ns and 10 ns for visibility). For example, the width 30 ns corresponds to the cut (-15, 15) ns on the timing distributions in Fig. 5.11. The errors at each jitter are calculated as the Bayesian interval (CL=0.683) for the uniform prior. The plotted error bars are small and almost invisible.

For this comparison, we need to take into account the signal efficiency and background rejection of three-sample selection itself, or $\epsilon_{3/6}$, discussed in Section 5.3.1 and 5.3.2. By combining the results, we can get the performance plot, i.e., the relation between the signal efficiency vs the background rejection, as shown in Fig. 5.14. From this plot, we can conclude that, with less than 10 ns jitter which we will achieve in the future, the time-cut performance is comparable to that in the performance study, i.e., we can recover the tracking performance even in the three-sample-mode.

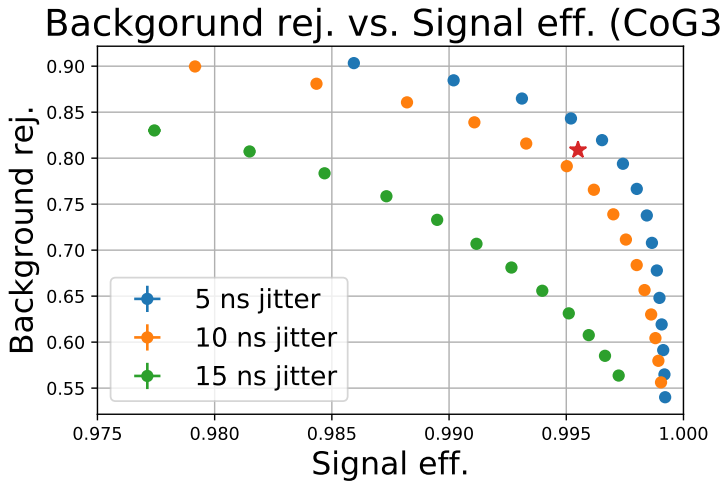

Fig. 5.14: The relations between signal efficiency and background rejection for each trigger jitter (omitting 0, 7, 20 ns for visibility), considering $\epsilon_{3/6}$, calibration efficiency, and timing-cut. Each plotted points stand for one timing cut with a certain width, which is plotted in Fig. 5.12 and 5.13. The red star stands for the cut applied for the tracking performance study in MC. The errors at each jitter are calculated as the combined errors of $\epsilon_{3/6}$ and the time-cut + calibration efficiency.

5.3.6 Cluster charge

We estimate the amplitude by the largest ADC value among the sampled ADC values. With the trigger jitter, we are more likely to lose this largest sample in the three-sample time-window.

For the amplitude, we first check the differences in cluster amplitude distribution, which are shown in Fig. 5.15. The shape of the distribution is not affected much.

Furthermore, we can check the sum of all amplitudes in the run, normalized with that of 6 samples. The results are shown in Fig. 5.16. The value at each trigger jitter is almost identical to that of the strip amplitude. Even with the 10 ns jitter, we can achieve the high ratio of gathered charges as 99.1%, which corresponds to the signal efficiency of around 99.98%. Here signal efficiency is more important for data-taking, so such a small loss of amplitude is not problematic.

We can say that as a total, we can correct charges well even with the trigger jitter. This is promising also for the performance of SVD dE/dx PID.

5.3.7 Cluster position

Another purpose of the SVD amplitude is to estimate the cluster position.

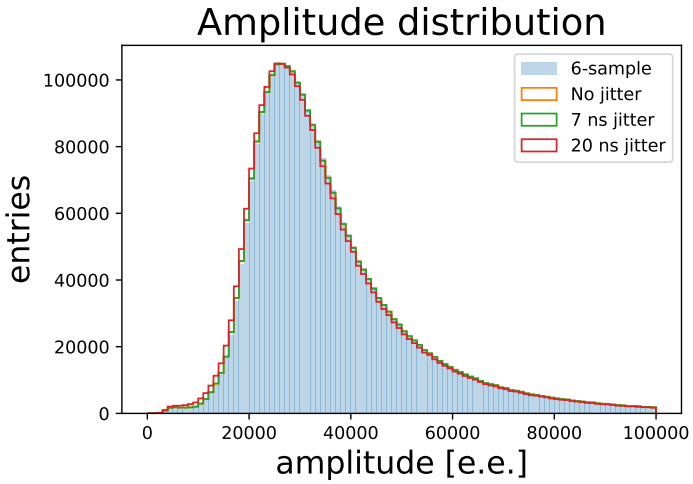

Fig. 5.15: The distribution of cluster amplitude in emulated timing for each trigger jitter. The unit *e.e.* stands for the *electron equivalent*.

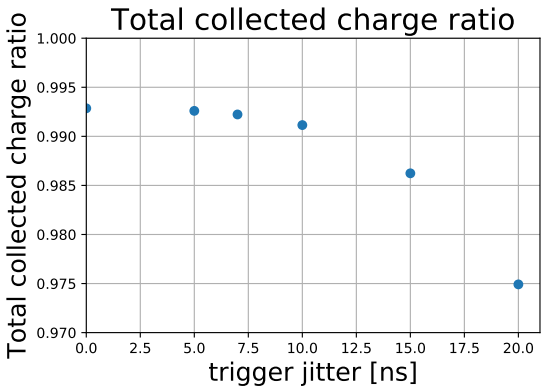

Fig. 5.16: The ratio of collected charge respect to that of 6 samples vs trigger jitter.

We see the distance between the three-sample-mode clusters and the original six-sample-mode clusters. The resulting distribution at 7 ns jitter is shown in Fig. 5.17, as an example. The distance for most of the clusters is equal to 0, which is consistent with the tiny difference we see in strip amplitudes (Section 5.3.3) or cluster charges (Section 5.3.6). This standard deviations at various trigger jitters are plotted in Fig. 5.18. The errors are estimated by

$$\text{var}\,\sigma^2 = \frac{1}{n}\left(\beta_2 + 2\right)\sigma^2, \tag{58}$$

where n for data entries, β_2 for kurtosis (β_2=0 for Gaussian) [19]. As you see in Fig. 5.17, the distribution has a large kurtosis, hence the error on the standard deviation is also large accordingly. An important note is that the original six-sample-mode data are the same at any trigger jitter, thus we have some correlation in the error. We can see a slight increase in the standard deviation as the trigger jitter increases, as expected. However, the differences between 10.7 μm without jitter and 12.4 μm at 20 ns jitter are small considering the current SVD position resolution of around 20 μm [20]. We can conclude that the position resolution is not largely affected by the trigger jitter.

The absolute value of around 10 μm is caused by the small but long tail. One possible explanation of such a large deviation is the split three-sample-mode cluster: a six-sample-mode cluster is split into two or more three-sample-mode clusters where only one of those is the true cluster and the others are caused by background or noise. In such a case, our tracking performance will not be deteriorated even we have a large standard deviation. To remove such effects, we need to measure the residual between the position of the track and the nearest cluster. The evaluation of this residual is left for our future study.

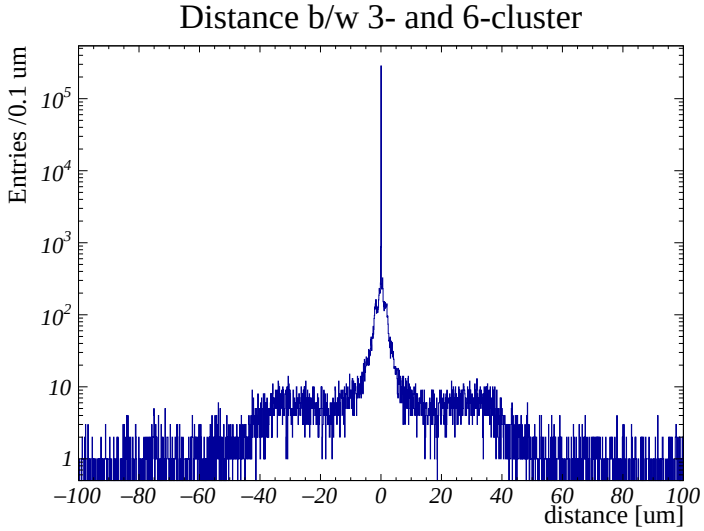

Fig. 5.17: The distance between the six-sample-mode and the three-sample-mode clusters at 7 ns jitter. Note that the y-axis is log-scaled.

5.4 Data rate reduction and the safety factor

From these studies, we can allow the ECL trigger jitter for hadron events with 7 ns jitter. In the future where the trigger jitter is less than 10 ns for all types of the trigger, we will be able to use

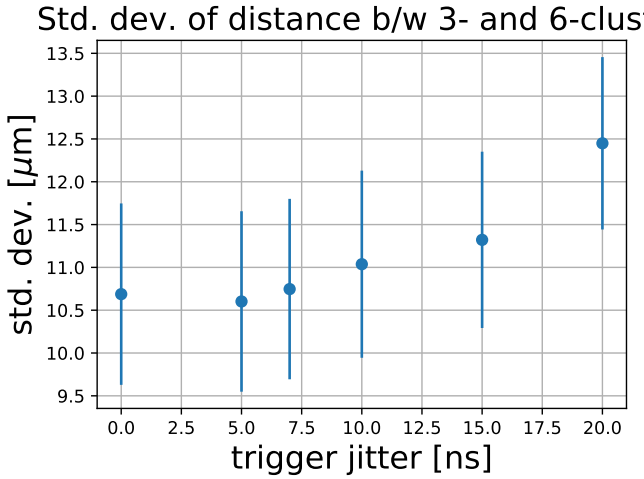

Fig. 5.18: The standard deviation of the distance between the six-sample-mode and the three-sample-mode clusters. The error bars are calculated from the variance of σ^2 in Eq. 58.

the three-sample-mode in data-taking for 100%.

In this case, the data from the beam backgrounds are reduced to (100% − 30%)/2 and the signal and the electrical noise also decrease by a factor of two. The data rate at the bottleneck, ROPC output, in this condition are shown in Fig. 5.19, compared to that without the three-sample-mode in data-taking[16]. We enough reduce the data sample and achieve safety factor of eight for the current limitation of ROPC output. Thus, with the implementation of the three-sample-mode in data-taking, we do not need to concern about the data rate anymore.

In addition to this data-size reduction, we can suppress the trigger loss as described in Section 2.1. The dead rate due to APV25 trigger veto system is expected to decrease from 3.30±0.02% to 0.563±0.007% [8].

[16]In case we cannot use three-sample-mode for 100% trigger, we can estimate the data rate by taking the internal division of the two data rates plotted in Fig. 5.19.

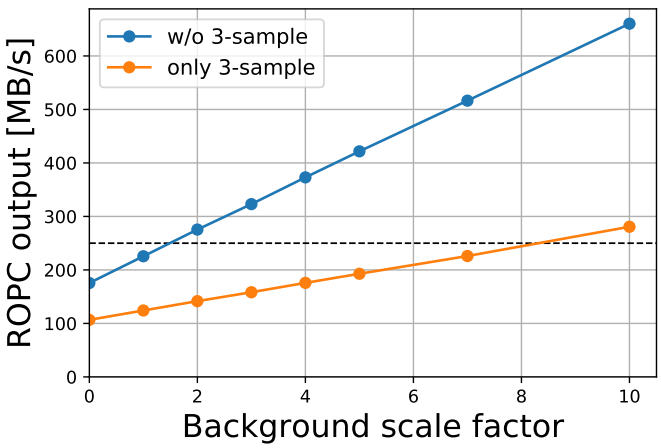

Fig. 5.19: The expected data rate at the COPPER output and ROPC output. The orange line for the results with the three-sample-mode only, the blue line for the results without the three-sample-mode, and the black-dashed line for the current bandwidth.

Chapter 6
Conclusion

6.1 Achievements

The Belle II experiment aims to probe new physics with the intense, focused, and high-current beam of SuperKEKB. The beam background condition expected in the MC simulation at the design luminosity (the occupancy of 1.7% in Layer 3) will be acceptable for the SVD systems in terms of online data readout and offline data analysis, without enough safety factor. Although the future background condition is difficult to estimate, the recent more reliable study predicts 7.0% occupancy in Layer 3, corresponding to five times larger background than the simulation. In this study, based on this estimation, we aim to improve the safety factor of five by developing new features in the data readout and offline analysis.

High occupancy caused by the beam-background hits will increase the data size of the SVD. To reduce the data size into less than a half, we newly develop the three-sample-mode in data-taking instead of the current six-sample-mode. The performance in this new mode of data-taking is evaluated with the emulated three-sample-mode data from the Belle II experiment data in the spring of 2019. For this performance study, we develop a new method to estimate hit-time, which can be used to analyze the three-sample-mode data. The resulting hit-time resolution is around 2.5 ns when analyzing six-sample-mode data, which is excellent compared to the sampling period of 31.4 ns. As a result, we confirm the excellent efficiency of 99.96±0.01% for the physics signals, the rejection factor of 30.57±0.03% for the beam-background signals, and the good charge collection of 98.6%, assuming 15 ns jitter. This jitter can be satisfied with almost 100% of the trigger in the future update. This results in a reduction of the data size into 34.72±0.02% for the background. We can conclude that the three-sample-mode in data-taking is a viable option to reduce the data size. With the implementation of this three-sample mode, the requirements on the background will be loosened, from the safety factor of five to over ten on the nominal beam background at the trigger rate of 30 kHz.

Another concern of the occupancy increase is the degradation of the tracking performance. In this study, a new hit selection using the hit-time information in the offline analysis is developed. Here, the new method developed during the above study is used to estimate this hit-time. The performance of this selection is evaluated and validated using the experimental data. We confirm the rejection factor of 88.51±0.02% (CoG3) or 88.20±0.02% (ELS) for the beam background, and the efficiency of 99.57±0.01% (both CoG3 and ELS) for the physics signals. The improvement in the tracking performance due to this selection is evaluated in the MC simulation with scaled backgrounds. As a result, with the background scaled by a factor of five, the track-finding efficiency is improved from 30% to 89.3±0.3%, and the fake rate is suppressed from 76% to 31.4±0.4%, with 70 ns wide time-cut. By applying this cut, the tracking performance gets more stable to the background condition. We confirm the safety factor of almost five on the beam background to keep the track-finding efficiency over 90%. We also confirm the comparable time-cut performance to the MC in the three-sample-mode with the 10 ns jitter. Thus, we can use this background rejection also in the three-sample-mode.

As a result, we will be able to achieve the safety factor of almost five for the simulated background at the design luminosity by these two modifications: the three-sample-mode in data-taking and the hit selection using the hit-time information. Although the estimation on the

background condition includes substantial uncertainties, we confirm that SVD can be operated stably in the background condition at the design luminosity. The methods developed in this study and the results of the expected performance will be essential in the coming operation of the Belle II experiment at the design luminosity of SuperKEKB.

6.2 Remaining studies

Some more studies and the implementation remain to be done to realize the stable operation of SVD. These works are listed below:

- The developed three-sample analysis method ELS can give an estimation on the amplitude A as well as the hit-time T_{SVD}, though not used in this study. By using this new amplitude estimation, we may be able to improve performance, such as efficiency and position resolution.
- We need to implement the three-sample-mode in the real setup. First, we will implement the data-taking algorithm on the FADC firmware, then test it on a test bench.
- To confirm the tracking performance more solidly, we need to study the performance other than the SVD standalone tracking, i.e., the track extrapolation performance from CDC.
- The implementation of the developed methods of hit-time estimation to the real software framework is also important so that every collaborator can use and confirm the validity.
- The optimization of the time-cut in the hit-selection is important because the tracking performance still limits background tolerance.
- The evaluation of the residual in three-sample-mode data-taking is important to confirm the position resolution.

Acknowledgements

I first thank Prof. Yutaka Ushiroda for supervising me generously and responsibly and correcting my writings including this thesis.
I thank Dr. Katsuro Nakamura for always taking care of my whole work and advising me in detail, including the technical subject such as writing skills. I thank Dr. Koji Hara, Dr. Toru Tsuboyama and for kindly helping me and advising me in the study. I also thank all the colleagues in the SVD group, especially those working on the offline software, for guiding me with the method of analysis in the complex framework.
I thank Hikaru Tanigawa for advising me in the detail of the analysis and explaining me about the beam backgrounds.
I thank Dr. Taichiro Koga and the TRG group for discussing the trigger timing resolution together.
I appreciate Prof. Naohito Saito and Prof. Satoru Yamashita undertaking the vice committees of this thesis.
I thank K. Nakamura, T. Tsuboyama, K. Hara, H. Tanigawa, Bae Hanwook, Ryohei Sugiura, Kosuke Furui, Kota Nakagiri, Takuto Kunigo, Qi-Dong Zhou, Miki Nishimura, and Nobuhiko Sato, who all make my life in Tsukuba enjoyable.
Finally, I thank my family for their lifelong support.

References

[1] M. Tanabashi et al. Review of particle physics. *Phys. Rev. D*, 98:030001, Aug 2018. and 2019 update.

[2] Yosef Nir. CP violation. *Conf. Proc.*, C9207131:81–136, 1992.

[3] David Atwood, Michael Gronau, and Amarjit Soni. Mixing-Induced CP Asymmetries in Radiative B Decays in and beyond the Standard Model. *Physical Review Letters*, 79(2):185–188, Jul 1997.

[4] E. Kou, P. Urquijo, et al. The Belle II Physics Book, 2018.

[5] `https://www.kek.jp/ja/imagearchive/images/20180320_superkekb_002.png`.

[6] Kazunori Akai, Kazuro Furukawa, and Haruyo Koiso. SuperKEKB collider. *Nuclear Instruments and Methods in Physics Research Section A: Accelerators, Spectrometers, Detectors and Associated Equipment*, 907:188 – 199, 2018. Advances in Instrumentation and Experimental Methods (Special Issue in Honour of Kai Siegbahn).

[7] P.M. Lewis, I. Jaegle, H. Nakayama, A. Aloisio, F. Ameli, M. Barrett, A. Beaulieu, L. Bosisio, P. Branchini, T.E. Browder, and et al. First measurements of beam backgrounds at SuperKEKB. *Nuclear Instruments and Methods in Physics Research Section A: Accelerators, Spectrometers, Detectors and Associated Equipment*, 914:69–144, Jan 2019.

[8] H. Tanigawa. A study of beam background from SuperKEKB on Belle II Silicon Vertex Detector. master thesis, department of physics, graduate school of science, The university of Tokyo, 2019.

[9] N. Braun et al. Study of the d0 track resolution. BELLE2-NOTE-PL-2018-037. `https://docs.belle2.org/record/1235?ln=en`, Dec 2018.

[10] T. Abe et al. Belle II Technical Design Report, 2010.

[11] L. Jones. *APV25-S1 user guide version 2.2*. Available at `https://cds.cern.ch/record/1069892/files/cer-002725643.pdf`.

[12] R. Turchetta. Spatial resolution of silicon microstrip detectors. *Nuclear Instruments and Methods in Physics Research Section A: Accelerators, Spectrometers, Detectors and Associated Equipment*, 335(1):44 – 58, 1993.

[13] Jaroslaw Wiechczynski.

[14] K. Nakamura. SVD status, including limits of current detectors in terms of background. Belle II VXD Open Workshop, CERN. `https://indico.cern.ch/event/810687/timetable/#27-svd-status-including-limits`, Jul 2019.

[15] H. Tanigawa. Beam background study for the Belle II Silicon Vertex Detector. HSTD12, Hiroshima. `https://indico.cern.ch/event/803258/contributions/3582915/attachments/1962369/3261968/326-Tanigawa-Belle2SVD_BeamBkg.pdf`, Dec 2019.

[16] D. J. Lange. The EvtGen particle decay simulation package. *Nucl. Instrum. Meth.*, A462:152–155, 2001.

[17] SAD. http://acc-physics.kek.jp/SAD/.

[18] Geant4. https://geant4.web.cern.ch/.

[19] Maurice G. Kendall, M.A. *The Advanced Theory of Statistics*. Charles Griffin & Company Limited, 42 Drury Lane, London, 1943.

[20] H. Tanigawa. Performance of the Belle II Silicon Vertex Detector. HSTD12, Hiroshima. https://indico.cern.ch/event/803258/contributions/3582865/attachments/1962373/3261975/283-Tanigawa-Belle2SVD_Performance.pdf, Dec 2019.

A Search for the ideal three-sample selection algorithm

Here we study three algorithms for the 3-sample selection as shown in Fig. 6.1.

1. *Max. sample at the center*
   Find the sample a_i with the largest ADC value, then choose $[a_{i-1}, a_i, a_{i+1}]$

2. *Max. sum at the latter*
   Find the sum $b_i = a_i + a_{i+1}$ with the largest ADC value, then choose $[a_{i-1}, a_i, a_{i+1}]$

3. *Max. sample at the last*
   Find the sample a_i with the largest ADC value, then choose $[a_{i-2}, a_{i-1}, a_i]$

The motivations of these candidates are explained as follows. The first one, max. sample at the center, is the most simple and robust to the jitter. Naively, we may want to use this algorithm. However, if we consider the signal waveform, we want to capture the rising edge rather than falling tail, as it is steeper. Thus, we slightly shift the position of sampling toward the rising edge. This is the max. sum at the latter algorithm. To confirm the validity of this sampling algorithm, we prepare another sampling with larger shift, max.sample at the last.
In principle, such choice of selections could suggest us to take 3 samples which are not included

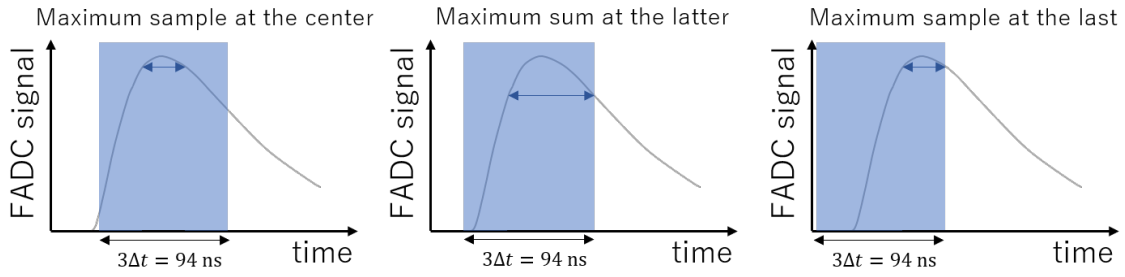

Fig. 6.1: Time-windows to select 3 samples. Each has offset to each other, but they all have the peak and rising edge in the time-window.

in the original 6 samples: e.g. $[a_{-1}, a_0, a_1]$, etc. In such case, we instead take the nearest possible 3 samples not to lose the efficiency by these selections: $[a_0, a_1, a_2]$ for $[a_{-2}, a_{-1}, a_0]$ and $[a_{-1}, a_0, a_1]$; $[a_3, a_4, a_5]$ for $[a_4, a_5, a_6]$.
Naively, the performance should be dependent on these algorithms to select 3 samples, while this dependence should not be changed for the methods (CoG3 or ELS in Section 3.4). This can be checked in the results in Section 3.5.3.
We perform the calibration and estimate the hit-time resolution for those three algorithms to choose three samples.[17] The method is describe in Section 3.5.
First, the pairs of correlation plots in Layer 3 Ladder 1 Sensor 1 Side V are shown in Fig. 6.2 for each algorithm. Here we have a different shape of correlation for *max. sample at the last*, even though they seem to have a smooth connection to the correlation in other windows. In this region, ELS is clearly affected by its negative part of the fit function, and almost lose the correlation. We can expect that this selection has the worst timing resolution.
Then, we perform the fit to get the calibration function. For *max. sample at the last*, the fit

[17] In this section, we set $\tau = 50$ ns in ELS fit function $a(t)$.

quality is not good. As you can see in the lower left plot in Figure 6.2, the polarization of the third-degree polynomial is inverted. For the ELS, the slope of the linear function is inverted in some sensors, as shown. Fit range is very small, [-8, 1] and if we make the upper limit larger to 1.5, fitting fails with "abnormal minimization". Thus, we also lose the stability of the fit in this selection.
After applying the calibration $T_{\mathrm{SVD}} = g(T_{\mathrm{SVD;raw}})$ to the same data sample as we used for the calibration, we can get the calibrated correlations in Fig. 6.3. Here we fit with linear function $a + bx$ to confirm that the calibration works fine. The correlation after calibration is consistent with T_{SVD} = T0 + TB − FF except for *max. sample at the last*.

The determined calibration function g enables us to calculate $T_{\mathrm{SVD}} = g(T_{\mathrm{SVD;raw}})$. Calibration is done on each sensor and side, and here we combine the results of all. Then, we can get the distribution of T_{SVD} − (T0 + TB − FF). The distribution in each method and algorithms are shown in Fig. 6.4. There are some tail components and the distribution is not exactly Gaussian, thus we simply fit to the peak region: [-5, 5]. For *max. sample at the last*, the tail of the distribution is quite larger than other two distributions, and have larger σ of the fitted Gaussian. We summarized the σ of the fitted Gaussian (= σ_{fit}) for each distribution in Table 6. From Eq. (35)[18], σ_{SVD} is also calculated for each σ_{fit} and summarized in Table 6. From these results, we can conclude that *max. sum at the latter* is the best selection to take 3 samples from 6 using the waveform information.

Table 6: σ's of the fitted Gaussian and the SVD hit-time resolutions for the two hit-time estimation methods and the three 3-sample selection algorithms. The difference among the timing calculation methods is small, while the difference among the 3-sample selection algorithms is large.

	σ_{fit} [ns]		σ_{SVD} [ns]	
Method	CoG3	ELS	CoG3	ELS
max. sample at the center	2.69	2.62	2.61	2.54
max. sum at the latter	2.57	2.54	2.49	2.45
max. sample at the last	3.13	4.15	3.06	4.10

[18]Here we read σ_{total} as σ_{fit}.

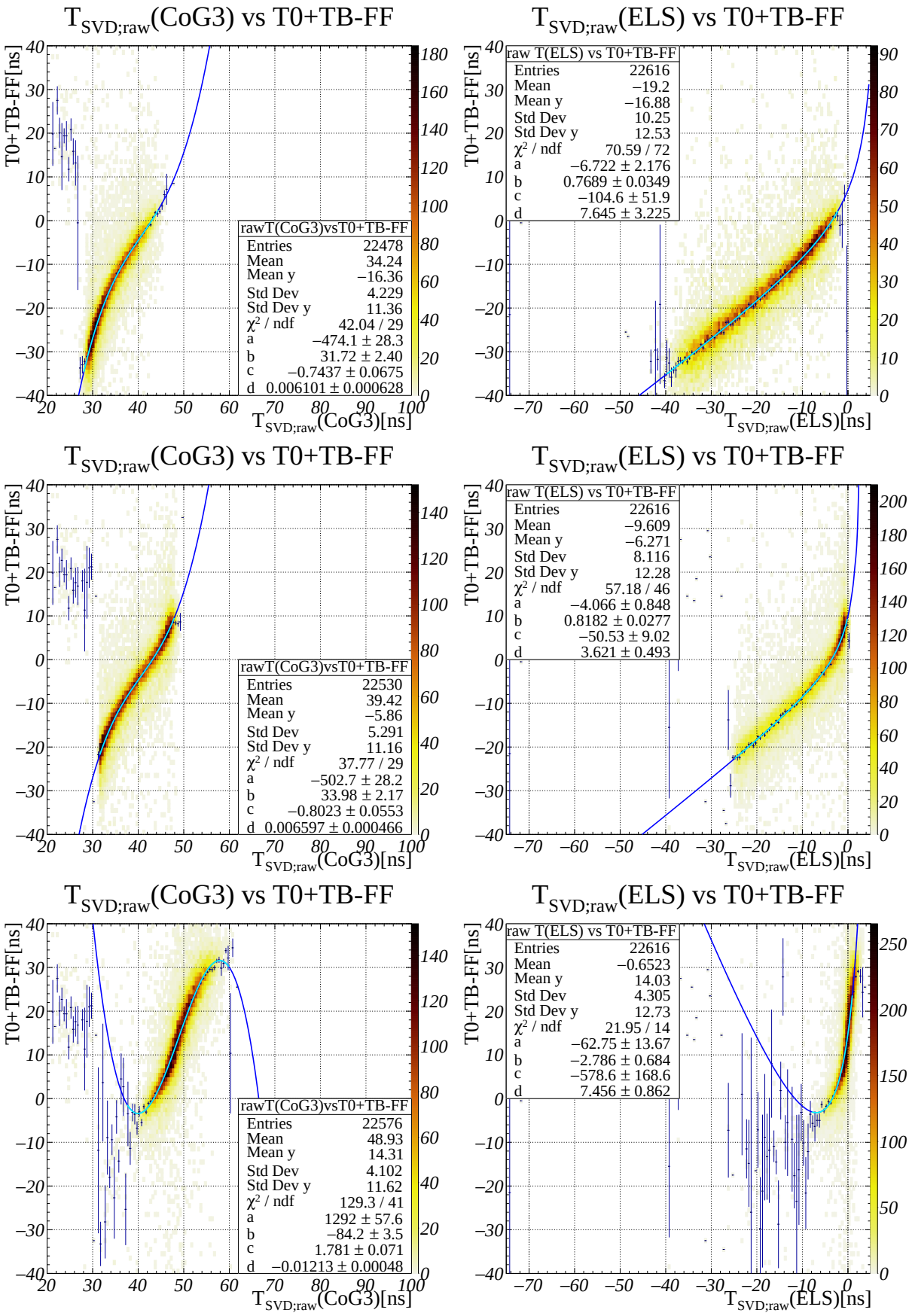

Fig. 6.2: Correlation between $T_{\mathrm{SVD;raw}}$ and T0+TB−FF with CoG3 (left) and ELS (right), for *max. sample at the center* (upper), *max. sum at the latter* (middle), and *max. sample at the last* (lower). The dark-blue point with error bars shows the mean of the T0+TB−FF distributions at each $T_{\mathrm{SVD;raw}}$ bin, with an error calculated by its standard deviation divided by the square root of the total entries. The light-blue line and blue line represent the fit curve in the fit range and outside the fit range, respectively.

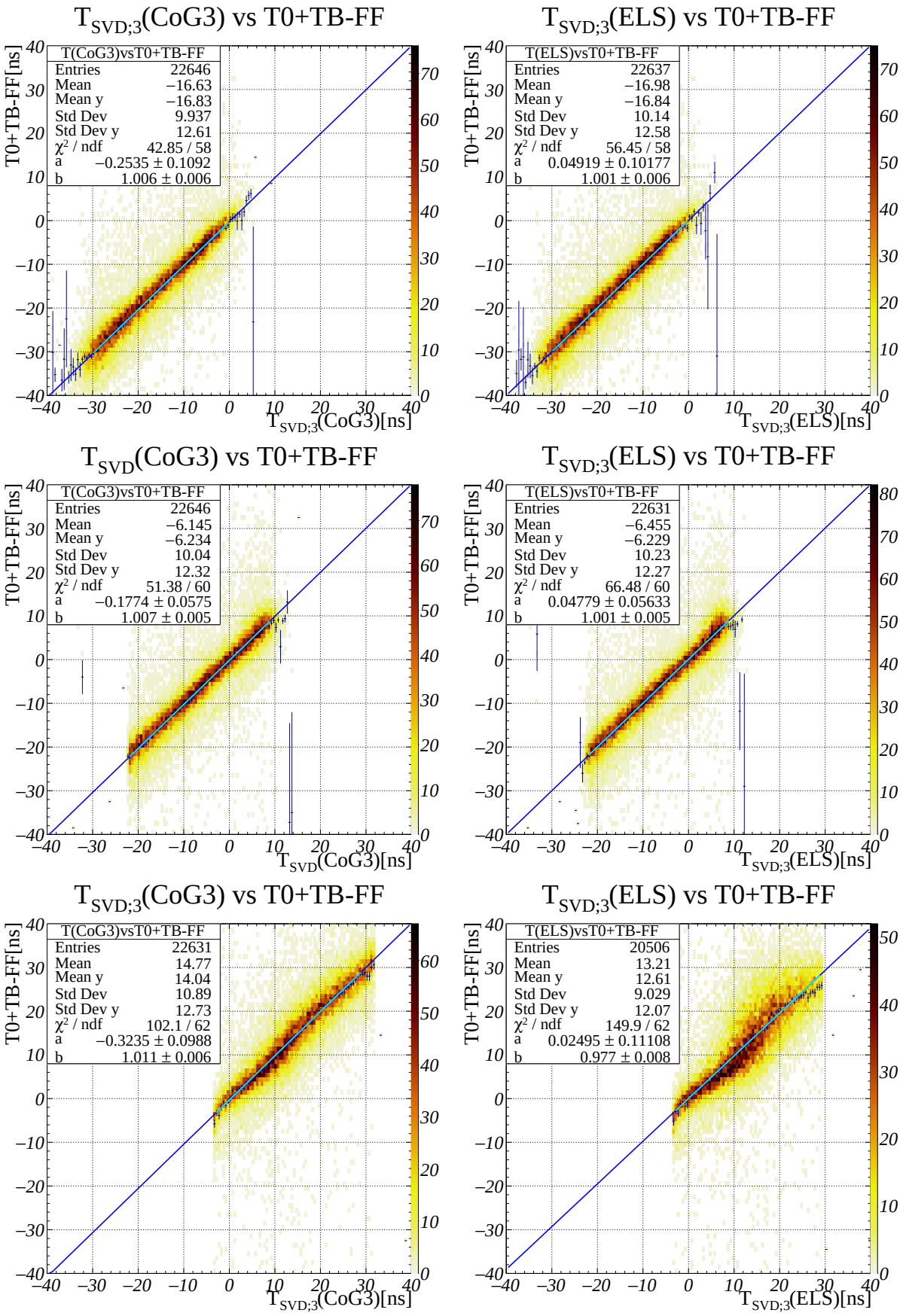

Fig. 6.3: Correlation between T_{SVD} and T0+TB−FF with CoG3 (left) and ELS (right), for *max. sample at the center* (upper), *max. sum at the latter* (middle), and *max. sample at the last* (lower). The dark-blue point with error bars shows the mean of the T0+TB−FF distributions at each $T_{\mathrm{SVD;raw}}$ bin, with an error calculated by its standard deviation divided by the square root of the total entries. The light-blue line and blue line represent the fit curve in the fit range and outside the fit range, respectively.

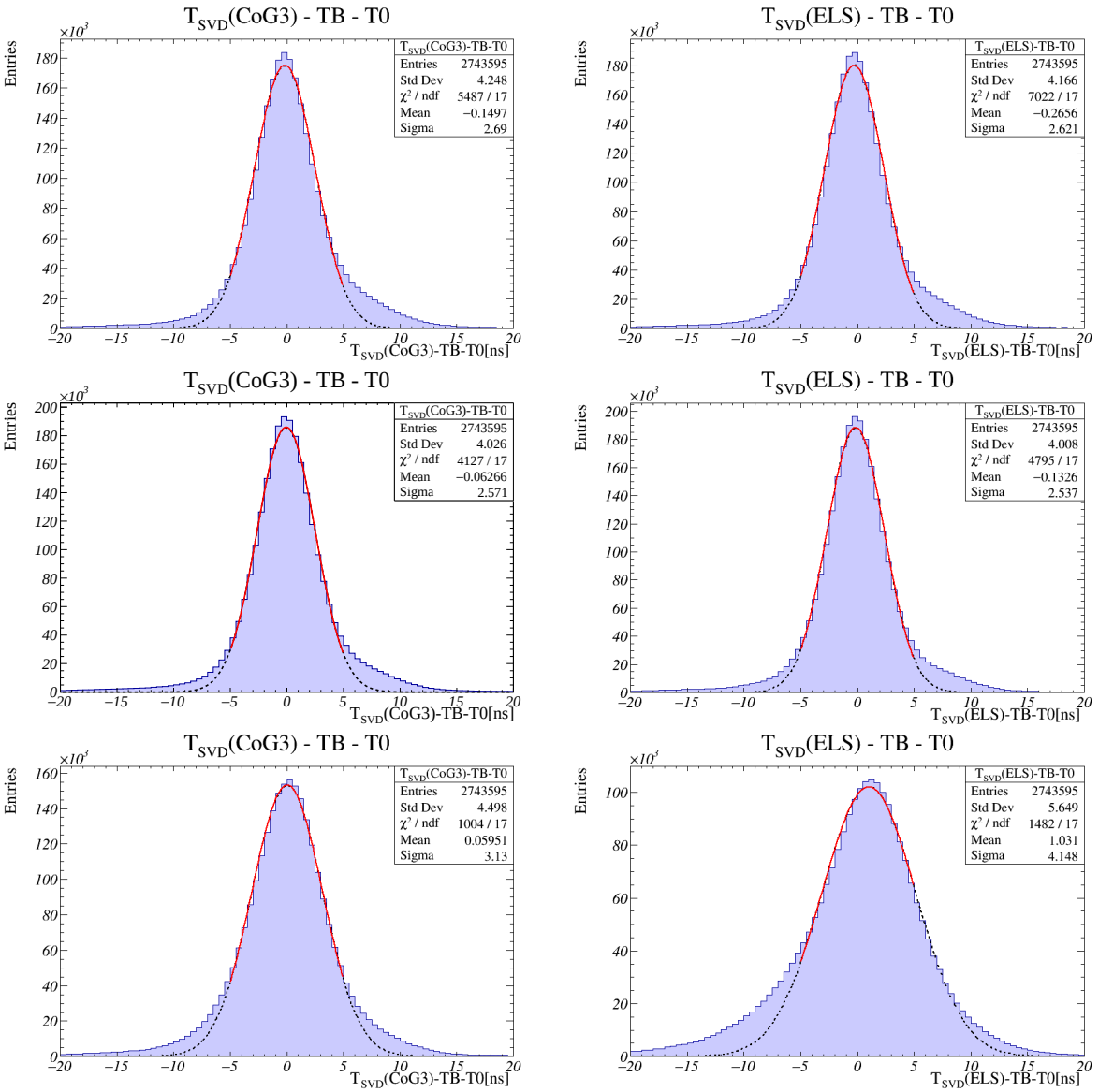

Fig. 6.4: Total distribution of $T_{\mathrm{SVD}} - \mathrm{TB} - \mathrm{T0}$ (top: *max. sample at the center*, middle: *max. sum at the latter*, bottom: *max. sample at the last*). The width of this distribution approximately corresponds to the resolution of SVD hit-time.

B Tuning of the time constant τ in the ELS fit function $a(t)$

Here we tune the time constant to maximize the hit-time performance. The change of this time constant largely affects the raw timing estimation in ELS. We use the same data sample as in the last section (which is common for all τ), and change τ in the ELS fit function $a(t)$ in Eq. (11) to 35, 40, 45, 50, 55, 60, 65 ns. With these various values of τ, we perform the same analysis as in the last section and get correlations and the timing distributions. The calibration functions determined from the correlation between $T_{\mathrm{SVD;raw}}$ and T0+TB−FF for various tau values are plotted in Fig. 6.5 As you see, the slope of the calibration function changes as the time constant

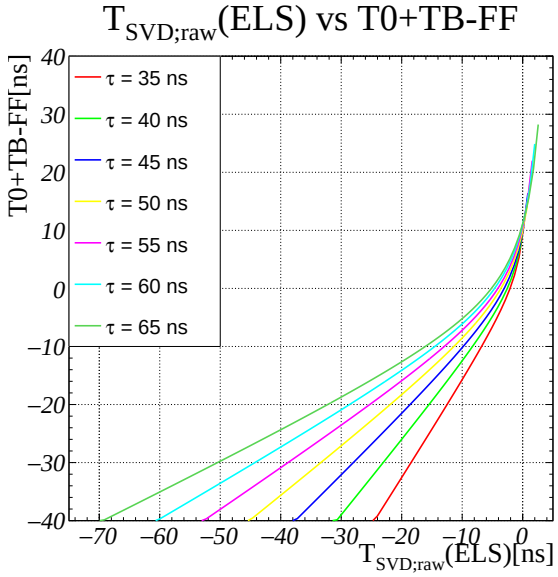

Fig. 6.5: Calibration functions determined from the correlation between $T_{\mathrm{SVD;raw}}$ and T0+TB−FF various time constant τ values from 35 to 65 ns.

changes; larger time constant leads to smaller $T_{\mathrm{SVD;raw}}$. This is consistent with one of the characteristics of the fit function $a(t)$: time constant τ also appears as the peaking time.
The most important indicator for the timing resolution (and further for the background rejection) is the sigma of the fitted Gaussian in $T_{\mathrm{SVD}} - \mathrm{TB} - \mathrm{T0}$ distribution. Thus, we fit the $T_{\mathrm{SVD}} - \mathrm{TB} - \mathrm{T0}$ distribution with the Gaussian as in Section 3.5.3, for range [-5, 5] and for each time constant τ. The resulting Gaussian sigmas are plotted in Fig. 6.6. Though the σ's of the peak Gaussian are within the fit uncertainties in 50–65 ns, we have a local minimum at around τ = 55–60 ns. From this result, we set τ = 55 ns hereafter.

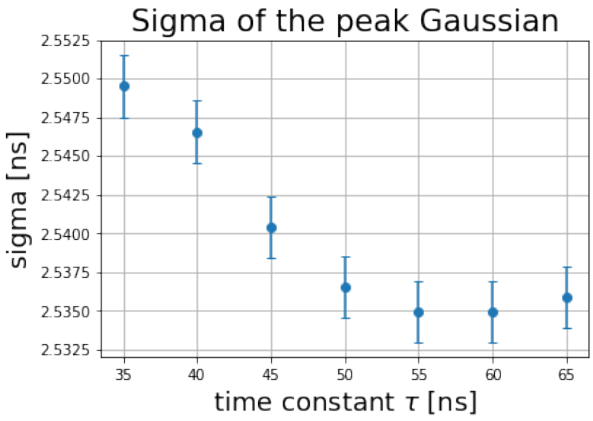

Fig. 6.6: Sigma of the Gaussian fitted to $T_{\mathrm{SVD}} - \mathrm{TB} - \mathrm{T0}$ for each time constant of ELS. The error bars represent the fitting uncertainties on the sigma.

C Derivation of ELS estimators

Here we will describe the derivation of A and $T_{\mathrm{SVD;raw}}$ in detail. Let us start with the expression of sum of squares $S(A, T_{\mathrm{SVD;raw}})$:

$$S(A, T_{\mathrm{SVD;raw}}) = \sum_{i=0}^{2} (a(i\Delta t) - a_i)^2 \tag{59}$$

and the constants: shaping (and decaying) time constant $\tau = 55$ ns and sampling period $\Delta t = 31$ ns.

We assume that A and $T_{\mathrm{SVD;raw}}$ are independent and write down the stationary conditions at the fit result:

$$\frac{\partial S}{\partial A} = \frac{\partial S}{\partial T_{\mathrm{SVD;raw}}} = 0 \tag{60}$$

By substituting the expression of S, we can write as

$$\frac{\partial}{\partial A} \sum_{i=0}^{2} (a(i\Delta t) - a_i)^2 = \frac{\partial}{\partial T_{\mathrm{SVD;raw}}} \sum_{i=0}^{2} (a(i\Delta t) - a_i)^2 = 0 \tag{61}$$

$$\begin{cases} \displaystyle\sum_{i=0}^{2} 2\,(a(i\Delta t) - a_i)\,\frac{\partial}{\partial A} a(i\Delta t) = 0 & (62) \\ \displaystyle\sum_{i=0}^{2} 2\,(a(i\Delta t) - a_i)\,\frac{\partial}{\partial T_{\mathrm{SVD;raw}}} a(i\Delta t) = 0 & (63) \end{cases}$$

Here

$$\frac{\partial}{\partial A} a(i\Delta t) = \frac{1}{A} a(i\Delta t) \tag{64}$$

$$\frac{\partial}{\partial T_{\mathrm{SVD;raw}}} a(i\Delta t) = -\frac{1}{i\Delta t - T_{\mathrm{SVD;raw}}} a(i\Delta t) + \frac{1}{\tau} a(i\Delta t) \tag{65}$$

$$= \left(\frac{1}{\tau} - \frac{1}{i\Delta t - T_{\mathrm{SVD;raw}}} \right) a(i\Delta t) \tag{66}$$

Thus,

$$\begin{cases} \displaystyle\sum_{i=0}^{2} 2\,(a(i\Delta t) - a_i)\,\frac{1}{A} a(i\Delta t) = 0 & (67) \\ \displaystyle\sum_{i=0}^{2} 2\,(a(i\Delta t) - a_i) \left(\frac{1}{\tau} - \frac{1}{i\Delta t - T_{\mathrm{SVD;raw}}} \right) a(i\Delta t) = 0 & (68) \end{cases}$$

$$\begin{cases} \displaystyle\sum_{i=0}^{2} (a(i\Delta t) - a_i)\, a(i\Delta t) = 0 & (69) \\ \displaystyle\sum_{i=0}^{2} (a(i\Delta t) - a_i) \left(\frac{1}{\tau} - \frac{1}{i\Delta t - T_{\mathrm{SVD;raw}}} \right) a(i\Delta t) = 0 & (70) \end{cases}$$

$$\begin{cases} \displaystyle\sum_{i=0}^{2} \left(a(i\Delta t) - a_i\right) a(i\Delta t) = 0 & (71) \\ \displaystyle\sum_{i=0}^{2} \frac{1}{i\Delta t - T_{\mathrm{SVD;raw}}} \left(a(i\Delta t) - a_i\right) a(i\Delta t) = 0 & (72) \end{cases}$$

$$\begin{cases} \displaystyle\sum_{i=0}^{2} \left(a(i\Delta t) - a_i\right) (i\Delta t - T_{\mathrm{SVD;raw}}) e^{-i\Delta t/\tau} = 0 & (73) \\ \displaystyle\sum_{i=0}^{2} \left(a(i\Delta t) - a_i\right) e^{-i\Delta t/\tau} = 0 & (74) \end{cases}$$

$$\begin{cases} \displaystyle\sum_{i=0}^{2} i \left(a(i\Delta t) - a_i\right) e^{-i\Delta t/\tau} = 0 & (75) \\ \displaystyle\sum_{i=0}^{2} \left(a(i\Delta t) - a_i\right) e^{-i\Delta t/\tau} = 0 & (76) \end{cases}$$

$$\begin{cases} \left(a(\Delta t) - a_1\right) e^{-\Delta t/\tau} = -2 \left(a(2\Delta t) - a_2\right) e^{-2\Delta t/\tau} & (77) \\ a(0) - a_0 = \left(a(2\Delta t) - a_2\right) e^{-2\Delta t/\tau} & (78) \end{cases}$$

$$\begin{cases} \left(a(\Delta t) - a_1\right) e^{-\Delta t/\tau} = -2 \left(a(0) - a_0\right) & (79) \\ a(0) - a_0 = \left(a(2\Delta t) - a_2\right) e^{-2\Delta t/\tau} & (80) \end{cases}$$

$$\begin{cases} \dfrac{A\left(\Delta t - T_{\mathrm{SVD;raw}}\right)}{\tau} \exp\left(1 - \dfrac{2\Delta t - T_{\mathrm{SVD;raw}}}{\tau}\right) + \dfrac{2A\left(-T_{\mathrm{SVD;raw}}\right)}{\tau} \exp\left(1 - \dfrac{-T_{\mathrm{SVD;raw}}}{\tau}\right) = a_1 e^{-\Delta t/\tau} + 2a_0 \\ \dfrac{A\left(-T_{\mathrm{SVD;raw}}\right)}{\tau} \exp\left(1 - \dfrac{-T_{\mathrm{SVD;raw}}}{\tau}\right) - \dfrac{A\left(2\Delta t - T_{\mathrm{SVD;raw}}\right)}{\tau} \exp\left(1 - \dfrac{4\Delta t - T_{\mathrm{SVD;raw}}}{\tau}\right) = a_0 - a_2 e^{-2\Delta t/\tau} \end{cases}$$

(81)

(82)

To solve for hit-time $T_{\mathrm{SVD;raw}}$, remove amplitude A:

$$\begin{aligned} &\frac{a_1 e^{-\Delta t/\tau} + 2a_0}{\frac{\left(\Delta t - T_{\mathrm{SVD;raw}}\right)}{\tau} \exp\left(1 - \frac{2\Delta t - T_{\mathrm{SVD;raw}}}{\tau}\right) + \frac{2\left(-T_{\mathrm{SVD;raw}}\right)}{\tau} \exp\left(1 - \frac{-T_{\mathrm{SVD;raw}}}{\tau}\right)} \\ &= \frac{a_0 - a_2 e^{-2\Delta t/\tau}}{\frac{\left(-T_{\mathrm{SVD;raw}}\right)}{\tau} \exp\left(1 - \frac{-T_{\mathrm{SVD;raw}}}{\tau}\right) - \frac{\left(2\Delta t - T_{\mathrm{SVD;raw}}\right)}{\tau} \exp\left(1 - \frac{4\Delta t - T_{\mathrm{SVD;raw}}}{\tau}\right)} \end{aligned} \tag{83}$$

Here we will define waveform dependence $w\left(a_0, a_1, a_2; \tau\right)$ as:

$$w\left(a_0, a_1, a_2; \tau\right) = \frac{a_0 - e^{-2\Delta t/\tau} a_2}{2a_0 + e^{-\Delta t/\tau} a_1} \tag{84}$$

With this,

$$w\left(a_0, a_1, a_2; \tau\right) = \frac{\frac{\left(-T_{\mathrm{SVD;raw}}\right)}{\tau} \exp\left(1 - \frac{-T_{\mathrm{SVD;raw}}}{\tau}\right) - \frac{\left(2\Delta t - T_{\mathrm{SVD;raw}}\right)}{\tau} \exp\left(1 - \frac{4\Delta t - T_{\mathrm{SVD;raw}}}{\tau}\right)}{\frac{\left(\Delta t - T_{\mathrm{SVD;raw}}\right)}{\tau} \exp\left(1 - \frac{2\Delta t - T_{\mathrm{SVD;raw}}}{\tau}\right) + \frac{2\left(-T_{\mathrm{SVD;raw}}\right)}{\tau} \exp\left(1 - \frac{-T_{\mathrm{SVD;raw}}}{\tau}\right)} \tag{85}$$

$$= \frac{\left(-T_{\mathrm{SVD;raw}}\right) - \left(2\Delta t - T_{\mathrm{SVD;raw}}\right) e^{-4\Delta t/\tau}}{\left(\Delta t - T_{\mathrm{SVD;raw}}\right) e^{-2\Delta t/\tau} + 2\left(-T_{\mathrm{SVD;raw}}\right)} \tag{86}$$

$$w\left(a_0, a_1, a_2; \tau\right)\left(e^{-2\Delta t/\tau}\Delta t - \left(2 + e^{-2\Delta t/\tau}\right) T_{\mathrm{SVD;raw}}\right) = -2e^{-4\Delta t/\tau}\Delta t - \left(1 - e^{-4\Delta t/\tau}\right) T_{\mathrm{SVD;raw}} \tag{87}$$

$$\left(1 - e^{-4\Delta t/\tau} - w\left(a_0, a_1, a_2; \tau\right)\left(2 + e^{-2\Delta t/\tau}\right)\right) T_{\mathrm{SVD;raw}} = -w\left(a_0, a_1, a_2; \tau\right) e^{-2\Delta t/\tau}\Delta t - 2e^{-4\Delta t/\tau}\Delta t \tag{88}$$

Thus we can get the result

$$T_{\mathrm{SVD;raw}} = -\frac{2e^{-4\Delta t/\tau} + w\left(a_0, a_1, a_2; \tau\right) e^{-2\Delta t/\tau}}{1 - e^{-4\Delta t/\tau} - w\left(a_0, a_1, a_2; \tau\right)\left(2 + e^{-2\Delta t/\tau}\right)} \cdot \Delta t \tag{89}$$

We can also solve for A.

$$\begin{aligned}
A &= \frac{a_1 e^{-\Delta t/\tau} + 2a_0}{\frac{\left(\Delta t - T_{\mathrm{SVD;raw}}\right)}{\tau} \exp\left(1 - \frac{2\Delta t - T_{\mathrm{SVD;raw}}}{\tau}\right) + \frac{2\left(-T_{\mathrm{SVD;raw}}\right)}{\tau} \exp\left(1 - \frac{-T_{\mathrm{SVD;raw}}}{\tau}\right)} \\
&= \tau \exp\left(-1 - T_{\mathrm{SVD;raw}}/\tau\right) \frac{a_1 e^{-\Delta t/\tau} + 2a_0}{\left(\Delta t - T_{\mathrm{SVD;raw}}\right) e^{-2\Delta t/\tau} + 2\left(-T_{\mathrm{SVD;raw}}\right)} \\
&= \frac{\tau/\Delta t \cdot \exp\left(-1 - T_{\mathrm{SVD;raw}}/\tau\right)\left(a_1 e^{-\Delta t/\tau} + 2a_0\right)}{\frac{1+e^{-4\Delta t/\tau}-2w}{1-e^{-4\Delta t/\tau}-w\left(2+e^{-2\Delta t/\tau}\right)} \cdot e^{-2\Delta t/\tau} + 2\frac{2e^{-4\Delta t/\tau}+we^{-2\Delta t/\tau}}{1-e^{-4\Delta t/\tau}-w\left(2+e^{-2\Delta t/\tau}\right)}} \\
&= \frac{\left(1 - e^{-4\Delta t/\tau} - w\left(2 + e^{-2\Delta t/\tau}\right)\right)\left(a_1 e^{-\Delta t/\tau} + 2a_0\right)}{\Delta t/\tau \cdot \exp\left(1 + T_{\mathrm{SVD;raw}}/\tau\right)\left(e^{-2\Delta t/\tau} + 4e^{-4\Delta t/\tau} + e^{-6\Delta t/\tau}\right)} \\
&= \frac{\left(1 - e^{-4\Delta t/\tau}\right)\left(a_1 e^{-\Delta t/\tau} + 2a_0\right) - \left(2 + e^{-2\Delta t/\tau}\right)\left(a_0 - e^{-2\Delta t/\tau} a_2\right)}{\Delta t/\tau \cdot \exp\left(1 + T_{\mathrm{SVD;raw}}/\tau\right)\left(e^{-2\Delta t/\tau} + 4e^{-4\Delta t/\tau} + e^{-6\Delta t/\tau}\right)} \\
&= \frac{\left(1 - e^{-4\Delta t/\tau}\right) e^{-\Delta t/\tau} a_1 + \left(2 + e^{-2\Delta t/\tau}\right) e^{-2\Delta t/\tau} a_2 - \left(e^{-2\Delta t/\tau} + 2e^{-4\Delta t/\tau}\right) a_0}{\Delta t/\tau \cdot \exp\left(1 + T_{\mathrm{SVD;raw}}/\tau\right)\left(e^{-2\Delta t/\tau} + 4e^{-4\Delta t/\tau} + e^{-6\Delta t/\tau}\right)} \\
&= \frac{\left(e^{\Delta t/\tau} - e^{-3\Delta t/\tau}\right) a_1 + \left(2 + e^{-2\Delta t/\tau}\right) a_2 - \left(1 + 2e^{-2\Delta t/\tau}\right) a_0}{\Delta t/\tau \cdot \exp\left(1 + T_{\mathrm{SVD;raw}}/\tau\right)\left(1 + 4e^{-2\Delta t/\tau} + e^{-4\Delta t/\tau}\right)}
\end{aligned} \tag{90}$$

For simplicity, we use $T_{\mathrm{SVD;raw}}$ in the expression of A. This results can be used for the future update of the amplitude calculation.

D Validation of the calibration parameters

As discussed in Section 3.5.2, we check the validity of the calibration by checking all the four calibration parameters a, b, c, d for CoG3 and ELS. The resulting distributions are shown in Fig. 6.7.
Though there are some values in ELS that are far away from the others, those are confirmed to be well-fitted, by the eye. The variation can arise from both the low statistics and the actual difference in correlation.

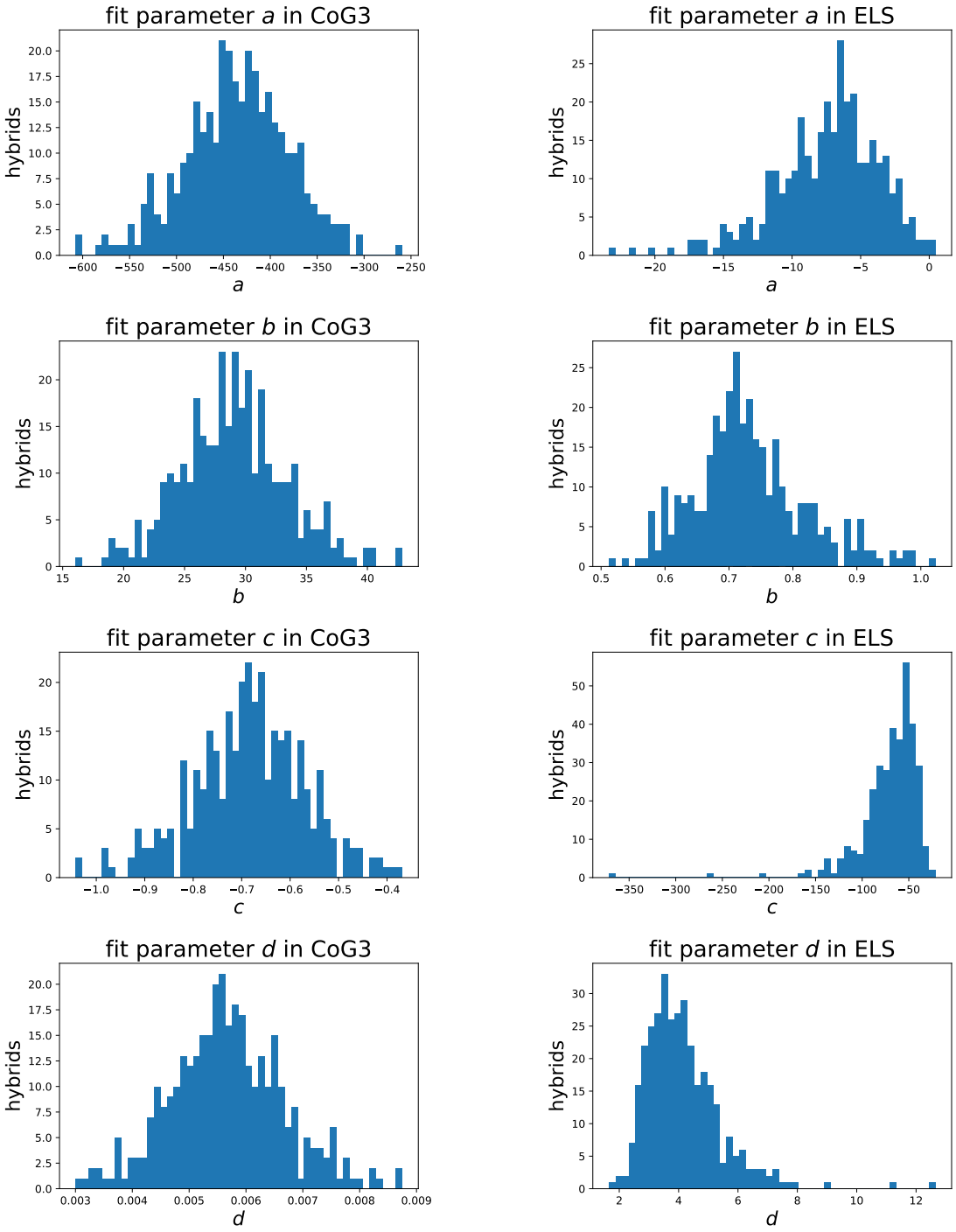

Fig. 6.7: The distribution of all the calibration parameters for all the sensors/hybrids.

E Determination of the time-window position t_0 with the Max-Sum algorithm

When we take three samples at APV25, in practice, we determine which samples to take by a fine-timing (or TOP timing) level-1 trigger, which is currently under development. The start timing of these three samples can be different from that of the waveform-selected three samples in Section 3.5, because of the electrical noise, trigger jitter and other timing jitters. Triggers with sufficient timing resolution are not available for the SVD data taking so far, thus we use EventT0 information to emulate the ideal trigger timing which determines a three-sample time-window for each event, then we apply this time-window on the six samples offline.

Next we adjust the latency for the best time-window. If the EventT0 ($= t_{\mathrm{col}} - t_{\mathrm{TRG}}$) gets larger, i.e., the collision timing compared to the trigger timing gets later, SVD signal also gets later in six-sample time-window. In other words, there must be a correlation between the EventT0 and the best position of three samples in the 6 samples. Such a position of three samples is given by the MaxSum algorithm, as described in Section 3.3. To see the correlation, we classified the data into five groups: i of max. sum $a_i + a_{i+1}$ equals to 0, 1, 2, 3, 4. Then, we get the EventT0 (with trigger bin correction, denoted as T0+TB) distributions for each i of max. sum. These five distributions and the sum of five distributions (total) are shown in Fig. 6.8.

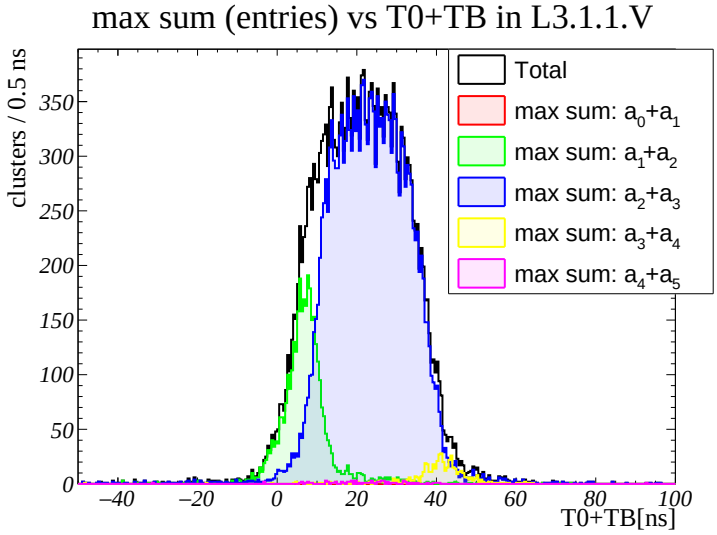

Fig. 6.8: T0+TB distributions for each i of max. sum. Black line shows the total entries at each T0+TB bins.

The total distribution is localized from T0+TB = 0 ns to 40 ns, which makes it difficult to extract the correlation information. Therefore, instead of these distribution (entry N_i), we extract the information of probability to take i of max. sum at a certain value for each T0+TB bin:

$$P_i(\mathrm{T0+TB}) = \frac{N_i(\mathrm{T0+TB})}{N_{\mathrm{total}}(\mathrm{T0+TB})}. \tag{91}$$

We calculate this for $i = 0,\ 1,\ 2,\ 3,\ 4$. The results of these divisions are shown in Fig. 6.9. Here three samples $a_{i-1},\ a_i,\ a_{i+1}$ with i of the highest possibility at each T0+TB bin are regarded as the best three samples. This enables us to define the T0+TB region for each i. The one

clock-cycle (Δt = 31.4 ns) shift in T0+TB corresponds to the one sample shift in ADC sampling window i.e. one shift of i. This periodic structure by Δt = 31.4 ns can be observed in the plot. Now we can see the threshold to move from i to $i+1$ which we cannot clearly see in Fig. 6.8. We can write the four boarders of the region corresponds to i = 0, 1, 2, 3, 4 as t_0, $t_0 + \Delta t$, $t_0 + 2\Delta t$, $t0 + 3\Delta t$, where t_0 is the same as that appears in Eq. 47.

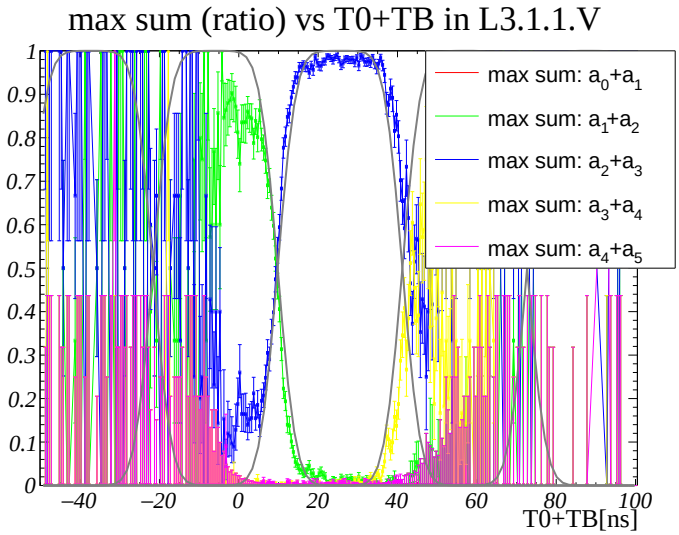

Fig. 6.9: Probability of each max. sum at T0+TB. In the region with less statistics, we cannot get much information.

The shape of this graph can be explained as follows. If there is no timing jitter nor noise, the time-window using the waveform information perfectly corresponds to the time-window in real time. In such case, we can express the probability of each i of max. sum by step function as shown in Fig. 6.10.

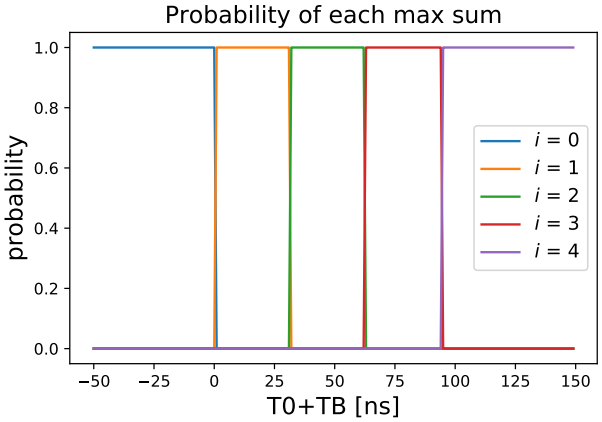

Fig. 6.10: An example of step function probability of each max. sum at T0+TB (t_0 = 0 ns). We have a definite max. sum at each time bin.

If we assume that the effect of electrical noise is also expressed as timing jitter, and that the timing jitter obeys Gaussian distribution, we can get the estimation for the probability $P_i(t)$ by

convolving the step function $H(x)$ and the Gaussian $G(x;\mu,\sigma)$. For $i = 1$, this function can be written as

$$P_1(t) = \frac{1}{2}\left[\mathrm{erf}\left(\frac{t-t_0}{\sqrt{2}\sigma}\right) - \mathrm{erf}\left(\frac{t-(t_0+\Delta t)}{\sqrt{2}\sigma}\right)\right], \tag{92}$$

where the error function $\mathrm{erf}(x)$ is defined as

$$\mathrm{erf}(x) = \frac{2}{\sqrt{\pi}}\int_0^x \exp\left(-t^2\right)\mathrm{d}t. \tag{93}$$

For the detailed derivation, see also Appendix F. For $i = 2$ and 3, we can get the result by just changing $t_0 \leftrightarrow t_0 + \Delta t$ and $t_0 + 2\Delta t$. For the $i = 0$ and 4, the shape is not the same: only the one step function contributes. From this formula, we can tell that the timing jitter effect appears as replacing the step function with error function. We can calculate probability by this formula and get the plot as shown in Fig. 6.11. Fitting this function to data in each 5 max sums with same

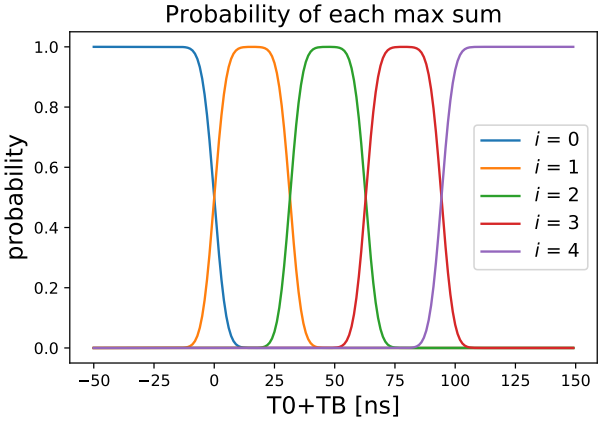

Fig. 6.11: An example of error function probability of each max. sum at T0+TB. Comapred to Fig. 6.10, we have a blunted distribution by the error function.

parameter, we can get the position of the time-window t_0. By this way, we can decide the time window.

In practice, we do not have enough statistics beyond $i = 0$ and 4. Thus, we approximate their functions to the same form as the other i. Then, we can write the probability for all i as

$$P_i(t) = \frac{1}{2}\left[\mathrm{erf}\left(\frac{t-t_0-(i-1)\Delta t}{\sqrt{2}\sigma}\right) - \mathrm{erf}\left(\frac{t-t_0-i\Delta t)}{\sqrt{2}\sigma}\right)\right]. \tag{94}$$

This function is perfectly periodic, as plotted in Fig. 6.12. Note that this $(i-1)\Delta t$ term is the same as the 1st frame correction.

Then we can completely overlap these five functions as shown in Fig. 6.13 by shifting the time corresponding to each i of max. sum. Thus we can easily perform the fit. We fitted sensor-wise and side-wise, and one of the fit results is also shown in Fig. 6.9 with dark gray line, shifted for each i. Gathering the results in all the sensors, the distribution of the timing threshold t_0 is plotted in Fig. 6.14. In the real implementation of this time-window, it is difficult to use different trigger-latency values among the sensors and the sensor-sides. Thus, we average all the result and get one time-window threshold (dotted line in Fig. 6.14):

$$t_0 = -22.40\ \mathrm{ns}. \tag{95}$$

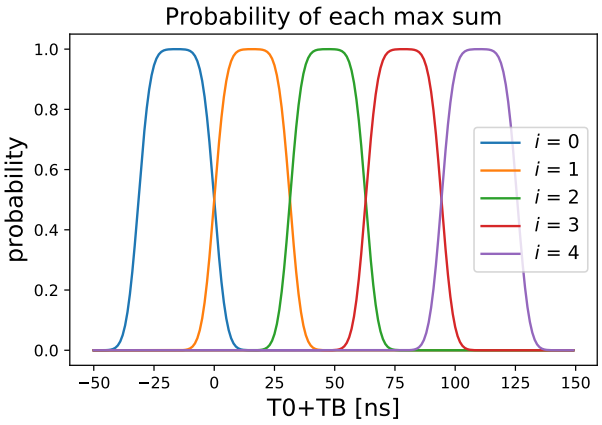

Fig. 6.12: Approximated error function probability of each max. sum at T0+TB. The edges are approximated and we get the same function (except for the shift) for all max. sum.

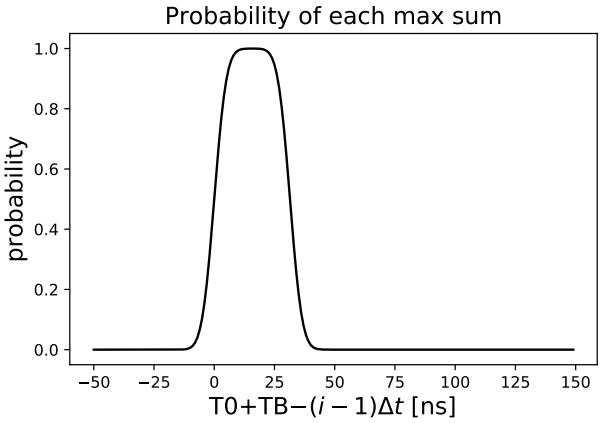

Fig. 6.13: Overlapped error function probability vs T0+TB$-(i-1)\Delta t$ (or T0+TB−FF). By applying the first frame correction, we can shift the functions of each max. sum and get the overlapped distribution.

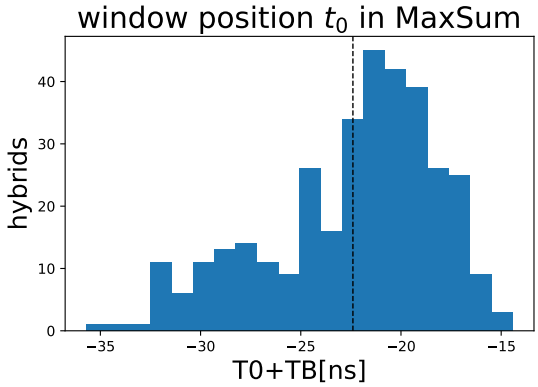

Fig. 6.14: The distribution of timing thresholds of max. sum probability. Dotted line stands for the mean of −22.40 ns.

With this value, we can apply time-window and emulate three-sample-mode data from the existing six-sample-mode data.

F Derivation of probability function $P_i(t)$ for i of max. sum with jitters

Here we perform the convolution of the step function $H(x)$ and the Gaussian $G(x;\mu,\sigma)$ to calculate the probability $P_i(t)$ for $i = 1$.

$$
\begin{aligned}
P_1(t) &= \int_{-\infty}^{\infty} G(t;\mu,\sigma)(H(\mu - t_0) - H(\mu - (t_0 + \Delta t)))\mathrm{d}\mu && (96)\\
&= \int_{t_0}^{t_0+\Delta t} G(t;\mu,\sigma)\mathrm{d}\mu && (97)\\
&= \int_{t_0}^{t_0+\Delta t} \frac{1}{\sigma\sqrt{2\pi}} \exp\left(-\frac{(t-\mu)^2}{2\sigma^2}\right)\mathrm{d}\mu && (98)\\
&= \int_{t-(t_0+\Delta t)}^{t-t_0} \frac{1}{\sigma\sqrt{2\pi}} \exp\left(-\frac{\mu'^2}{2\sigma^2}\right)\mathrm{d}\mu' \quad (\mu' = t - \mu) && (99)\\
&= \int_{\frac{t-(t_0+\Delta t)}{\sigma}}^{\frac{t-t_0}{\sigma}} \frac{1}{\sqrt{2\pi}} \exp\left(-\frac{\mu''^2}{2}\right)\mathrm{d}\mu'' \quad (\mu'' = \mu'/\sigma) && (100)\\
&= \Phi\left(\frac{t-t_0}{\sigma}\right) - \Phi\left(\frac{t-(t_0+\Delta t)}{\sigma}\right) && (101)\\
&= \frac{1}{2}\left[1 + \mathrm{erf}\left(\frac{t-t_0}{\sqrt{2}\sigma}\right)\right] - \frac{1}{2}\left[1 + \mathrm{erf}\left(\frac{t-(t_0+\Delta t)}{\sqrt{2}\sigma}\right)\right] && (102)\\
&= \frac{1}{2}\left[\mathrm{erf}\left(\frac{t-t_0}{\sqrt{2}\sigma}\right) - \mathrm{erf}\left(\frac{t-(t_0+\Delta t)}{\sqrt{2}\sigma}\right)\right]. && (103)
\end{aligned}
$$

Here, cumulative distribution function of Gaussian $\Phi(x)$ is given as:

$$\Phi(x) = \frac{1}{\sqrt{2\pi}} \int_{-\infty}^{x} \exp\left(-\frac{t^2}{2}\right)\mathrm{d}t, \tag{104}$$

which are easily related to the error function $\mathrm{erf}(x)$

$$\mathrm{erf}(x) = \frac{2}{\sqrt{\pi}} \int_{0}^{x} \exp\left(-t^2\right)\mathrm{d}t \tag{105}$$

as:

$$
\begin{aligned}
\Phi(x) &= \frac{1}{\sqrt{2\pi}} \int_{-\infty}^{x} \exp\left(-\frac{t^2}{2}\right)\mathrm{d}t && (106)\\
&= \frac{1}{2} + \frac{1}{\sqrt{2\pi}} \int_{0}^{x} \exp\left(-\frac{t^2}{2}\right)\mathrm{d}t && (107)\\
&= \frac{1}{2} + \frac{1}{\sqrt{\pi}} \int_{0}^{x/\sqrt{2}} \exp\left(-t'^2\right)\mathrm{d}t' \ (t' = t/\sqrt{2}) && (108)\\
&= \frac{1}{2}\left[1 + \mathrm{erf}\left(\frac{x}{\sqrt{2}}\right)\right]. && (109)
\end{aligned}
$$